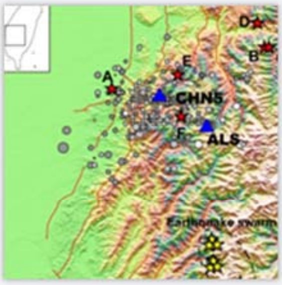

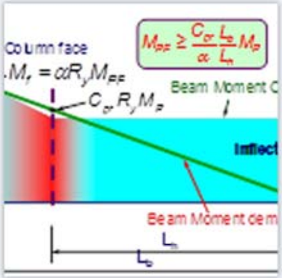

2014

NCREE
Research Programs and Accomplishments

National Center for Research on Earthquake Engineering,
National Applied Research Laboratories

www.ncree.org.tw

Contents

Shaking Table Testing of a Shallow Foundation Model

Jiunn-Shyang Chiou[1], Chia-Han Chen[2], and Yu-Wei Huang[3]

邱俊翔 [1]、陳家漢 [2]、黃郁惟 [3]

Abstract

In recent years, the foundation rocking mechanism was adopted in seismic design to isolate seismic waves for reducing the seismic demand. In this study, shaking table testing of a rocking-dominated column-footing model was performed to investigate the rocking effect on the dynamic behavior of the structure of this type under seismic loading. The model was a column of height of 80cm with a square footing of size 40cm×40cm. Vietnam sand was adopted for the soil specimen. Specific sinusoidal waves were adopted for input motions. From the preliminary results of the testing, the rocking response of the footing could help reduce the dynamic amplification effect of the model. For the model under a small excitation, its acceleration response could be amplified, while upon the application of a larger excitation, its acceleration response was limited by the rotational capacity of the footing. However, too large seismic loading would trigger foundation failure, such as foundation twisting.

Keywords: Footings, shallow foundations, shaking table testing.

Introduction

In Taiwan, spread footings are commonly used bridge foundations founded on a stiff stratum, such as gravel or rock. They are normally subjected to vertical loading, but when their superstructure is subjected to horizontal loading, such as seismic loading, they will have rotational displacements due to the induced moments at the column base. In recent years, seismic design has moved toward performance based design, in which a structure is designed to meet different performance requirements corresponding to different levels of design earthquakes from low seismic intensity to high seismic intensity. For the higher level of design earthquake, the footing may significantly rock to make the column base become quite flexible. The above foundation rocking effect in recent years was used in seismic design to isolate seismic waves for reducing the seismic demand (Gajan et al., 2005; Megro and Kawashima, 2005). However, foundation rocking may cause the soil around the edges of the footing to yield and settle and also result in adverse influence on the stability of structures. For instance, Shirato et al. (2008) had conducted large scale of shaking table testing for a structure model under different seismic and foundation embedment cases: in some cases the structure model was intact; in some cases the model had significant settlement and even in a case the model toppled. Therefore, it is necessary to conduct more studies to investigate the applicability of foundation rocking for the use in seismic isolation. To this end, this study designed a rocking-governed column-footing model and conducted shaking table testing on it to investigate the seismic performance of this type of structure.

Model Design and Test Program

A prototype condition that an 8m-high single column with a 4m×4m footing is situated on a 12m-thick sandy stratum was assumed. The length scaling factor of 10 was adopted and the model was designed as displayed in Fig. 1, in which the height of the column was 80 cm, the size of the footing was 40cm×40cm and the weight of the model was 0.165 kN. Mass blocks of weight 0.905 kN were placed on the top of the column to simulate the weight of the structure. The weight of the whole model was 1.07 kN. Vietnam sand was used for the soil specimen. The

[1] Research Fellow, National Center for Research on Earthquake Engineering, jschiou@ncree.org.tw
[2] Assistant Researcher, National Center for Research on Earthquake Engineering
[3] Graduate Student, Dept. of Civil Engineering, National Taiwan University

sand was compacted to have the relative density of about 75% to model a stiff stratum.

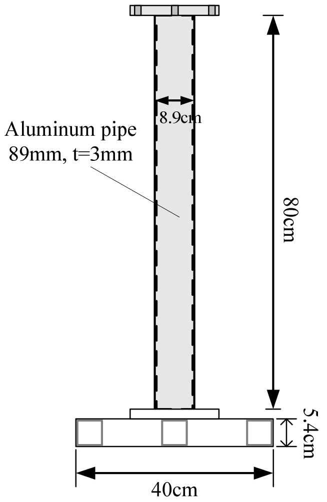

Fig. 1 The column-footing model

Fig. 2 Shaking table testing

The arrangement of the shaking table testing is shown in Fig. 2. The same column-footing was put on a laminar box developed at NCREE. The laminar shear box is composed of 15 layers of sliding frames (Ueng et al., 2006). In the box, the soil specimen size is 1880 mm × 1880 mm × 1520 mm. These 15 layers of frames are separately supported on surrounding rigid steel walls, one above the other, with a vertical gap of 20 mm between adjacent layers, which can simulate the soil movement of a level ground subjected to horizontal seismic waves. On the top of the column attached the mass blocks. The setup of instrument sensors is displayed in Fig. 3, including accelerometers, LDTs, and strain gauges. The accelerometers were used to measure the vertical and horizontal accelerations of the structure model and soil. The LDTs were used to measure the horizontal displacement of the frames of the shear box, representing the lateral movements of the soil. The strain gauges were attached on the column sides near the column base to measure the bending strains. The input motions were applied at the bottom of the shear box via the shaking table to simulate seismic loading. Three types of input motions were adopted, including white noise sweeping and sinusoid signals. The amplitude and bandwidth of white noise waves adopted were 0.03g and 60Hz, respectively. The use of white noise sweeping is to identify the dynamic properties of the structure-foundation system and the soil layers. The frequencies of the input sinusoid waves were 1, 2, 4 and 6 Hz.

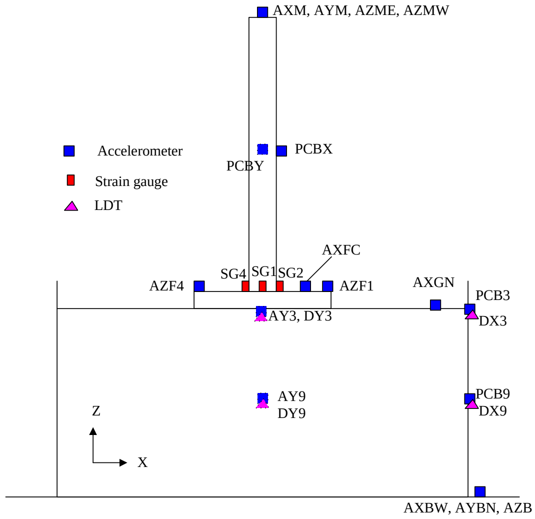

(a) side view

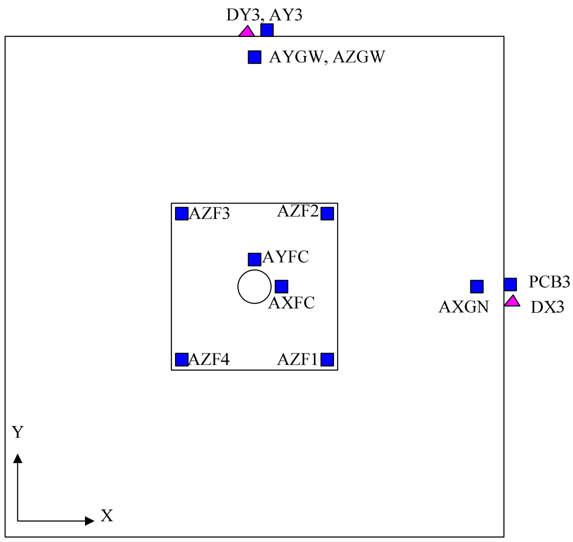

(b) top view

Fig. 3 Arrangement of instrument sensors

Results

1. White noise sweeping

Using the horizontal accelerations at the bottom of the soil (AYBN) and the surface of the soil (AYGW) under the white noise wave, the transfer function between them (AYGW/AYBN) can be built, as shown in Fig. 4, which indicates that the predominant frequency of the soil was about 20Hz. In the same way, the transfer function of the structure model using the horizontal accelerations at the surface of the soil (AYGW) and the top of the mass (AYM) was built, as shown in Fig. 5, from which the predominant frequency of the structure model was about 3.9 Hz.

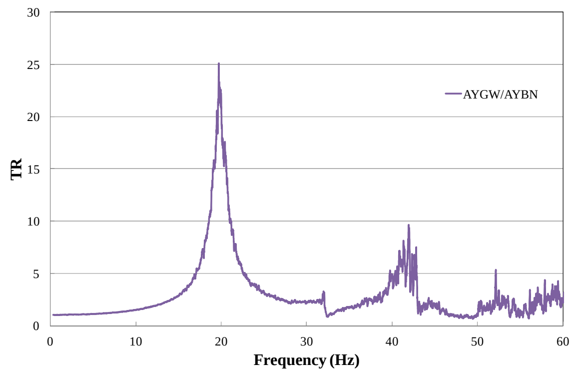

Fig. 4 Transfer function of the soil layer (AYGW/AYBN)

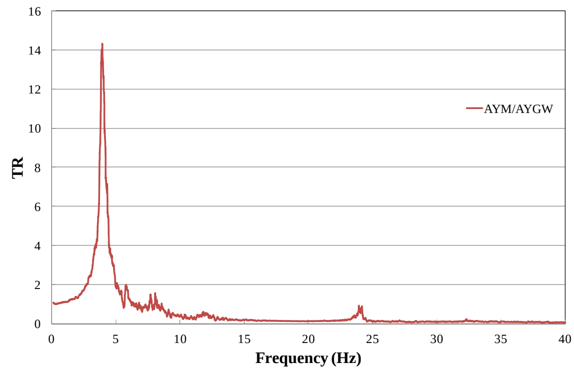

Fig. 5 Transfer function of the structure model (AYM/AYGW)

2. Sinusoid signals

Figure 6 shows the acceleration responses of the structure model and the soil under the sine wave of 4 Hz with a maximum acceleration (Amax) of 0.05g. It could be expected that since the predominant frequencies of the soil and the input motion were not consistent, the acceleration response at the soil surface was very similar to the input motion, as shown in Fig. 6(a). This indicated that the amplification effect of acceleration was insignificant. However, as shown in Fig. 6(b), the top of the mass was significantly amplified due to the consistency of the predominant frequencies of the structure model and the input motion. But, it also could be observed that the maximum acceleration of the main cycles did not exceed 0.2g. With the amplitude of 4Hz sine wave increased to 0.075g, similar trends could be observed, as shown in Fig. 7. It also could be seen that the maximum acceleration of the main cycles was limited to be below 0.21g. The acceleration of the structure seemed to be limited by the moment capacity of the footing. As the acceleration of the input motion was further increased to 0.13g, the acceleration response at the top of the mass was amplified as expected, but still limited to not higher than 0.22g, as shown in Fig. 8. However, during the process of shaking, the structure had a significant twist, as shown in Fig. 9.

Conclusions

Based on the results of this study, the following conclusions can be drawn:

1. The maximum response at the top of the mass had a limit, being controlled by the moment capacity of the footing.

2. Although the seismic response of the structure can be limited by the moment capacity of the footing, too large seismic loading may trigger failure, such as foundation twisting as observed in the test.

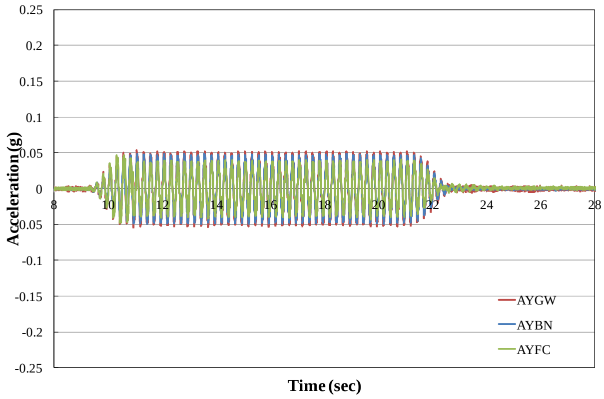

(a) on soil surface and footing,

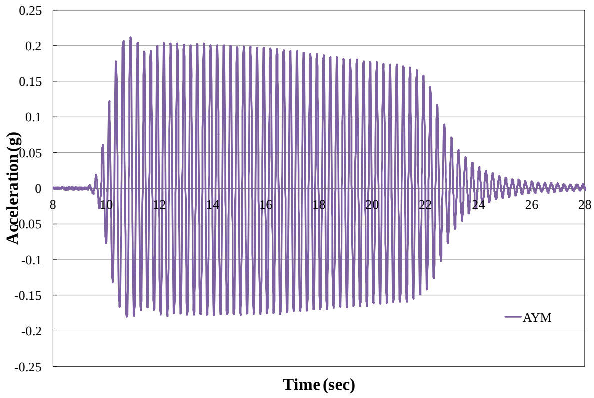

(b) on top of the mass

Fig. 6 Accelerations of the soil and the structure model (Amax=0.05g)

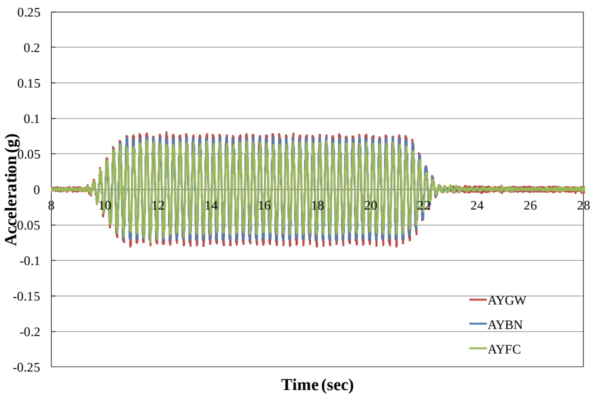

(a) on soil surface and footing

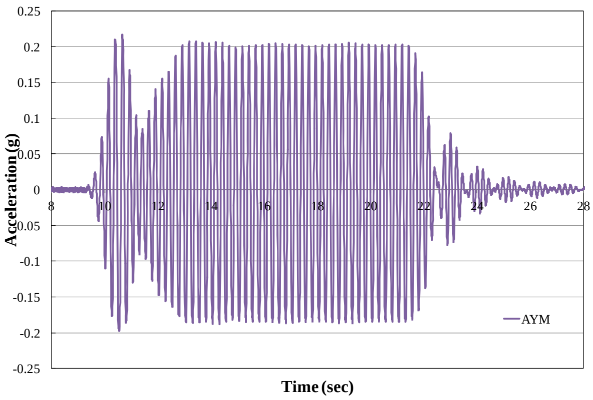

(b) on top of the mass

Fig. 7 Accelerations of the soil and the structure model (Amax=0.075g)

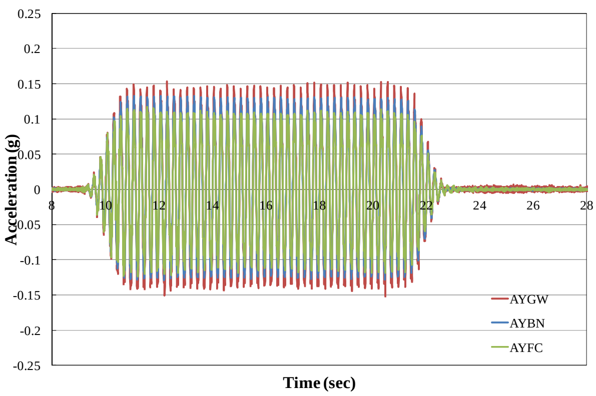

(a) on soil surface and footing

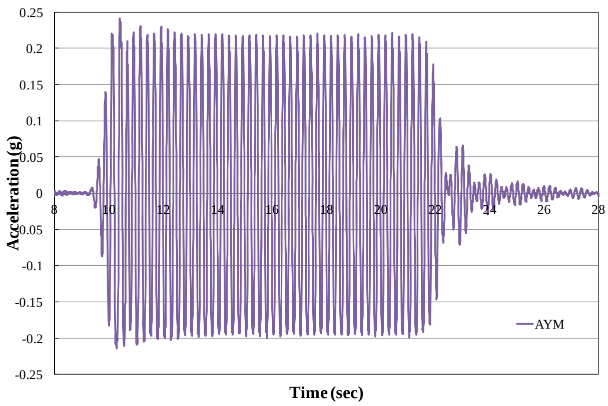

(b) on top of the mass

Fig. 8 Accelerations of the soil and the structure model (Amax=0.13g)

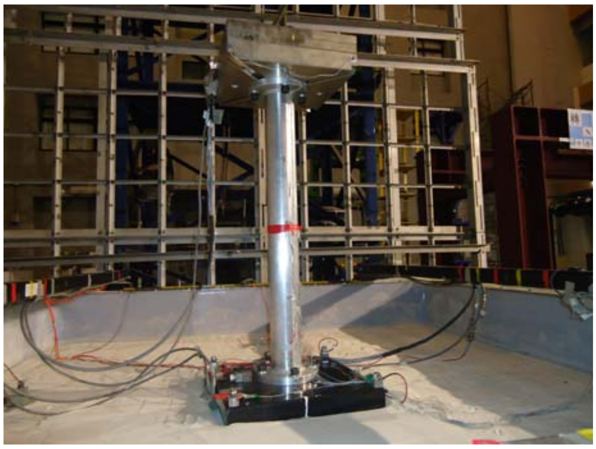

Fig. 9 Foundation twist: side view in orthogonal to the direction of shaking

References

Gajan, S., Kutter, B.L., Phalen, J.D., Hutchinson, T.C., and Martin, G.R. (2005). “Centrifuge modeling of load-deformation behavior of rocking shallow foundations,” Soil Dynamics and Earthquake Engineering, 25, 773-783.

Megro, P.E. and Kawashima, K. (2005). “Rocking isolation of a typical bridge pier on spread foundation,” Journal of Earthquake Engineering, 9(2), 395-414.

Shirato, M., Kouno, T., Asai, R., Nakatani, S., Fukui, J., and Paolucci, R. (2008). “Large-scale experiments on nonlinear behavior of shallow foundations subjected to strong earthquakes,” Soils and Foundations, 48(5), 673-692.

Ueng, T. S., Wang, M. H., Chen, M. H., Chen, C. H., and Peng, L. H. (2006). “A large biaxial shear box for shaking table test on saturated sand,” Geotechnical Testing Journal, 29(1), 1-8.

Time-Dependent Dynamic Characteristics of Model Pile in Saturated Sloping Ground during Soil Liquefaction

Chia-Han Chen[1], Yung-Yen Ko [2], Cheng-Hsing Chen[3] and Tzou-Shin Ueng[4]

陳家漢 [1]、柯永彥 [2] 、陳正興 [3]、翁作新 [4]

Abstract

In order to quantify the relation of reduction of soil stiffness and excess pore water pressure during liquefaction, the test data of a series of shaking table tests on model pile in saturated sand using a large biaxial laminar shear box conducted at the National Center for Research on Earthquake Engineering were analyzed. The test results showed that the frequency changes of model pile was dependent on the response of water pressure ratio. The pile top was mounted with 6 steel disks to simulate the superstructure. In addition, strain gauges and mini-accelerometers were placed on the pile surface to obtain the response of the pile under shaking. Therefore, the model pile can be considered as a sensor to evaluate the changes of dynamic characteristics of soil-pile system during the shaking by using the time-frequency analysis and system identification technique. The relation of stiffness of soil and pore water pressure ratio due to liquefaction during shakings were also studied

Keywords: shaking table test, liquefaction, lateral spreading, pile

Introduction

Many studies on dynamic characteristics of soil under earthquake loading were conducted in order to understand the dynamic behavior of saturated sand under earthquake shaking. Small soil specimens in the laboratory (e.g. Iwasaki et al., 1981; Chiang 1990; Pradhan et al., 1995) , shaking table tests on sand specimens, under either 1 g or centrifugal condition (e.g. Tokimatsu et al., 2005; Ueng et al., 2006; Lee et al., 2012), and in-situ test or seismic records of vertical arrays (e.g. Kostadinov and Towhata , 2002; Kramer et al., 2011) have been used to investigate the relation of soil stiffness and excess pore water pressure, including post-liquefaction. The results of these studies indicated that the generation of excess pore water pressure led to the decrease of effective stress and resulted in reduction of modulus of soil.

The foundation design code in Taiwan suggested to adopt the reduction factors for the mechanical parameters of liquefied soil proposed in Japan Road Association (JRA, 1996) and in Architectural Institute of Japan (AIJ, 1998). However, these regulations are just empirical procedure without solid theories. Therefore, it is necessary to quantify the relation of soil stiffness and excess pore water pressure during liquefaction for better understanding of soil behavior, including post-liquefaction.

Ueng et al. (2009) and Chen et al. (2012) have conducted a series of shaking table tests on model pile in saturated sand using a large biaxial laminar shear box to investigate the soil-structure interaction especially soil liquefaction and lateral spreading, in a liquefiable ground during earthquake. These experimental data were utilized and analyzed to investigate the pile behavior changes with the generation or dissipation of excess pore water pressure during the shaking via the time-frequency analyses and system identification technique.

[1] Assistant Researcher, National Center for Research on Earthquake Engineering, chiaham@narlabs.org.tw
[2] Associate Researcher, National Center for Research on Earthquake Engineering
[3] Professor, Department of Civil Engineering, National Taiwan University
[4] Professor Emeritus, Department of Civil Engineering, National Taiwan University

Shaking Table Tests

Sand specimen and model pile

Clean fine silica sand (Gs = 2.65, e_{max} = 0.918, e_{min} =0.631, D_{50} = 0.30 mm) from Vietnam was used in this study for the sand specimen inside the laminar shear box. The sand specimen was prepared using the wet sedimentation method after placement of the model pile and instruments in the shear box. The sand was rained down into the shear box filled with water to a pre-calculated depth. The size of the sand specimen is 1.880 m × 1.880 m in plane and about 1.40 m in height before shaking tests.

The model pile was made of an aluminum alloy pipe, with a length of 1600 mm, an outer diameter of 101.6 mm, a wall thickness of 3 mm and its flexural rigidity, EI = 75 kN·m^2. The shear box was inclined 2° to the horizontal, simulating a mild infinite slope and the sloping direction of this test was defined as X direction, as shown in Figure 1. The pile was fixed vertically at the bottom of the shear box. Hence, this physical model can be used to simulate the condition of a vertical pile embedded in sloping rock or within a sloping firm soil stratum. The model pile was instrumented and placed inside the shear box before preparation of the sand specimen, attempting to simulate a pile foundation installed with minimum disturbance to the surrounding soil. In addition, 6 steel disks, 226.14 kg in total, were attached to the top of the model pile to simulate the superstructure.

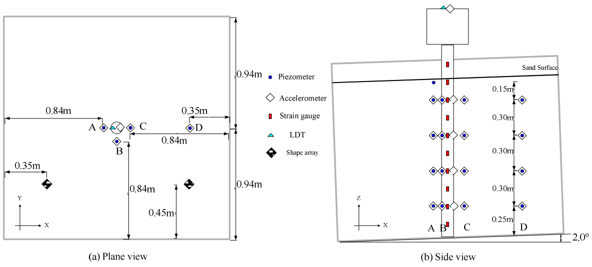

Fig. 1 Instrumentation on the pile and within the sand specimen

Test plan

Shaking table tests were first conducted on the model pile without the sand specimen in order to evaluate the dynamic characteristics of the model pile itself. Sinusoidal and white noise accelerations with amplitudes from 0.03 to 0.05 g were applied in X and/or Y directions. The model pile in saturated sloping ground was then tested under one dimensional sinusoidal (1-8 Hz) and recorded accelerations at the Chi-Chi Earthquake and the Kobe Earthquake with amplitudes ranging from 0.03 to 0.15 g. White noise accelerations with amplitude of 0.03 g were also applied in both X- and Y-directions to evaluate the dynamic characteristics of the model pile within soil and the sand specimen.

Basic results of the test

Shaking table tests on the model pile without sand specimen were conducted to evaluate the dynamic characteristics of the model pile itself. We consider the behavior of model pile without sand specimen under the shakings as a single-degree viscously damped system. Table 1 lists the predominant frequencies of the model pile according to the test data.

The dynamic characteristics of soil and soil-pile system were evaluated by a series of shaking table tests on the model pile within the saturated sand specimen with small amplitude. Table 2 lists the predominant frequencies of the soil and the soil-pile system for the model pile in the saturated sand of various relative densities.

Table 1. Predominant frequencies of the model pile

Mass on pile top	Aluminum pile
	Freq., Hz
No mass	22.9
6 steel disks	2.1

Table 2. Predominant frequencies of the soil and the aluminum pile in soil of different relative densities

Density of soil	Predominant frequency , Hz	
Dr, %	Pile in soil	Soil
11.9	5.0	10.74
26.0	4.76	12.21
42.4	4.40	12.93
70.1	4.40	14.0

Time-Frequency Analysis and System Identification

Time-frequency analysis

Short-time Fourier transform (STFT) is one of the often used time-frequency analysis method. Because STFT is not only easy to be programmed and executed but also able to effectively exhibit the time-frequency characteristics of the signal, it was adopted in this research.

A shaking table test under one-dimensional recorded acceleration at Chi-Chi earthquake with an amplitude of 0.10 g in Y direction was conducted to study the effect of pore water pressure on the pile behavior in liquefiable soil during liquefaction process with a relative density of 27 %. Figure 2(a) shows the measured acceleration time histories of the pile top and input motion. In addition, the time histories of excess pore water pressure ratios (r_u) at different depths of the free-field piezometer array are also shown in Figure 2(b). It can be observed based on the measured the excess pore water pressures that the sand at a shallower depth liquefied at about 20 seconds, and afterwards the excess pore water pressures were totally dissipated at around 45 seconds. The depth of liquefaction was determined based on the measured pore water pressures in the sand specimen and accelerometers on the frames. In this test, the liquefied depth of the sand specimen reached about 45 cm.

Figure 3 shows the result of time-frequency distribution of the measured acceleration on the pile top by STFT method under one-dimensional earthquake shaking. It can also be observed that the time-frequency distribution can be divided into four stages during the shaking: (i) before the shallower depth of soil liquefied prier to 20 sec, the frequency content of the soil-pile system is mainly ranged from 1 - 6 Hz in accordance with the Fourier spectrum of the input motion. (ii) In the period of initial stage of liquefaction during 20 - 30 sec, the main response of soil-pile system ranges from 2 - 3 Hz. (iii) the main response of soil-pile system increases with the time from 3 - 5 Hz during the period f 30 - 50 sec. (iv) after 50 sec, the main response of soil-pile system is kept constant at around 5 Hz. Based on the observation above, one can find that the main frequency of response has a sudden drop when the initial liquefaction occurs, and then the main response recovered with time due to the dissipation of excess pore water pressure. This result provided good evidence that stiffness of soil is strongly affected by the changes of excess pore water pressure, and also in accordance with the previous studies.

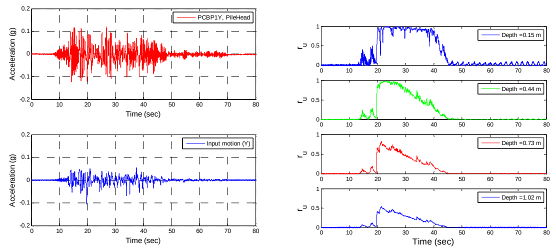

(a) Acceleration (b) Pore water pressure ratio

Fig. 2 Basic results of the chosen test

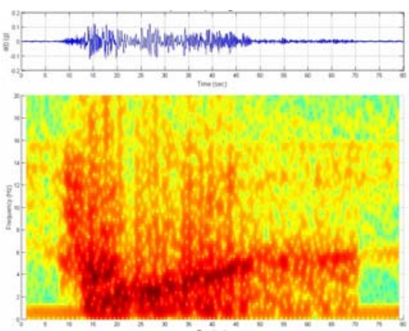

Fig. 3 Time-frequency distribution of the measured acceleration on the pile top by STFT method under 1D earthquake shaking

System identification

In order to quantify the time-dependent predominant frequency of soil-pile system, a method of system identification technique, so-called short-time transfer function (STTF), was proposed by this research to identify the predominant frequency of soil-pile system.

The time-dependent predominant frequency of model pile within saturated sand during earthquake shaking was thus conducted by short-time transfer function method, as shown in Figure 4. Comparing the analysis results of short-time Fourier transform and short-time transfer function in the case of earthquake shaking (Figures 3 & 4), it was found that the results are almost the same. Based on the results of the time-frequency analysis and system identification of the shaking table test, it can be seen that the generation and dissipation behavior of excess pore water pressure has great effects on the stiffness of soil and it would result in the changes of dynamic characteristics of soil-pile system. In addition, the short-time transfer function method can be used to identify the dynamic characteristics of the time-dependent system, and can obtain the reasonable results for the quantification study.

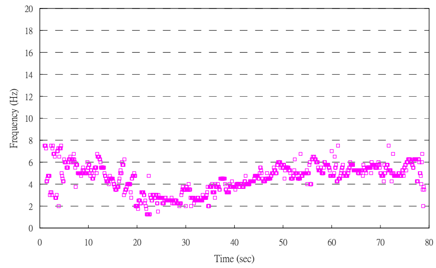

Fig. 4 The time-dependent predominant frequency of model pile within saturated sand during earthquake shaking

Effect of Pore Water Pressure on Predominant Frequency of Soil-Pile System

In order to investigate the relation of pore water pressure and predominant frequency of soil-pile system, the representative parameter should be firstly integrated from all the responses of the pore water pressures in the sand specimen to present the state of the specimen. Because of the stiffness of soil related to the vertical effective stress and vertical effective stress also related to the excess pore water pressure, the average pore pressure ratio ($r_{u,\ ave}$) is used to represent a average state of sand specimen in this study. The idea is to calculate the weighted average of excess pore water ratios of vertical piezometer array in the free field within the specimen, and the weighting is determined by the affecting depth of each piezometer. On the basis of concept of effective stress, the average effective stress ratio time history can be obtained, as shown in Figure 5.

Figure 6 is the comparison of the predominant frequency time history of soil-pile system and the average effective stress ratio time history of sand specimen. It can be found that the trend of the predominant frequency is similar to that of the average effective stress ratio. Furthermore, comparing this result with the predominant frequency of the model pile without and within the soil specimen (respectively

Table 1 & 2), one can find that predominant frequency of the model pile within the soil while liquefaction is only slightly larger than that of model pile without soil specimen. This inferred that the stiffness of the soil almost vanished during the period of initial liquefaction. In addition, the result also indicated that the stiffness of the soil would increase with the dissipation of pore water pressure and the recovery proportion of soil stiffness is directly related to the effective stress ratio of soil specimen.

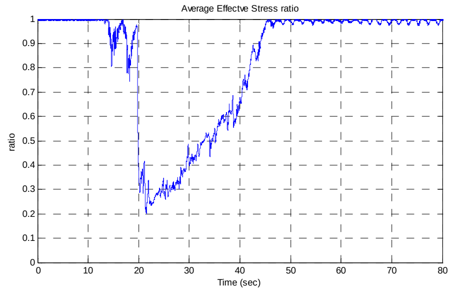

Fig. 5 Average effective stress ratio time history of sand specimen

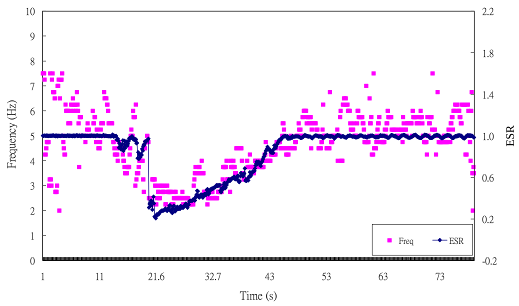

Fig. 6 The predominant frequency vs. average effective stress ratio time history

Conclusions

The time-dependent behavior of model pile in liquefiable soil during liquefaction process have been investigated by using time-frequency analysis and system identification technique based on the test data of shaking table test. The relation of predominant frequency and excess pore water pressure was analysis and discussed. It was found that the stiffness of the soil almost vanished during the period of initial liquefaction. Furthermore, the stiffness of the soil would increase with the dissipation of pore water pressure and the recovery proportion of soil stiffness is directly related to the effective stress ratio of soil specimen. Further analyses of the test data will be performed to obtain more information on the relation of stiffness of the soil and excess pore water pressure and set up a model to assess the seismic behavior of liquefied soil for more reasonable seismic design.

References

Architectural Institute of Japan (AIJ). Recommendations for Design of Building Foundations. Architectural Institute of Japan: Tokyo, 1988. (in Japanese)

Chen CH, Ueng TS, Chen CH. Shaking table tests on model pile in saturated sloping ground. The 15th World Conference on Earthquake Engineering 2012; Paper No.1250, Lisbon, Portugal, September 24-28.

Chiang KL. The behavior of saturated sand subject to undrained monotonic loading after the cyclic loading. MS thesis, National Taiwan University, Taipei, Taiwan, 2005 (in Chinese).

Iwasaki T, Tokida K, Kimata T. Study on the Feasibility of Liquefaction Evaluation Methods for Sandy Ground on Seismic Design. Report No. 1729, Public Works Research Institute, Ministry of Construction, Japan: Tsukuba, 1981. (in Japanese).

Japan Road Association (JRA). Design Specifications for Highway Bridges. Japan Road Association: Tokyo, 1996 (in Japanese).

Kostadinova MV, Towhata I. Assessment of liquefaction-inducing peak ground velocity and frequency of horizontal ground shaking at onset of phenomenon. Soil Dynamics and Earthquake Engineering 2002; 22(4): 309-322.

Kramer SL, Hartvigsen AJ, Sideras SS, Ozener PT. Site response modeling in liquefiable soil deposits. 4th IASPEI / IAEE International Symposium: Effects of Surface Geology on Seismic Motion 2011; Santa Barbara, CA.

Lee CJ, Wang CR, Wei YC, Hung WY. Evolution of the shear wave velocity during shaking modeled in centrifuge shaking table tests. Bulletin of Earthquake Engineering 2012; 10(2): 401-420.

Pradhan T, Kiku H, Sato K. Effect of fines content on behavior of sand during the process to liquefaction. Earthquake Geotechnical Engineering, Ishihara (ed.), Balkema, Rotterdam 1995: 823-828.

Tokimatsu, K, Suzuki H, and Sato M. Effect of inertial and kinematic interaction on seismic behavior of pile with embedded foundation., Soil Dynamics and Earthquake Engineering 2005; 25(7-10):753-762.

Ueng TS, Wang MH, Chen MH, Chen CH, Peng LH. A large biaxial shear box for shaking table tests on saturated sand. Geotechnical Testing Journal 2006; 29(1):1-8.

Ueng TS, Chen CH. Performance of model piles in liquefiable soil during shaking tests. IS-Tokyo, International Conference on Performance-Based Design in Earthquake Geotechnical Engineering— from case history to practice —2009; 523-529, Tsukuba, Japan, June 15-18.

A Study on the Evaluation of Seismic Performance of Sheet Pile Wharves

Yung-Yen Ko[1] Yu-Ning Ge[2] Ya-Han Hsu[3]

柯永彥[1]、葛宇甯[2]、徐雅涵[3]

Abstract

In order to evaluate the seismic performance of sheet pile wharves, including the displacement of quay walls and the stress states of structural members, the finite element method code PLAXIS is utilized in this study to establish the model of sheet pile wharves for dynamic seismic analysis. The nonlinearity of soil and structural members as well as the seismic response characteristics of layered ground are considered. Firstly, a scale-model shaking table test conducted by National Cheng Kung University and the Harbor and Marine Technology Center is simulated to verify the analysis method. Then, a sheet pile wharf in the Port of Hualien is adopted for a case study using the time history of a representative earthquake, and the obtained seismic performance is compared with its design conditions to confirm whether the design requirements are achieved. The results of this study can be applied to the seismic evaluation of sheet pile wharves, and can be used in the examination procedure in performance design.

Keywords: sheet pile wharf, seismic performance, PLAXIS, nonlinear dynamic seismic analysis

Introduction

Earthquake disasters are inevitable in Taiwan because it is located in the seismic active region of the Western Pacific Rim. One of the most representative was the Chi-Chi earthquake that occurred on Sep. 21, 1999. It caused a large number of casualties, heavy property losses, and had a massive impact to the society. In addition, Taiwan has a widely varied topography, including mountains, valleys, plains, and coasts. Thus, the geotechnical disasters induced by earthquakes are highly noticeable.

Because Taiwan is an island, marine transportation, both domestic and international, is critical. The failure of the retaining structures of wharves is one of the most common geotechnical disasters induced by earthquakes. For example, some of the wharves in the Port of Taichung were severely damaged in the Chi-Chi earthquake. Because this kind of failure usually occurs along the entire wharf simultaneously, it significantly affects the serviceability of the wharf. Therefore, direct and indirect losses and the cost of restoration may result in a huge economic expense.

In order to reasonably assess the displacement of the quay wall and the stress states of the structural members of sheet pile wharves for a determination of their performance level, the evaluation of the seismic performance of sheet pile wharves was investigated in this study. The focus was on the rigorous dynamic analysis method. The results can be applied to the seismic capacity evaluation of sheet pile wharves, and can be used as a reference for the examination procedure in performance design.

Evaluation of the Seismic Performance of Sheet Pile Wharves

1. Failure Modes and Damage Criteria:

A sheet pile wharf is composed of a main sheet pile wall, tie rods, and anchors (sheet piles or piles). Its seismic response is influenced by the interaction of the sheet pile wall and the soil body in front of and behind the wall. Based on case history studies, the World Association for Waterborne Transport Infrastructure (PIANC) (2001) proposed typical failure modes of sheet pile wharves during

[1] Associate Researcher, National Center for Research on Earthquake Engineering, yyko@narlabs.org.tw
[2] Associate Professor, Department of Civil Engineering, National Taiwan University, louisge@ntu.edu.tw
[3] Graduate Student, Depart of Civil Engineering, National Taiwan University, r02521101@ntu.edu.tw

earthquakes, as shown in Fig. 1, including the over displacement of the quay wall and the settlement or cracking of the apron, which are the because the dynamic earth pressure and water pressure cause the stress state of the structural members to exceed their designed strength, as well as the settlement of the apron, which is due to plastic failure or soil liquefaction at the embedment under dynamic seismic loading.

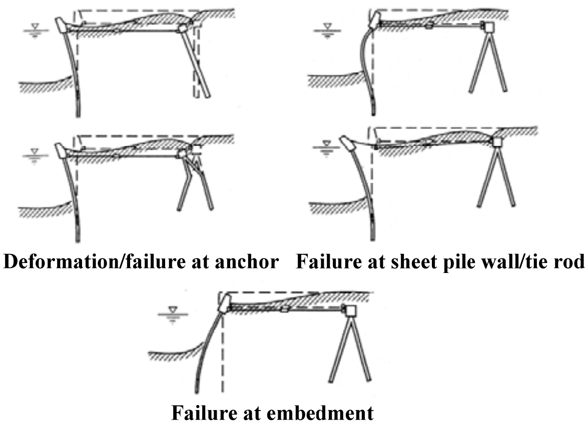

Fig. 1 Failure modes of the sheet pile wharf.

Table 1 gives the damage criteria for sheet pile wharves according to the state of structural damage and serviceability. The criteria which were based on the residual displacement at the top of the sheet pile wall were proposed by Uwabe (1983), while those based on the stress states at structural members were proposed by PIANC (2001). The definitions of the damage levels are:

I: Minor or no structural damage; little or no loss of serviceability.
II: Controlled structural damage; short-term loss of serviceability.
III: Extensive structural damage in near collapse; long-term loss of serviceability
IV: Complete structural damage; complete loss of serviceability.

It is noted that the sheet pile wall below mudline has a stricter criterion because it is difficult to repair.

2. Model for Seismic Analysis of Sheet Pile Wharves:

When seismic analysis of a sheet pile wharf is performed, it is necessary to consider the soil-structure interaction for an accurate assessment of its seismic response. In general, methods for seismic analysis of wharves include pseudo-static analysis, simplified dynamic analysis, and rigorous dynamic analysis which uses the finite element method (FEM) or the finite difference method (FDM). In the rigorous dynamic analysis, the variability of ground motions can be represented, the non-linearity of the materials and the interaction between soil and structure can be properly considered, and the resulting analysis results include the displacement and stress states of the structural members and soil, which can be used for the determination of the damage state according to the corresponding damage criteria. Therefore, rigorous dynamic analysis was adopted in this study and the FEM code PLAXIS, which was developed for geotechnical engineering analysis, was used because FEM can simulate the structural members well and because the model can be easily generated.

The plane-strain analysis was adopted because of the geometry of the wharf. The ground was modeled by 6-node plane strain triangular elements. The Mohr-Coulomb criterion was used to model the plastic failure of the soil. Undrained analysis was used to simulate the generation of excess pore water pressure so that the degradation of soil strength due to the decrease of effective stresses can be considered. However, PLAXIS cannot model the dissipation of excess pore water pressure in dynamic analysis so that it is not able to simulate the recovery of soil strength after the effective stresses increase.

In order to simulate the characteristics of the seismic response of layered ground, a rigid link was applied to tie together the two nodes at both ends of each layer to force their horizontal displacement to be consistent while allowing for relative displacement between layers. Thus, the ground can behave globally as a 1D shear beam, which is a common assumption in ground response analysis. In order to reduce the undesirable effect of fictitious reflections when a model with a finite domain was used to simulate the ground with a semi-infinite domain, absorbent boundaries were imposed at both edges of the ground model.

The sheet pile wall and the anchor were modeled by the plate element, while the tie-rod was modeled by the axial force element. The nonlinear behavior of the structural members was simulated by specifying the yielding moment of the plate element and the yielding tension of the axial force element.

Table 1 Damage criteria for sheet pile wharves.

Damage level	Residual displ. at wall top	Sheet pile wall		Tie rod	Anchor
		Above mudline	Below mudline		
I	<30 cm	Elastic	Elastic	Elastic	Elastic
II	30-100 cm	Plastic (less than ductility factor)	Elastic	Elastic	Elastic
III	100-200 cm	Plastic (less than ductility factor)	Plastic (less than ductility factor)	Plastic (less than ductility factor)	Plastic (less than ductility factor)
IV	>200 cm	Plastic (beyoond ductility factor)	Plastic (beyoond ductility factor)	Plastic (beyoond ductility factor)	Plastic (beyoond ductility factor)

Simulation of the Scale-Model Test

A scale-model shaking table test of the anchored sheet pile was conducted by National Cheng Kung University and the Harbor and Marine Technology

Center at the National Center for Research on Earthquake Engineering using the large biaxial laminar shear box (Chang et al., 2012). In order to verify the analysis method proposed in the previous section, a numerical simulation of this test was performed in this study, and the results of the analysis and the test were compared.

Fig. 2(a) shows the test setup, in which the backfill and the bed soil layer were prepared using Vietnam silica sand by the wet sedimentation method. A plate with a thickness of 5 mm and bars with a diameter of 10 mm made of aluminum (E = 71 GPa) were used as the sheet pile wall and the anchor piles, respectively. Steel wires with a diameter of 1.6 mm were used as the tie rods. The input motion of the adopted test case was a 15-second sinusoidal acceleration with an amplitude of 0.2 g and a frequency of 1 Hz. In this case, the excess pore water pressure increased significantly and the backfill was therefore liquefied, causing the overturning of the anchor piles and a displacement of 27 cm at the top of the sheet pile wall.

According to the previous section, the finite element (FE) mesh of the analysis model was generated, as shown in Fig. 2(b). In order to simulate the seismic behavior of level ground, the laminar flexible boundary of the shear box used in this test was formed by layers of movable frames (Ueng et al., 2003). Thus, a rigid link can also be applied between the two nodes at both ends of each layer of the frame. The soil properties were specified according to the predominant frequency of the specimen, with the variation of the soil stiffness with respect to the depth considered.

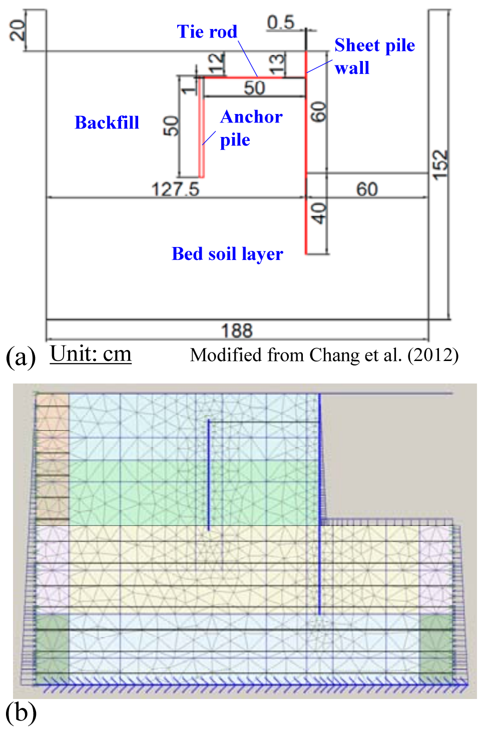

Fig. 2 Scale-model shaking table test of the anchored sheet pile: (a) test setup; (b) FE mesh

Fig. 3(a) shows the deformed mesh after the excitation. The obvious settlement of the backfill can be observed, which is a result of softening caused by the rise of the excess pore water pressure. The sheet pile wall and the anchor plate were therefore apparently tilted, which conforms to the observations in the test. Fig. 3(b) shows the lateral displacement of the sheet pile wall. The analyzed maximum displacement at the top of the sheet pile wall was 26.5 cm, which is quite close to the test result. Hence, the analysis model can simulate the global failure behavior of the anchored sheet pile quite well.

Fig. 3(c) depicts the distribution of the moment in the sheet pile wall when the maximum moment was reached. The maximum moment obtained from the analysis was 142.4 N-m, which was approximately twice the value from the test (69.03 N-m), and it occurred at a depth of 40 cm in the analysis, which was less than the 60-cm depth in the test. In addition, it can be observed that the moment curve from the analysis had an inflection point (where the moment is zero) at a depth of around 70 cm, and had a negative moment peak at a depth of 85 cm. That is, the sheet pile wall exhibited a double curvature behavior. However, the moment curve from the test showed no inflection point and negative moment.

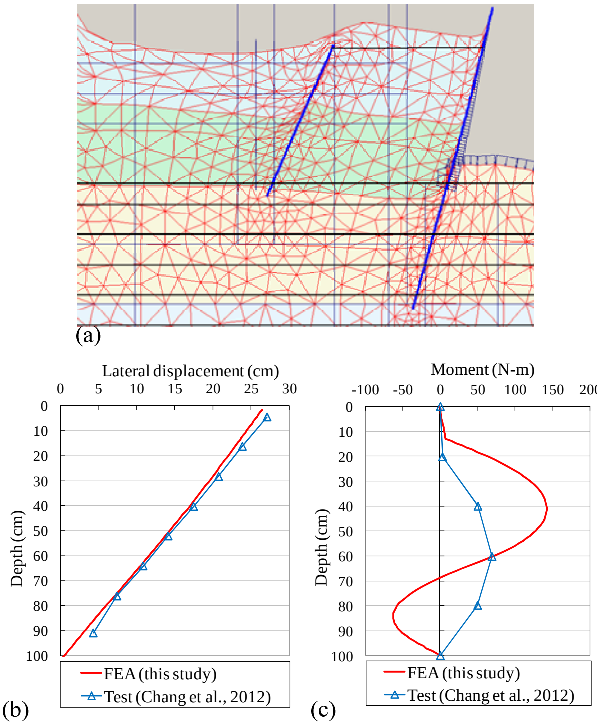

Fig. 3 Simulation results of the scale-model test: (a) deformed mesh (true scale), (b) lateral displacement of the sheet pile wall, and (c) the moment in the sheet pile wall.

A possible reason of the mentioned phenomenon is that the soil at the lower end of the sheet pile wall was weakened as a result of the disturbance from the pile tip during the excitation. Therefore, the soil could not provide sufficient reaction to make the sheet pile exhibit double curvature, and the analysis model did not simulate this soil weakening phenomenon. Although the analysis gave a more conservative result at the maximum moment, the difference in the location of the occurrence might lead to a misjudgment of the failure position and the damage level. Therefore, it is necessary to improve the analysis method in order to provide a better simulation of the structural behavior of the sheet pile.

Case Study of a Sheet Pile Wharf in the Port of Hualien

Wharf No. 8 in the Port of Hualien was adopted for the case study of sheet pile wharves. Its main sheet pile wall is composed of steel sheet piles with a yielding moment of 540 kN/m/m. The tie rods have a yielding tension of 500 kN/m and the anchors are composed of reinforced concrete (RC) plates with a yielding moment of 200 kN/m/m. Concerning the geological conditions of the site, the depth of the bed rock is around 10-20 m, and the layers above the bed rock are mainly composed of gravels. An analysis model was established using the PLAXIS code according to the parameters given above.

The input motion was a time history recorded at the Hualien Weather Station (HWA019) of the Hualien offshore earthquake that occurred on March 31, 2002, and it was scaled to have a peak ground acceleration (PGA) of 0.33 g, which was the 475-year return period design PGA for the Port of Hualien.

A dynamic seismic analysis was performed using the FE model and the input motion. The deformed mesh, the moment distribution along the sheet pile wall, the tension of the tie-rod, and the moment distribution along the anchor plate are shown in Fig 4. The maximum residual displacement at the top of the sheet pile wall is 51.4 cm, and the maximum moment in the sheet pile wall is 465.5 kN-m/m, occurring above the mudline. The maximum moment in the anchor plate is 129.3 kN-m/m, occurring at the end of the tie-rod. The tension of the tie-rod is 326.6 kN/m. None of the structural members yielded.

Although the sheet pile wall above the mudline did not yield, the moment value was close to the yielding moment. Moreover, the residual displacement at the wall top exceeded 30 cm. Consequently, according to Table 1, the damage level in this case was degree II, which corresponds to a temporary loss of serviceability. If the wharf can be regarded as an important structure with a performance grade A, its damage level should be no higher than degree II under an earthquake with a 475-year return period. Thus, Wharf No. 8 in the Port of Hualien can meet its design requirements, and the seismic analysis model for the sheet pile wharf proposed in this study was verified to be practical.

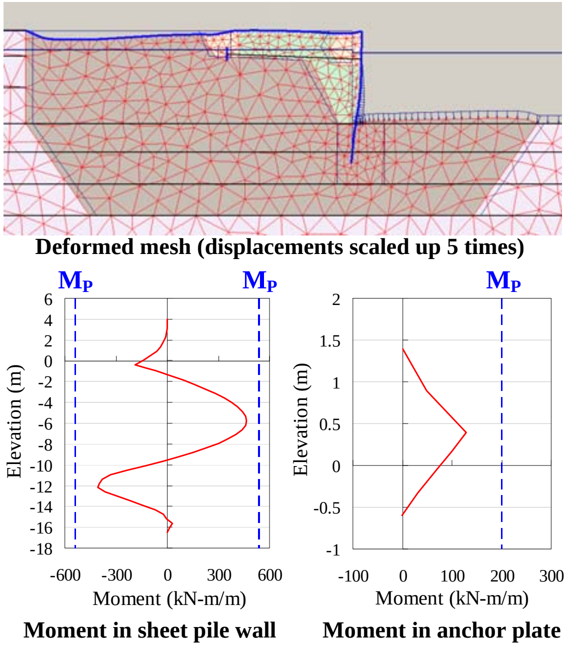

Fig. 4 Analyzed seismic response of Wharf No. 8 in the Port of Hualien (PGA = 0.33 g).

References

International Navigation Association (PIANC) (2001), Seismic Design Guidelines for Port Structures, A.A Balkema Publishers, Rotterdam.

Uwabe, T. (1983), "Estimation of earthquake damage deformation and cost of quaywalls based on earthquake damage records," Technical Note of Port and Harbour Research Institute, No.473, pp.197 (in Japanese).

Ueng, T.-S., Chen, C.-H, Peng, L.-H, Li, W.-C. (2003), Large-Scale Shear Box Soil Liquefaction Tests on Shaking Table (II)- Preparation of Large Sand Specimen and Preliminary Shaking Table Tests, Research Report of National Center for Research on Earthquake Engineering (in Chinese).

Chang, W.-J., Chen, J.-F., Wu, P.-R., Hsieh, M.-J. (2012), "The Study of anchored sheet pile responses in liquefied soil by dynamic model test," The 34th Ocean Engineering Conference in Taiwan, Tainan (in Chinese).

High Resolution Tomography Images in Southwestern Taiwan: Applications in Seismology

Strong Wen [1] Yi-Zen Chang [2] Che-Min Lin [3] and Kuo-Liang Wen [4]

溫士忠 [1]、張議仁 [2]、林哲民 [3]、溫國樑 [4]

Abstract

In this study, we adopt the damping least-square inversion method to investigate Vp structures and Vp/Vs ratios of the crust in southwestern Taiwan. Previous studies have shown that velocity structure can be used as an indicator of the geometry of a fault and the estimation of strong motion. Therefore, the goal of this research is to obtain a high resolution velocity structure and seismic characteristics with respect to the wave propagation in this area. Finally, the distribution of the Vp/Vs ratio and its association with fault activities is also investigated. Our results indicate that the variations in velocity structure in southwestern Taiwan are caused by local geological structures, such as fault crossings. We also find that most earthquakes occur in areas that have Vp/Vs gradients that vary greatly. In addition, through the simulation of strong earthquakes that have occurred in this area, the obtained 3D velocity structure can be more reliably utilized in seismic hazard assessment.

Keywords: Vp、Vp/Vs、complex structure、seismic wave propagation

Introduction

In recent years, several major communications and transportation systems have been built in the Yun-Chia-Nan area (see Figure 1) to improve its economic development. As such, it is extremely important to analyze the accumulation of seismic energy in the upper crust and seismic potential in this area. In this study, we investigate the high resolution velocity structure in southwestern Taiwan and its tectonic implications. Therefore, through the velocity structure and estimation of strong earthquake, we want to explore the relationship between seismogenic zones and seismicity in southwestern Taiwan. In addition, we also expect to provide useful information about the great significance for earthquake disaster prevention in this region.

The National Center for Research on Earthquake Engineering (NCREE) and the Central Weather Bureau Seismic Network (CWBSN) of Taiwan have set up seismic monitoring systems around Taiwan and its outlying islands. This dense seismic network and broadband seismometers provided us with the high-quality travel time records for P and S waves required in this study. Not only have we been able to analyze this data to precisely determine earthquake locations, but we have also been able to obtain 3-D tomographic velocity structures beneath this area. In addition to the Vp and Vs structures, we are also interested in studying the Vp/Vs ratio. This ratio Vp/Vs reflects rock porosity, the degree of fracture and fluid pressure in the rock, and is therefore a key parameter for understanding the properties of crustal rocks (Walck, 1988; Chen et. al., 2001). Furthermore, recent studies have shown that the Vp/Vs ratio can also provide useful information about geological evolution and tectonic variations. The result can be a reference to the estimation of strong motion and the distribution of PGA in understanding the spatial and temporal variations in southwestern Taiwan.

3D Wave propagation

The Spectral Element Method (SEM) was first put

[1] Associate Researcher, National Center for Research on Earthquake Engineering, scwen@narlabs.org.tw.
[2] Assistant Researcher, National Center for Research on Earthquake Engineering, yzchang@narlabs.org.tw
[3] Associate Researcher, National Center for Research on Earthquake Engineering, cmlin@narlabs.org.tw
[4] Professor, Dept. of Earth Science, National Central Univ., wenkl@narlabs.org.tw

forward in the 1980s (Babuska *et al.*, 1981). Now the method is widely used for solving problems in the simulation of global wave propagation (Komatitsch and Tromp, 2002a,b; Chaljub *et al.*, 2003; Wen et al., 2007). This study will utilize this method to simulate seismic waves traveling through complex structures. SEM is a kind of high-order differential equation in the physical field. It is an efficient tool to study the various types of fluctuation characteristics in a 3D structure. One of the main reasons for adopting this method is that in order to exhibit complicated wave phases generated by seismic waves traveling through a geological structure, precise method is required to simulate the boundary conditions, irregular and non-homogeneous interface, and situations when the structure involves a strong velocity contrast and topographical effect. These effects cause the ground to shake in a complicated manner, and have decisive influence on the structural design of buildings.

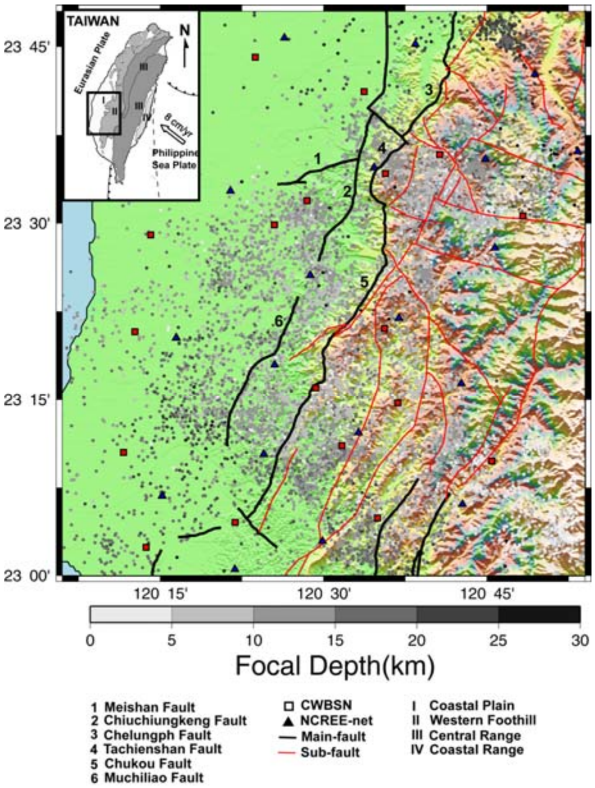

Figure 1. The locations of the faults and the stations of the CWBSN in our research area

Southwestern Taiwan can be divided into two main areas: the Western Foothills (WF) and the Western Coastal Plain (WCP). WF is mainly composed of Neogene clastic sediments and partly of Oligocene strata. The dominant rock types are an interlamination of sandstone and shale. The thickness of the shale and mudstone layers increases from north to south. In order to examine the precision of SEM, we simulated the strong wave propagation in southwestern Taiwan by using the obtained velocity structures (see Figure 2).

3D Tomography model

This study uses the travel time data of P and S waves from the period 2012 to 2014 recorded by the CWBSN and NCREE. A damping least-square inversion method was used to determine the Vp structure and Vp/Vs ratio in the crust and upper mantle of the region. The programs and routines used to perform the 3-D inversion were originally developed by Thurber (1983) and Eberhart-Phillips and Michael (1998), and have since been modified by others to obtain both the Vp and the Vp/Vs ratio. The latitude and longitude ranges of our study area were 22.9°N - 23.8°N and 120.1°E - 121.°E. Many seismic events have occurred in the region of interest. In order to improve the resolution of the tomographic inversion and achieve uniform ray distribution around the volume source, we chose events with epicenter location errors of less than 5 km and events with more than six readings of the P and S waves. To ensure the quality of the seismic data, the ERH (error in horizontal components) and ERZ (error in vertical component) were set at less than 5 km and 10 km, respectively. Under the above conditions, we were able to select 11,000 events with 99,698 P-wave and 95,075 S-wave arrival times for use in this study. We chose an *a priori* 1-D P-velocity model parameterized by horizontal layers of constant velocities that could roughly reproduce the main features of the known velocity structure obtained by Yeh *et al.*, (2013). An uneven 3-D grid formed through a trial-and-error process parameterized the 3-D structure. Several other cases were also taken into account during the process: station spacing, estimated resolution, and the desired spatial resolution around the fault plane. Table 1 lists the one-dimensional initial velocity model (Yeh et al., 2013) that couples with the grid node from the top surface to a depth into the inversion of more than 75km. The dimensions of the mesh were 5km x 5km. The effect of station elevation on the 3-D tomographic inversion was also considered in our calculations.

Results and Discussions

In this section, we discuss our results in two parts. The first part discusses the results in terms of how the velocity structures and Vp/Vs ratios were derived, and is accompanied by an examination of the checkerboard test. Here, the epicenters are relocated and the velocity structures are calculated through an iterative process. The second part of our discussion involves examining velocity structures in the estimation of strong motion. These profiles are almost perpendicular to the Chukou fault. Thus we can outline the relationship among the velocity structures, fault zones and seismicity.

As the distributions of the seismic events were observed uniformly, the results show good resolution in the selected zones, including the Chukou fault and in a band roughly 15 km wide running along the sides of the fault (see Figure 2). However, the resolution at depths from 0 to 3 km and from 22 to 35 km is relatively poor. At depths between 0 and 3 km, this problem may be due to the incident angles being almost perpendicular to the surface, meaning that the lateral resolutions of velocity are lower. Between 22 and 35 km, a reasonable explanation may be that only a few selected events actually occurred at such depths. The high resolution indicates that the seismic rays crossed most of the area, and ought to be reliable in helping to determine the geological structures more precisely beneath the Yun-Chia-Nan area.

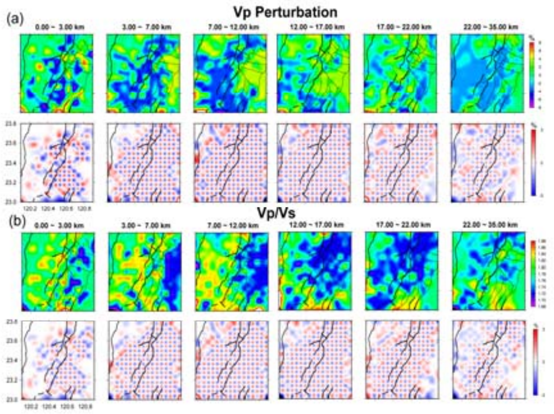

Figure 2. The checkerboard tests give results for 3-D tomographic Vp and Vp/Vs structures at four depth ranges (0-3km, 3-7km, 7-12km, 12-17km, 17-22km). The black lines represent the locations of the main faults in the research area

Figure 2 shows numerous seismic events in each layer. However, most are located in the shallow layers at depths from 3 to 22 km. Therefore, in our inversion process it is not possible to avoid the case where seismicity is not uniform. Between depths of 0 and 7km, the high and low values of Vp have a dispersed distribution. We also observed that there exist low Vp anomalies scattered within the vicinity of the fault zone. At depths between 7 and 17 km, we found that the low Vp anomalies increase with depth and expand in a southwesterly direction. This may be related to the existence of shallow sediment structures beneath this area (Ho, 1986). There are several cluster events in each layer and most lie within the low Vp anomalies. In the vicinity of the fault zones, a high Vp/Vs ratio anomaly is due to the increase in pore pressure, and therefore decreases in the S wave velocity. We also observed that a high Vp/Vs ratio anomaly broadens from the WF to the WCP between 3 and 17 km, and that the low Vp/Vs ratio zone extends to the CMR with increasing depth (see Figure 2). The likely reason for this is that rock formations are older and denser beneath the CMR, and so contain less fluid or SiO_2, which leads to the lower Vp/Vs ratio. Our results indicate that most seismic events are located in areas with Vp/Vs gradients that vary greatly or that have a high Vp/Vs ratio.

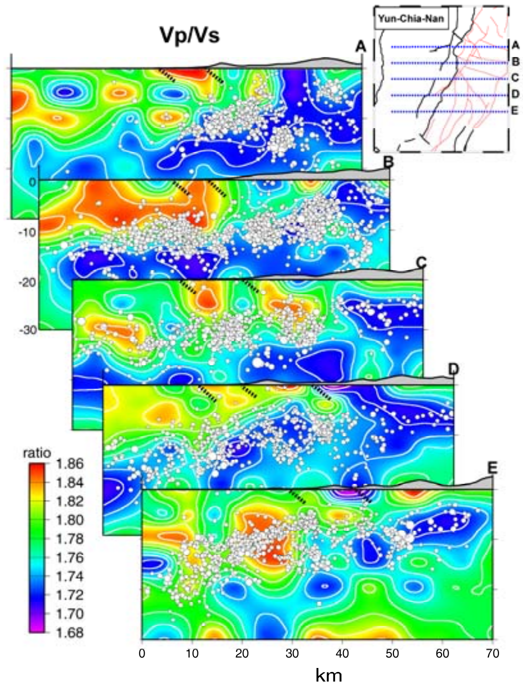

Figure 3. Tomographic Vp/Vs ratio structure along the profiles A~E. Circles represent seismic events used in this inversion. The dotted lines indicate faults

In Figure 3, profiles A~E show that anomalies exist in the Vp and Vp/Vs cross section, and also potentially indicate an eastward leaning fault geometry beneath the Chukou fault zone. This implies that the fault is the Chukou fault. On the west side of the fault, there is also a low Vp, high Vp/Vs anomaly area, which tends to dip toward the west, and exhibits an earthquake cluster. The west side of the Chukou fault zone exhibits anomalous activity, possibly owing to the high pore pressure, which can lead to rupture. Therefore, the abnormal area can be interpreted as an oversaturated pore pressure zone. We conclude that high seismicity exists in zones that exhibit a low P wave velocity and where the gradients of the Vp/Vs ratio vary greatly in each profile. Hence, we can observe a seismic zone dipping toward the west, and believe that this lies around a blind fault zone. The geological implications of this phenomenon with regard to southwestern Taiwan are worth further investigation. In addition, the high resolution velocity structure is necessary to simulate wave propagation. The numerical mesh is composed of 96 x 96 x 23 elements with an approximate frequency of 1 Hz. Due to the source near-field effect, we adopted the rupture model that was derived from Wen et al.,(2008) to simulate the 1022 Chiayi earthquake (see Figure 4a). The simulated PGA map is plotted in Figure 4b. We can observe more complex rupture behavior near the source area than the point source model.

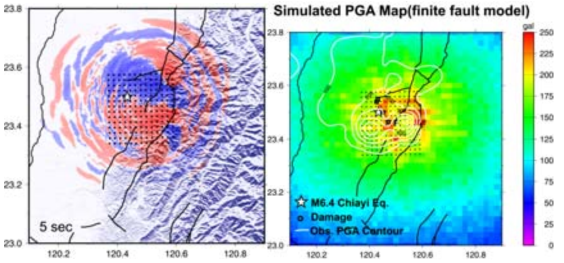

Figure 4. The simulated wave propagation in 1022 Chiayi earthquake and the related PGA map. The white contour lines are indicated as the observed PGA values

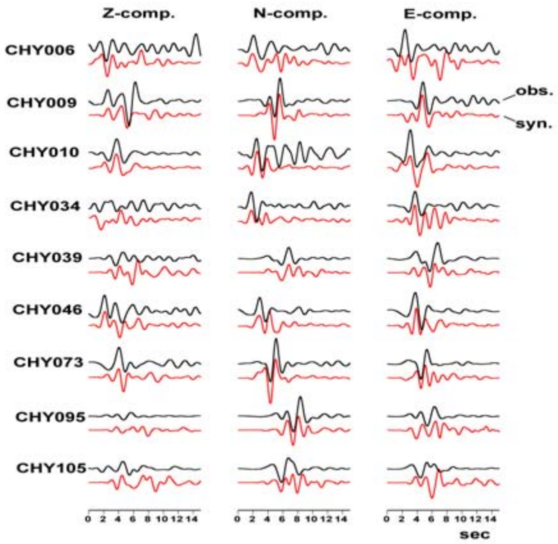

Figure 5. Fitting the observed and synthetic waveforms to the 1022 Chiayi earthquake. The band pass filter was between 0.1~1 Hz

In Figure 5, we illustrate the comparison between the observed and synthetic data in the stations. The station names are listed on the left side, the black lines are the observed waveform, and the red lines indicate synthetic data. The waveform fitting is highly similar for most stations which imply that the obtained model is reliable; however, for some stations, the fitness is poor owing to shallower layers and the site effect. From the examined model, we can observe the complex phases when the wave travels through 3D velocity structures and the near surface layers play an important role in the site response.

Conclusions

In this study, we applied a damping least-square inversion method to investigate, via 3-D tomographic inversion, the Vp structures and Vp/Vs ratios of the crust in southwestern Taiwan using body wave travel time data. Our results indicate that we are able to not only locate earthquakes, but also deduce the relationship between the seismicity and the regional geological structures. An additional finding was that most earthquakes occurred in areas that have Vp/Vs gradients that vary greatly. From our study, we inferred that there might exist a west-dipping fault in the western Chukou fault region. However, this inference needs further study. The waveform fitting is highly similar for most stations and the lower traveling time error implies that the obtained velocity model is more reliable. The 3-D numerical model from this study is helpful in improving the accuracy of earthquake location, and is also an important factor in estimating strong motion. Therefore, for southwestern Taiwan, the results are also of great significance in earthquake prevention and mitigation.

References

Babuska, I., and M. R. Dorr. (1981). Error estimates for the combined h and p versions of the finite element method, *Numer. Math*., **37**, 257-277.

Chen, C.H.,W.H. Wang, and T. L. Teng (2001). 3-D Velocity Structure Around the Source Area of The Chi-Chi Earthquake,1999,Taiwan： Before and After Mainshock , *Bull. Seismol. Soc. Am.*, **91**, 1010-1027

Ho, C.S. (1986). A synthesis of the geologic evolution of Taiwan, *Tectonophysics* 125, 1-16.

Komatitsch, D., and J. Tromp (2002a). Spectral-element simulations of global seismic wave propagation, I. Validation, *Geophys. J. Int.*, **149,** 390–412.

Komatitsch, D., and J. Tromp (2002b). Spectral-element simulations of global seismic wave propagation, II. 3-D models, oceans, rotation, and self-gravitation, *Geophys. J. Int.*, **150,** 303–318.

Thurber,C. H.(1983). Earthquake locations and three-dimension crustal structure in the Coyote Lake area,central California, *J. Geophys. Res.*, **88**,8226-8236.

Walck, M. C. (1988). Three-Dimensional Vp/Vs Variation for the Coso Region,California, *J. Geophys. Res.*, **93**, 2047-2052.

Wen S., C. H. Chen, and T. L. Teng (2008) Ruptures in a Highly Fractured Upper Crust, *Pure and Applied Geophysics*, **165**, 201-213.

Yeh, Y-L., Wen, S., Lee, K-J., Chen, C-H. (2013), Shear-wave velocity model of the Chukuo Fault Zone, Southwest Taiwan, from Cross Correlation of Seismic Ambient Noise, Journal of Asian Earth Sciences, doi: http : // dx.doi.org /10.1016/ j.jseaes. 2013.07.023.

Preliminary Analysis for Downhole Arrays

Chun-Hsiang Kuo[1], Hung-Hao Hsieh[2], Che-Min Lin[1], Kuo-Liang Wen[3], and Chih-Wei Chang[4]

郭俊翔[1]、謝宏灝[2]、林哲民[1]、溫國樑[3]、張志偉[4]

Abstract

In order to understand site amplification of seismic wave propagation in the near surface layers, National Center for Research on Earthquake Engineering (NCREE) of National Applied Research Laboratories (NARL) installed a downhole seismic array near the edge of the Taipei Basin. Five seismometers were installed at the surface and at depths of 20, 30, 58, 78 m. The depth of the interface between sediment and bedrock is 58 m. Therefore, this array is able to analyze the seismic site effect from the bedrock to the surface inside the Taipei Basin. Moreover, one downhole array includes a surface seismometer and three downhole seismometers at depths of 20, 30, and 70 m. It was installed at the Observatory Experiment for Earthquake Precursors of the National Dong Hua University (NDHU), in order to observe and analyze the characteristics of near source seismic waves. The two sites were investigated and logged prior to array installation. Most of the recordings belong to zero grade with Peak Ground Acceleration (PGA) < 0.8 gal. The largest one is only three grade (PGA between 8 and 25 gals) at both arrays because the time of observations is short and the resolution of the seismometers is high (24 bits). Although strong motion recording is not currently available, we used weak motion data to analyze the attenuation of PGA with increasing depth.

Keywords: Downhole seismometer; Ambient noise; Peak Ground Acceleration

Introduction

Many downhole arrays have been installed in Taiwan by the Taiwan Power Company and U.S. Electric Power Research Institute (EPRI). The Lotung Large Scale Seismic Test (LLSST) located in Lotung town, Ilan County was the first phase of the international project which included three types of accelerometers (structural, free-field, and down-hole) and was installed with the assistance from the Institute of Earth Science (IES), Academia Sinica. The second phase is called the Hualien Large Scale Seismic Test (HLSST). It was located in Hualieh City and it also used three types of accelerometers. The recordings of the two projects were widely used by many researchers in seismology and earthquake engineering. The Central Geological Survey of the Ministry of Economic Affairs (CGS, MOEA) started to drill deep boreholes and installed accelerometers at depths from the bedrock to the surface to monitor the propagation of seismic waves and analyze the influence of the basin effect on seismic waves (Wen *et al.*, 1995; Huang *et al.*, 2010). Several stations were closed after the end of the project. The strong motion downhole arrays were transferred to IES and restarted to install several new stations of downhole arrays in recent years. In order to monitor the structural damage and soil liquefaction at the sediments and polder lands in the important harbors caused by earthquakes, the Harbor and Marine Technology Center, Institute of Transportation, Ministry of Transportation and Communications (HMTC, IOT, MOTC) installed downhole arrays at important harbors as well as dynamic pore pressure sensors at different depths to

[1] Associate Researcher, National Center for Research on Earthquake Engineering, chkuo@ncree.narl.org.tw; cmlin@ncree.narl.org.tw
[2] Assistant Researcher, National Center for Research on Earthquake Engineering, hhhsieh@ncree.narl.org.tw
[3] Professor, Dep. of Earth Science, National Central University and Division Manager, National Center for Research on Earthquake Engineering, wenkl@ncree.narl.org.tw
[4] Assistant Technologist, National Center for Research on Earthquake Engineering, chihwei@ncree.narl.org.tw

measure the local seismic amplification and water pressure variations. The analyses of soil liquefaction potential and seismic hazard of harbor facilities were therefore conducted and provided as reference for seismic design. To improve the abilities of seismic monitoring, earthquake early warnings, and locating earthquakes, the Central Weather Bureau (CWB) started to renew old seismometers and constructed a surface-downhole monitoring system throughout Taiwan. The upgrading of cables and the setting up of a framework to integrate all stations as new generation platforms for seismic monitoring was also carried out. The integrated monitoring system can therefore increase signal quality, resolution of the earthquake source, the ability to rapidly report an earthquake, and speeds up the focal mechanism calculation.

For the purpose of further understanding the properties of seismic wave propagation and site amplification in near surface layers, the National Center for Research on Earthquake Engineering (NCREE) of the National Applied Research Laboratories (NARL) installed a downhole seismic array near the edge of the Taipei Basin (inside NCREE) with five accelerometers at the surface and at depths of 20, 30, 58, and 78 m. This array is able to analyze the seismic site effect from the bedrock to different layers and the surface inside the important Taipei Basin. Another downhole array including a surface accelerometer and three downhole accelerometers at depths of 20, 30, and 70 m, was installed at the National Dong Hua University (NDHU), in order to observe and analyze the characteristics of near source seismic waves.

Logging Investigations and Station Installation

In order to increase the accuracy of analyses, a detailed knowledge of the geology and velocity loggings of the site are necessary prior to the installation of seismometers. Examples of the required data are the Standard Penetration Test (SPT), soil grain size analysis, soil classification by the United Soil Classification System (USCS), laboratory physical properties test for soils and velocity measurements every 0.5 m using a suspension PS-logging system. The profiles of N-value, P-wave, and S-wave velocities at the two stations are plotted in Fig. 1. The depth of the bedrock in NCREE is determined to be around 58 m from the profiles. The N profile is up to 50 at a depth of three meters at NDHU, where the layer is composed of sand and gravel. The S-wave velocity is higher than 300 m/s without obvious interface until a depth of 65 m. The measured average S-wave velocities in the top 30 m (Vs30) are 236.7 m/s (class D or Second type) and 479.0 m/s (class C or First type) at NCREE and NDHU, respectively.

The seismometers were then installed. The NCREE station firstly used a sampling rate of 100 Hz and then changed to 200 Hz. The NDHU station started the operation with the same sampling rate of 200 Hz. The in-situ environments are shown in Fig. 2.

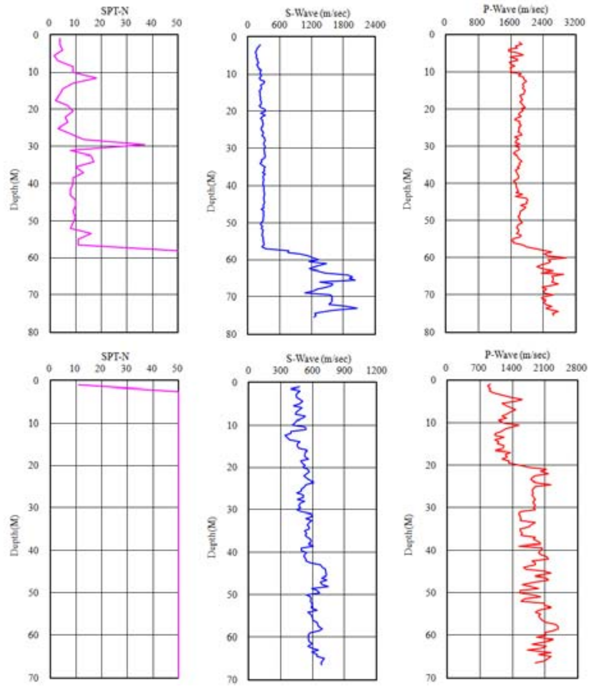

Fig. 1 Profiles of N-value (left), S-wave velocity (middle), and P-wave velocity (right) of the stations at NCREE (upper) and NDHU (lower)

Fig. 2 In-situ photos at the stations of NCREE (upper) and NDHU (lower)

Intensity of Ambient Noise and Seismic Observation

Recordings of downhole accelerometers are able to avoid contamination caused by high frequency noise from the surface in comparison with the accelerometers installed at the surface. The data quality of downhole accelerometers is, therefore better than that of surface ones, especially for small earthquakes. We used Power Spectral Density (PSD) to analyze the intensity of ambient noise of the data at the surface and the deepest subsurface for two stations. The results (Fig. 3 and Fig. 4) show that the ambient noise of frequency higher than 1 Hz is lower at the subsurface than at the surface, as expected.

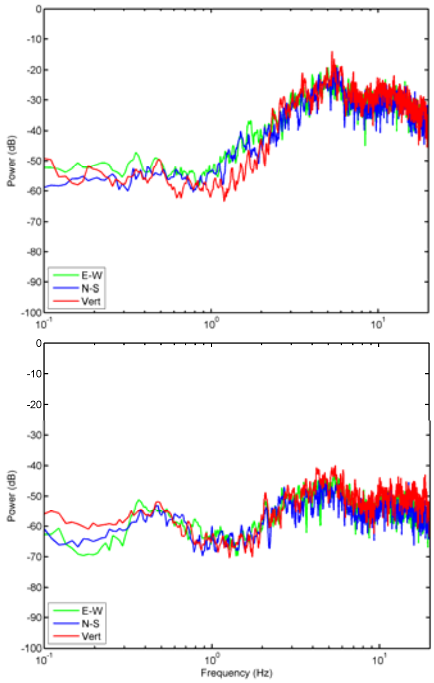

Fig. 3 PSD of ambient noise at surface (upper) and downhole (lower) at the NCREE station

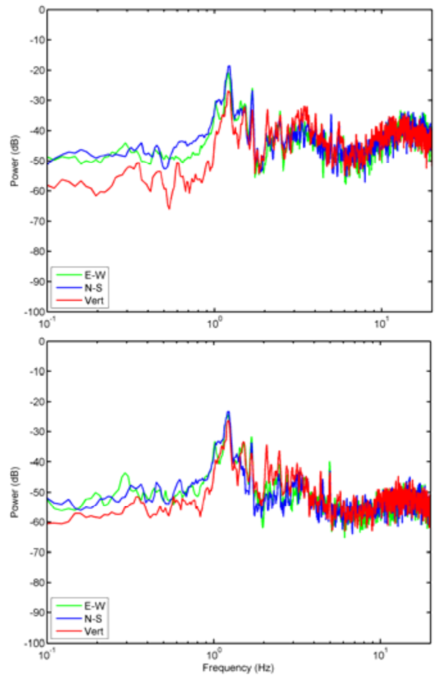

Fig. 4 PSD of ambient noise at surface (upper) and downhole (lower) at the NDHU station

The locations of the downhole array stations at NCREE and NDHU as well as the epicenters of recorded events in 2014 are shown in Fig. 5. Most of the recorded earthquakes occurred in eastern Taiwan with magnitudes of three and four. The recorders used in this study have a high resolution (24 bits) and the sensors were installed at the subsurface to avoid high frequency noise. This allows the arrays to record earthquakes with magnitudes of three to four within 100 km of the hypocenter and record earthquakes with magnitude of four to five within 200 km of the hypocentral (Fig. 6). The NDHU station is able to record some local small earthquakes with magnitude of only two to three because it is situated near the source area.

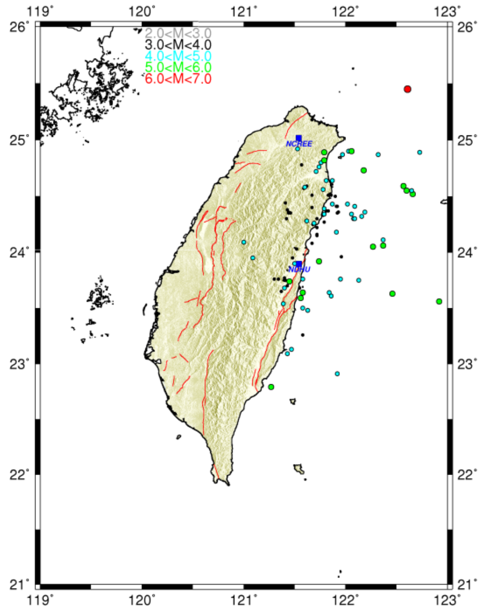

Fig. 5 Locations of the downhole array stations (blue square) and recorded epicenters (circles). The colors and sizes of the circles indicate different magnitudes

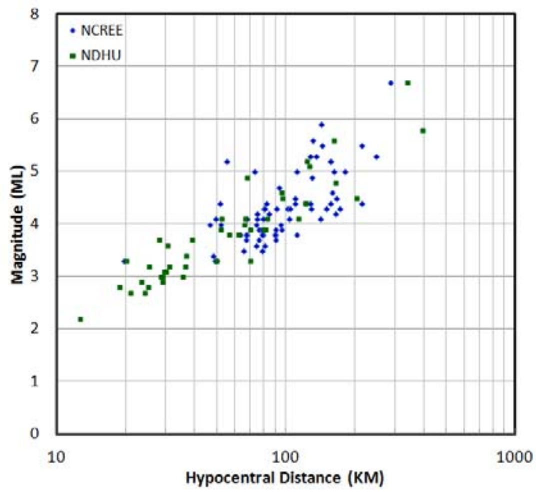

Fig. 6 Distributions of hypocentral distance and magnitude for the recorded earthquakes

The Characteristics of PGA

The downhole seismic arrays at NCREE and NDHU have five and four accelerometers at different depths, respectively. The change of seismic wave amplitudes can be measured clearly by observing their propagations in the near-surface layers using the downhole arrays. Therefore, the variations of Peak Ground Acceleration (PGA) can be analyzed using this data. However, the observation durations of the two stations until the end of 2014 are only eight and two months, respectively. Most of the recorded accelerations belong to an intensity of zero grade (PGA < 0.8 gal) and even the largest intensity is of only three grade (8 gal < PGA < 25 gal). Fig. 7 shows the statistics of the intensity distributions and implies that we still need time to wait for large events.

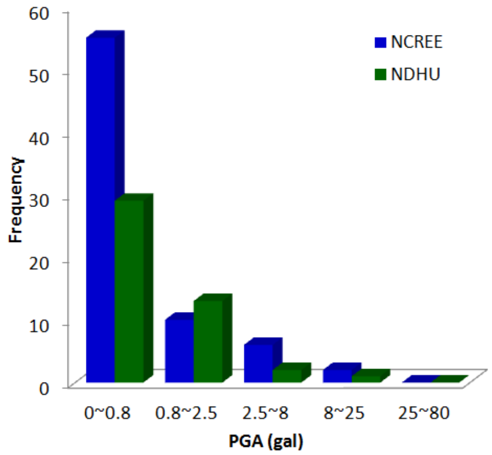

Fig. 7 Intensity distributions of recordings for the two stations

We normalized the PGA of the surface accelerometer to 1 and the PGA values at different depths were therefore less than 1. The normalized results can show the PGA variations of events on the same scale, helping to understand the local site effect caused by the near surface layers. Fig. 8 shows the average PGA variations with the depth of the NCREE station (black) and the NDHU station (blue). The x-axis is the normalized PGA and the y-axis is the depth (red squares indicate the depths of accelerometers). Results of PGA variations in the vertical component are plotted as dotted lines and those of the horizontal component (calculated as the vector summation of the NS and EW components) are plotted as solid lines. At the NCREE station, the PGAs of both horizontal and vertical components are amplified by around five times from the bedrock (depth of 78 m) to the surface. For the case of the NDHU station, the PGA is amplified by about 2.5 times in the horizontal component. Otherwise, the PGA of the vertical component is amplified by about 3.3 times. The amplification of PGA at NDHU is smaller than at NCREE because the deepest accelerometer is not in the bedrock and thus cannot represent the whole amplification of the sediments in Hualieh.

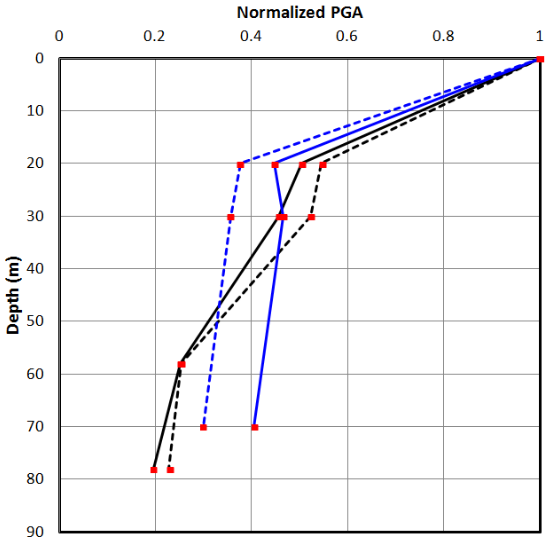

Fig. 8 Normalized amplification of PGA from the downhole to the surface for stations at NCREE (black) and NDHU (blue)

Conclusions

We have installed two seismic downhole arrays that include five and four accelerometers respectively, in the Taipei Basin (NCREE) and in Hualien (NDHU) to observe the seismic wave amplification in the near surface layers as well as the characteristics of near source seismic waves. Earlier investigations of the two sites were also conducted to understand the geological and seismic conditions and can therefore be a very important reference for the related studies. This study analyzed the PGA variation with depth for both the horizontal and vertical components. The recordings used are all weak motions so that it is still not necessary to consider soil nonlinearity in our analysis. The results show that PGA can be amplified by up to five times at NCREE and by about 2.5 times at NDHU; the difference arises because the deepest station is in the sediments of the latter. Observed recordings will be used to calculate transfer functions of layers and calculate S-wave velocities using different methods in subsequent studies.

References

Huang, W.G., Huang, B.S., Wang, J.H., Chen, K.C., Wen, K.L., Tsao, S., Hsieh, Y.C. and Chen C.H. (2010), "Seismic Observations in the Taipei Metropolitan Area Using the Downhole Network", *Terr. Atmos. Ocean Sci.*, 21(3), 615-625.

Wen, K.L., Fei, L.Y., Peng, H.Y., and Liu, C.C. (1995), "Site effect analysis from the records of the Wuku downhole array", *Terr. Atmos. Ocean Sci.*, 6(2), 285-298.

Geochemical Monitoring for Earthquake Precursory Research

Vivek Walia[1], Shih-Jung Lin [2], Arvind Kumar [3], Yu-Tzu Liao [4], Tsanyao Frank Yang [5] and Kuo-Liang Wen [6]

Abstract

The present investigations aim at developing an effective earthquake precursory system from the long term soil-gas data obtained from a network of soil-gas monitoring. In very recent years, we have established monitoring stations in the Tatun volcanic area (TVG) using Solid State Nuclear Track Detectors (SSNTDs) technique to investigate soil-gas radon-thoron variations to observe the tectonic activity in the Tatun volcanic area of northern Taiwan. As per the present practice, the data from various stations are examined synoptically to evaluate earthquake precursory signals against the backdrop of rainfall and other environmental factors. The present study is also aimed at the appraisal and filtrations of these environmental/meteorological parameters and to create a real-time database for earthquake precursory study. During the observation period of 2014, about 30 earthquakes of magnitude $\geq$ 5 were recorded and out of these, 10 earthquakes fell under the defined selection criteria and were tested in the proposed model. Out of these 10 earthquakes 7 have been forecasted or shown precursory signals.

Keywords: Soil-gas, Earthquake, Radon, SSNTDs, Real-time, Data base

Introduction

Soil gas geochemistry and its spatial/temporal variations has been used for monitoring of seismic activities, volcanic activity, environmental research, mapping of fault zones, geological traces etc. for decades (Fu et al., 2005; Kumar et al., 2009, 2013; Walia et al., 2013; Yang et al., 2006). There have been various researches dealing with the measurements of radon concentration in soil, gas emanating from the ground along active faults, which may provide useful signals before seismic events (Armienta et al., 2002; Chyi et al., 2011; Fu et al., 2008, 2009; Walia et al., 2009a; Yang et al. 2005, 2011). Studies on diffuse degassing from sub-surface carried out have clearly shown that the gases can escape towards the surface by diffusion and by advection and dispersion as they are transported by rising hot fluids and migrate along preferential pathways such as fractures and faults (Yang et al., 2003). The island of Taiwan is a product of the collision between Philippine Sea plate and Eurasian plate which make it a region of high seismicity. Active subduction zones occur south and east of Taiwan. To the south an oceanic part of the Eurasian plate is sub-ducting beneath the Philippine Sea plate along the Manila Trench, whereas in east the oceanic lithosphere of the Philippine Sea plate is subducting northwestward underneath the Eurasian plate along the Ryukyu Trench. These collisions are generally considered to be the main source of tectonic stress in the region. Among them, some have been identified active faults (Hsu 1989). A detailed study of these active faults will provide information about the activity of these faults and give basis, which may greatly help to reduce the damage when the unavoidable large earthquakes come. This study further helps the earthquake engineers to define the building codes for each fault zones.

In the last few years, we focused on the temporal variations of soil-gas composition at established geochemical observatories along the Hsincheng fault (HC) in Hsinchu area, Hsinhua fault (HH) in Tainan and at Jaosi (JS) in Ilan areas of Taiwan (Fig.1), respectively, to determine the influence of enhanced concentrations of soil gases to monitor the tectonic activity in the region and to test the previously proposed tectonic setting based model (Walia et al, 2009b,2012) from data generated at earthquake monitoring stations during the observation period. The stress-induced variations due to impending earthquakes in radon are contaminated by

[1] Research Fellow, National Center for Research on Earthquake Engineering, walia@ncree.narl.org.tw
[2] Professor,Department of Geosciences, National Taiwan University, tyyang@ntu.edu.tw
[3]Associate Research Fellow, National Center for Research on Earthquake Engineering, kumar@ncree.narl.org.tw
[4] Assistant Research Fellow, National Center for Research on Earthquake Engineering, sjlin@ncree.narl.org.tw
[5] Assistant Research Fellow, National Center for Research on Earthquake Engineering, 1406027@ncree.narl.org.tw
[6] Professor, National Center for Research on Earthquake Engineering, wenkl@ncree.narl.org.tw

meteorological changes (i.e. Atmospheric temperature, pressure, precipitation, etc.) and, hence assessment and quantification of these influences are a major prerequisite in the isolation of precursory signals. As per the present practice, the data from various stations are examined synoptically to evaluate earthquake precursory signals against the backdrop of rainfall and other environmental factors. The present study is aimed at the appraisal and filtrations of these environmental/ meteorological parameters and to create a real-time database for earthquake precursory study.

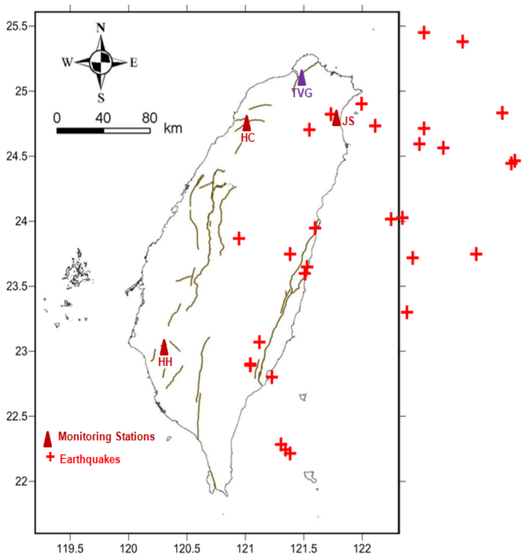

Fig.1.Map showing distribution of monitoring station and earthquakes recorded in the year 2014.

Variation of volcanic gas composition is considered as an important index of volcanic activity. Compositions of volcanic gases can help to understand the sources and origin of magmas in particular area. Radon (^{222}Rn) is the major radioactive gas in volcanic areas. The study of radon-thoron concentration variations in volcanic areas has been considered as a useful tool to investigate the volcanic activity. In addition to already established three monitoring stations in Hsinchu, Tainan and I-lan areas of Taiwan for earthquake forecasting studies, we tried to investigate geochemical variations of soil-gas radon-thoron concentrations using Soild State Nuclear Track Detectors (SSNTDs) technique (i.e. cellulose nitrate LR-115 films) to observe the tectonic activity in the Tatun volcanic area of northern Taiwan in very recent years.

Results and Discussions

To carry out the continues monitoring, investigation at the established monitoring stations, soil-gases compositions variations were measured regularly using RTM2100 (SARAD) for radon and thoron measurement following the procedure as described in Walia et al, 2009b. Seismic parameters (viz. Earthquake parameters, intensity at a monitoring station, etc.) and meteorological parameter data were obtained from Central Weather Bureau of Taiwan (www.cwb.gov.tw).

The Tatun volcano group (TVG) includes more than 20 volcanoes [Wang and Chen, 1990] and is located at the northern tip of Taiwan. TVG is about 15 km north of Taipei, the capital of Taiwan that has more than seven million inhabitants. Besides that two nuclear power plants that were built 30 years ago along the northern coast of Taiwan, are located only a few kilometers northeast of the TVG. Thus, the assessment for any potential volcanic activity in the Tatun area is not only a scientifically interesting topic, but will also have a great impact on the safety of the whole of the northern Taiwan area. The study of radon flux and concentration variations in volcanic areas has been considered as a useful tool to investigate the volcanic activity in one area.

In the ongoing Ministry of Science and Technology (MOST) project, experiments have been carried out to calibrate cellulose nitrate alpha detector films (LR-115) for the measurement of radon and thoron concentrations in soil gas for volcanic and seismic study. From this study it is concluded that progeny nuclides effect the track formation in LR-115 films in bare mode, which must be controlled in an experimental setup (Kumar et al., 2013). In order to study radon-thoron in volcanic areas, radon-thoron discriminators along with LR films were installed in Tatun Volcanic areas (Fig. 2) at number of sites (i.e. at Hsiaoyoukeng (SYK), Dayoukeng (DYK) and Gungtzeping (GTP), respectively) having different temperatures in a hole (about 50 cm depths) for a defined period (bi-weekly to monthly). Preliminary results show that the temperature of the sites are not constant in volcanic areas i.e. temperature during installation and during retrieval of the films from the hole is different. The safest temperature to install the films in volcanic areas is $\leq 65\ ^{0}$ C. The number of tracks recorded for thoron is very small. It means thoron concentration is very low in the study area. The low values of radon concentration at SYK Fig. 3a, b) and DYK (Fig. 4a, b) sites may be due to the existence of underneath magma chamber and dominated by the volatile gases whereas comparatively high values of radon at GTP (Fig. 5) may be due to the presence of fractured zones. Also, radon behavior observed is different at different sites in the volcanic areas of northern Taiwan and some sites are not suitable for radon detection (Kumar et al., 2013). Observations have also shown potential precursory signals for some earthquakes occurred during the observation period (January 2012-January 2013) having epicenter in and around TVG (Fig.6). In order to study the radon flux and concentration variations in volcanic areas continuous/integrated monitoring of sub soil radon is absolutely necessary for better results.

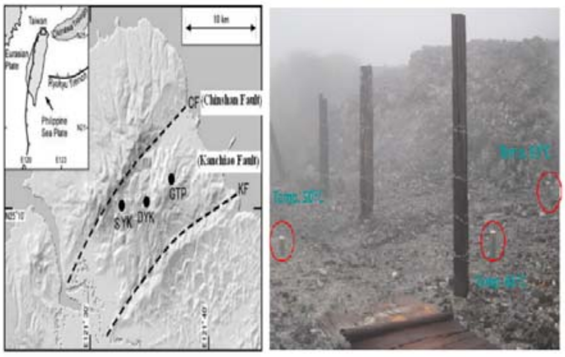

Fig. 2: Locations of TVG monitoring stations and discriminators installed in one of the monitoring stations.

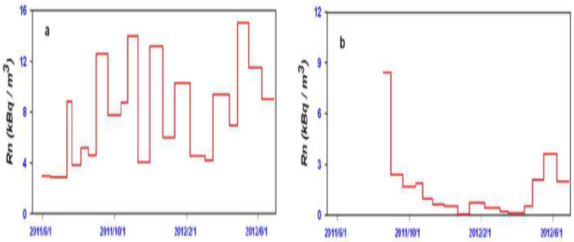

Fig. 3: Recorded average radon concentration at SYK **(a)** temperature range 24°C to 29°C and **(b)** temperature range 48°C to 60°C.

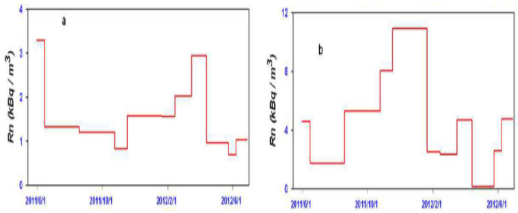

Fig. 4: Recorded average radon concentration at DYK **(a)** temperature range 23°C to 46°C and **(b)** temperature range 60°C to 65°C.

Also in the ongoing MOST Project, radon-helium survey were undertaken in and around Shanchiao fault for the selection of suitable sites for integrated radon monitoring using SSNTDs to see the tectonic activity of the fault systems. Keeping the work carried out above in mind and the low cost of SSNTD technique, we will establish number of long term monitoring sites: 1) along single fault to know the activity of the fault/s under observation which is not possible in other techniques, 2. In/around the Tatun volcanic area located in northern Taiwan, where hydrothermal activity is still active to study the radon flux and concentration variations in volcanic areas.

As per the present practice, the data from various stations are examined synoptically to evaluate earthquake precursory signals against the backdrop of rainfall and other environmental factors (see the previous reports). Various guidelines are developed to identify the nature of precursory signals almost in real-time. A real-time base has been developed,

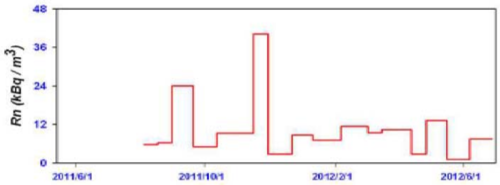

Fig 5: Recorded average radon concentration at GTP, where the temperature range is 35°C to 60°C.

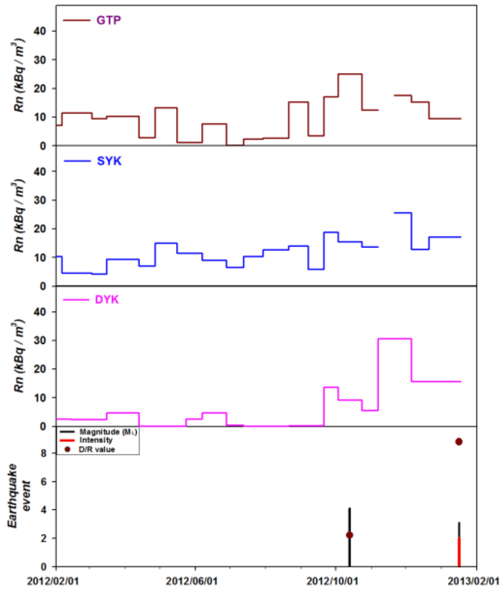

Fig.6:. Variations of radon at GTP, SYK & DYK monitoring stations and their correlation with earthquakes.

modified and used. In recent years automated operating real-time base had been developed and efforts were made to improve it. For the earthquake prediction the efficiency of an operation system depends not only upon its logical correctness, but also upon the response time. So, it's very important to work on reducing the "response time" effectively, which it has been achieved by using with some information technology techniques in automated real time database. Data from various monitoring stations (run by NCREE and NTU in collaboration) are automatically uploaded to the web service which provides the data management/exhibition with less response time database. In addition to monitoring station data, seismic parameters (i.e. Magnitude/location/depth of the event, the intensity/epicentral distance at a monitoring station, etc.) and meteorological parameter data are also uploaded from Central Weather Bureau of Taiwan (www.cwb.gov.tw) simultaneously. It would be helpful in increasing efficiency of earthquake prediction studies.

During the observation period of 2014, about 30 earthquakes of magnitude ≥ 5 were recorded in and around Taiwan. However, out of these, 10 (i.e. about 33%) earthquakes fell under the defined selection criteria and were tested for the proposed model. Out of these 10 earthquakes 7 (i.e. 70% of fitted earthquakes) have shown precursory signals (Fig.7).

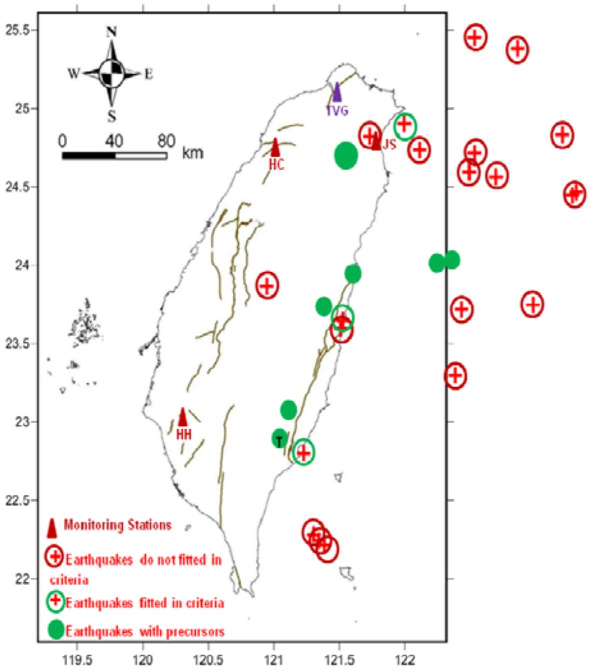

No. of Earthquakes of M≥5 (Jan. to Dec. 2014) (a) = **30**
Earthquakes fitted in defined criteria (i.e Depth ≤40 kms, Intensity ≥1 (at monitoring station) (b)= **10**
Fitted rate (b/a) = **33%** Forecasted (c) = **7**
Success rate with earthquakes fitted in criteria (c/b) = **70%**
Total success rate with all earthquakes of M≥5 (c/a)= **23%**

Fig.7:Distribution of recorded and correlated earthquakes in year 2014. Statiscial analysis of recorded and correlated earthquakes.

References

Armienta, M.A., Varley, N. , Ramos E.(2002). Radon and hydrogeochemical monitoring at Popocatépetl volcano, Mexico. Geofí. Intern. 41, 271-276.

Chyi, L.L., Quick, T.J., Yang, T.F., Chen, C-H. (2011). The origin and detection of spike-like anomalies in soil gas radon time series. Geochem. J., 45, 431-438.

Dobrovolsky, I.P., Zubkov, S.I. and Miachkin, V.I. (1979). "Estimation of the size of earthquake preparation zones". *Pure and Appl. Geophys*., 117, 1025-1044.

Etiope G., Calcara, M., Quattrocchi, F. (1997). "Seismogeochemical algorithms for earthquake prediction: an overview". *Annali Di Geofisica*, 40(6), 1483-1492.

Fu, C.-C., Yang, T.F., Du, J., Walia, V., Chen, Y.-G., Liu, T.-K., Chen, C.-H. (2008). Variations of helium and radon concentrations in soil gases from an active fault zone in southern Taiwan. Radiat. Meas. 43, S348–S352.

Fu, C.C., Yang, T.F., Walia, V., Chen, C.H. (2005). "Reconnaissance of soil gas composition over the buried fault and fracture zone in southern Taiwan". *Geochemical Journal*, 39,427-439.

Fu, C.C., Yang, T.F., Walia, V., Chen, C.-H. 2005. Reconnaissance of soil gas composition over the buried fault and fracture zone in southern Taiwan. Geochemical J. 39, 427-439.

Fu, C.-C., Yang, T.F., Walia, V., Liu, T.-K., Lin, S.-J., Chen, C-H., Hou, C.-S. (2009). Variations of soil-gas composition around the active Chihshang Fault in a plate suture zone, eastern Taiwan. Radiat. Meas. 44, 940-944.

Hsu, T. L. (1989). Geology and Engineering. 8th Ed., Ker-Chi -Book Company, Taipei (in Chinese)

Kumar, A., Singh, S., Mahajan, S., Bajwa, B.S., Kalia, R., Dhar, S. (2009). "Earthquake precursory studies in Kangra valley of North West Himalayas, India, with special emphasis on radon emission". Appl. Radiat. Isot. 67, 1904-1911.

Kumar, A., Walia, V., Yang, T.F., Hsien, C-H., Lin, S.J., Eappen, K.P., Arora, B.R. (2013). Radon-thoron monitoring in Tatun volcanic areas of northern Taiwan using LR-115 alpha track detector technique: Pre Calibration and Installation. Acta Geophysica, 61 (4), 958-976.

Walia V, Yang TF, Lin S-J, Kumar A, Fu CC, Chiu J-M, Chang H-H, Wen K-L, Chen C-H (2013) Temporal variation of soil gas compositions for earthquake surveillance in Taiwan. Radiat Meas 50:154–159.

Walia, V., Lin, S-J.,Yang, T.F., Fu, C-C., Hong, W-L., Wen, K-L.,Chen, C-H. (2010). "Soil-gas monitoring: A tool for fault delineation studies along Hsinhua Fault (Tainan) Southern Taiwan." *Applied Geochemistry, 25,* 602-607.

Walia, V., Virk, H.S., Yang, T. F., Mahajan, S., Walia, M. and Bajwa, B.S. (2005). "Earthquake prediction studies using radon as a precursor in N.W Himalayas, India: a case study". *TAO*, 16(4), 775.804.

Walia, V., Yang, T.F., Lin, S.J., Hong, W.L., Fu, C.C., Wen, K.L.,Chen, C.H. (2009b). "Continuous temporal soil.gas composition variations for earthquake precursory studies along Hsincheng and Hsinhua faults in Taiwan". *Radiat. Meas.,* 44, 934.939.

Walia, V., Yang, T.F., Lin, S.J., Hong, WL., Fu, C.C., Wen, K-L.,Chen, C-H. (2009a). "Geochemical variation of soil-gas composition for fault and earthquake precursory studies along Hsincheng fault in NW Taiwan". *Appl. Radiat. Isotopes, 67, 1855- 1863.*

Yang, T.F., Wen, H.-Y., Fu, C.-C., Lee, H.-F., Lan, T.F., Chen, A.-T., Hong, W.-L., Lin, S.-J., Walia, V., (2011). "Soil radon flux and concentrations in hydrothermal area of the Tatun Volcano Group, Northern Taiwan". *Geochem. J*., 45, 483-490.

Monitoring of Crustal Activities in the Yun-Chia-Nan area of Taiwan

Yi-Zeng Chang [1] and Strong Wen [2] and Chau-Huei Chen [3] and Kou-Liang Wen [4]

張議仁 [1]、溫士忠 [2]、陳朝輝 [3]、溫國樑 [4]

Abstract

The physical properties of the crust exhibit variation due to the effect of tectonic stress. In particular, before and after strong earthquakes, the relevant physical parameters (velocity, attenuation) produce a change that has been discussed in numerous studies. After a strong earthquake, the rupture can cause rock fragmentation and lead to pore fluid migration or filling and this phenomenon can be observed by analyzing the seismic wave propagation. Therefore, this study uses small earthquakes to calculate seismic crustal attenuation parameters. The variation in physical parameters can confirm the correlation between the observed data and the occurrence of earthquakes, and assess changes in the regional stress state. When a seismic wave propagates, the geometric spreading and anelastic absorption affect the amplitude, and related factors that include the rock porosity, lithology, temperature and pressure conditions, rock particle size, viscosity, and saturation. Hence, this study proposes monitoring of the crust, which exhibits temporal variations in lithology and fluid conditions under tectonic stress before an earthquake. Through the use of high-quality seismic waveform data and dispersive attenuation analysis, we can resolve temporal changes in media and assess the regional seismogenic processes.

Keywords: Dispersive attenuation, Qp

1. Introduction

At present, studies of crustal structures not only explore the variations in space, but also consider changes over a time period. Most research indicates that crustal disturbances are generated by earthquakes. Chen *et al.* (2011) carried out waveform comparisons using repeating earthquake sequences and a cross-correlation coefficient that showed changes in seismic waveforms from an earthquake. Kelly (2013), who used the repeating cluster and spectral ratio method to calculate Δt^* (the whole path attenuation operator), found a decrease in the Q factor after earthquakes. Wang and Ma (2014) adopted a single-path method to estimate the Qs value (the S-wave quality factor) and the temporal distribution around crustal earthquakes and showed that the average Q values increased before the 921 Chi-Chi earthquake. On the other hand, the velocity change after an earthquake can also be observed from the tomography inversion, but the change in velocity for regional media often exhibits a linear trend, and the attenuation factor is more sensitive than that. Changes in the crustal physical parameters are affected by lithology, temperature, pressure, cracking, pore fluid decrease, shift changes, etc., and the major factor in these cases is the effect of the tectonic stress generated from the collision process. Therefore, continuous observations play an important role in exploring the correlation between the seismic attenuation parameters and temporal variations. In addition, these results can also be considered an indicator of whether there is an implicit change in regional stress status.

2. Methodology

Dispersion concerns the velocity variation with a frequency change. Ciz *et al.* (2006) indicated that a P-wave shows an obvious dispersion effect in the frequency band of 10^0–10^4 Hz. In other words, the dispersive P-wave can be used to detect the physical change of media. The quality factor, Q, is a

[1] Assistant Researcher, National Center for Research on Earthquake Engineering, yzchang@ncree.narl.org.tw

[2] Associate Researcher, National Center for Research on Earthquake Engineering, scwen@ncree.narl.org.tw

[3] Professor, Dept. of Earth and Environment Sciences, National Chung Cheng Univ., seichen@eq.ccu.edu.tw

[4] Professor, Dept. of Earth Science, National Central Univ.,wenkl@ncree.narl.org.tw

dimensionless parameter and a small loss in seismic energy can be referred to as a high Q value. Dispersive attenuation exhibits more advantages than amplitude attenuation (Cong *et al.*, 2000) for the following reasons: (1) dispersive attenuation uses the first cycle of P-wave, while the amplitude attenuation method is easily affected by focusing and defocusing; (2) dispersive attenuation can be calculated from only a single station and the corner frequency is high enough in the frequency range of interest for small earthquakes; (3) through continuous monitoring of a small earthquake, the data is sufficient for calculations and the resolution in temporal variation; (4) the records from smaller earthquakes can avoid complex rupture behavior; and (5) the use of P-wave first motion data can effectively avoid interference from other waves.

3. Data processing

Figure 1 illustrates the study area with the station distribution denoted by blue triangles, the locations of large seismic events (M > 3.5) denoted by red stars, and the fault traces shown by red lines. This study used the data from the Central Weather Bureau Seismic Network (CWBSN) to seek the attenuation parameters. We chose the vertical component data from 2014 with magnitudes lower than 3 for each station. In addition, data also accessed selected epicenters ≤30 km away and focal depths ≤30 km away. Thus, by the use of smaller event data, the angular frequency can indeed fall into the frequency range. In addition, a relatively large number of smaller events can help us to study the environment surrounding the measuring station and it also increases the resolution in temporal variation.

This study used the 2014 waveform data from the CHN5 and ALS stations, which cover 332 and 478 events, respectively. The first cycle of P waves was cut for analysis. Figure 2(a) shows the waveform of the first cycle of P-wave data and then resamples the waveform to 1000 points using the Newton interpolation method and a band-pass filter.

The first cycle of a P-wave is sufficient to obtain information about the medium and it is unlikely to be disturbed by other phase signals. Due to fact that the signals are affected by the earthquake location and time of occurrence, the statistics for earthquake-related information are shown in Figure 3, in which the magnitudes of most seismic events are between 1.0–1.5 (M_L) and the focal depths are shallower than 15 km. Deeper seismic events (depth > 15 km) are fewer in number and have poor resolution. Regional stress accumulation within a limited range (epicentral distance less than 20 km) before a strong earthquake, as well as a longer wave propagation path, causes weak seismic waves with abnormal characteristics that also exhibit a high noise ratio, thus this poor quality data cannot be used in this study. Therefore, the available data become less when the epicentral distance is larger than 30 km.

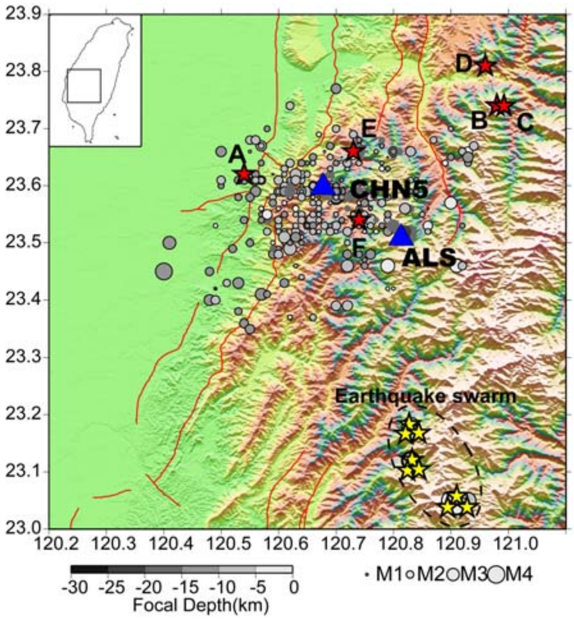

Figure 1. The selected events near CHN5 and ALS in 2014. The blue triangles indicate the stations, the red stars indicate large earthquakes, and yellow stars denote the swarm.

We adopts multiple filters technique to obtain group velocity of first cycle of P-wave. In Figure 2(b), the horizontal axis represents the frequency, and the ordinate represents the group velocity delay time, and the red circles denote the size of the energy corresponding to different frequencies. If waveform data is disturbed, then the time–frequency spectrum is considered to exhibit chaos and the data would not be used. Finally, we use the genetic algorithms to search optimal solutions (shown in red lines): Q_m, τ_1, and τ_2 in Figure 2(b).

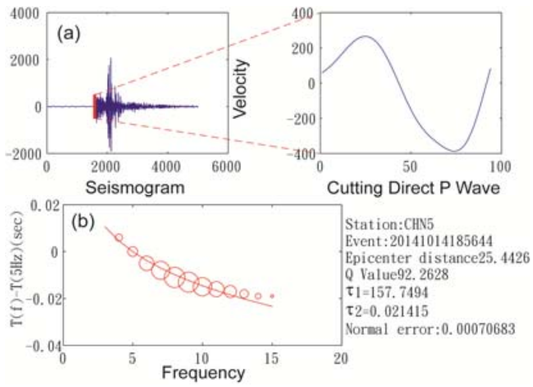

Figure 2. Data processing.

The above parameters are constant over a particular frequency range (Liu *et al.*, 1976). Here, we use Qp, rather than Q_m to indicate the results in this study. Due to the increased Qp with longer epicentral distance, we calculated the averaged Qp residuals (dQ) by taking the mean value of the Qp residuals at a specified depth range in a half-month moving window, which shifted at a time step of one day and then used a regression process for base-line correction to obtain the residuals. Finally, each seismic Q value statistic obtained by a respective station was converted into a distribution diagram corresponding to the time, and the appropriate average was taken to show the nearby area of the temporal variation.

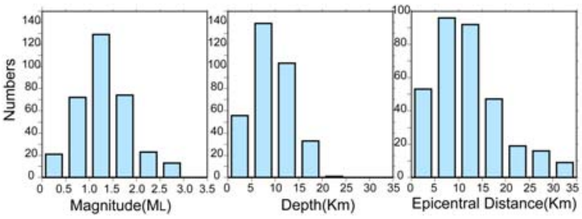

Figure 3. The variation of dQ at CHN5 in 2012. It is divided into two sides (east and west) to identify the anomalies.

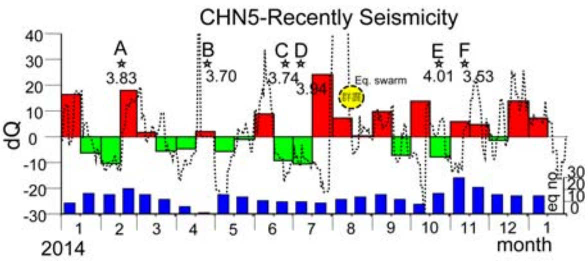

Figure 4. The variation of dQ at CHN5 in 2014.

4. Results and discussion

Figure 4 shows the distribution of dQ for a whole year (2014) at the CHN5 station, and the vertical axis represents dQ. The red and green histograms show variations that are higher and lower than the average calculated over two weeks. The blue histogram shows statistics within two weeks of the earthquake; the dotted line represents the 15-days moving average; A–F are seismic events that were nearby CHN5 station (within 40 km of the epicenter and ML > 3.5) throughout the year 2014. The yellow blocks (relative to the positions shown as yellow asterisks) indicate swarm earthquakes, which had more than 20 seismic events with ML > 3.0 and occurred in a small area in August.

In order to understand the P-wave attenuation of dispersion prior to an earthquake, we further used station CHN5 as a center-point to divide the study area into two sides, east and west, as shown in Figure 5. An important feature of dQ is that it would increase at some particular time and then decrease under the tectonic stress. The dQ value often exhibits a high value around one month before the occurrence of an earthquake (Figure 5, seismic events A–F). The results show that dQ also showed anomalies before the earthquake swarm (the dotted circles in Figure 1 and 5). In order to study the effect of the earthquake swarm, we compared the results from the southern part of the ALS station in Figure 6; a higher dQ value occurred in July at both stations and ALS station showed an earlier anomaly than CHN5. The seismic swarm was 43 km away from the ALS station and had more than 20 events in which the magnitudes were larger than 3. Otherwise, the dQ in the western part of CHN5 was almost negative, and that of the eastern side had a positive value. As shown in the topography map in Figure 1, the western side of CHN5 consists of relatively soft alluvium that could allow the seismic energy to attenuate more and exhibit a smaller Q value; the eastern side of CHN5 belongs to the central range area, and here the Q value is relatively high. This difference reveals that dQ is sensitive to the regional geological structure.

With regard to the relationship between the magnitude of the earthquake and the increased scale of dQ, due to the influence of the number and location of earthquakes on the average dQ calculation, it will yield a high dQ phenomenon before the earthquake, but that of the whole area around the station is not increased. Although dQ considers regional variation, the locations of earthquakes and the selected events will affect the mean dQ. When more seismic events were used, a more reliable dQ calculation was obtained. Theoretically, for the same epicentral distance, a larger earthquake could cause dQ to exhibit a larger anomaly. However, we find that the magnitude of an earthquake as well as the epicentral distance are the most significant factors that affect the estimation of dQ.

For the above reasons, it is difficult to estimate the magnitude from the dQ value. However, it is understood that when an earthquake is large enough, the affected area will be greater and more stations can be evaluated. When within a shorter time, if more stations are used, the dQ phenomenon can be evaluated for larger areas to assess its relationship to the size of the earthquake. By using different stations, we can compare the information from different directions, and then the results not only assess the relationship between the scope and impact of the earthquake, but also can confirm this criterion. In Figure 6, two different orientations of the stations were compared to determine the mechanism of enhancing the pre-earthquake characteristics, but only two stations were used, which was not sufficient to show the affected area before a strong earthquake.

The available number of seismic events is also important, because if more seismic data is used, then dQ values from multiple paths can be obtained. These can resolve the information from different directions and, in particular, the depth, in the temporal variations. When there is a lack of resolution of timing, information from the media is missed. For the current evaluation method for the quality factor that adopts the dispersive attenuation to analyze small earthquakes, more data must be available to have better time resolution. The time period is two weeks for the dQ calculation and it may take a longer time for the Q value to describe the changes over a longer period within the crust.

5. Conclusions

Real-time data is currently available to analyze seismic anomalies through dispersive attenuation, and it can be shown via a statistical method that the dQ will increase before an earthquake. When comparing different stations, the same phenomenon of an increased Q value can be found in a shorter time, which indicated that this is not a single station phenomenon, and the analysis of more stations can enhance the judging mechanisms. The use of temporal variations in the attenuation factor can serve as a reference of changes in stress and seismicity.

References

1. Ben-Menahem, A., and Singh, S. J., Seismic Waves and Sources, Springer-Verlag, New York, 1108 pp. (1981).
2. Chen, K. H., Furumura, T., Rubinstein, J., and Rau, R. J. (2011), Observations of changes in waveform character induced by the 1999 Mw 7.6 Chi-Chi earthquake. *Geophys. Res. Lett.,* **38,** L23302, doi: 10.1029/2011GL049841.
3. Ciz, R., Gurevich, B., and Markov, M. (2006), Seismic attenuation due to wave-induced flow in a porous rock with spherical heterogeneities. *Geophysical Journal International*, **165**, 957–968.
4. Correig, A. M., and Mitchell, B. J. (1989), Attenuative body wave dispersion at La Cerdanya, eastern Pyrenees, *Phys. Earth Planet. Int.* **57,** 304- 310.
5. Correig, A. M. (1991), On the measurement of body wave dispersion, *J. Geophys. Res.* **96,** 16,525–16,528.
6. Cong, L., Mejia, J. and Mitchell, B. J. (2000), Attenuation dispersion of P waves in near the New Madrid seismic zone, *Bull. Seism. Soc. Am.* **90** (3) ,679-689.
7. Liu, H. P., Anderson, D. L., and Kanamori, H. (1976), Velocity dispersion due to anelasticity: implications for seismology and mantle composition, *Geophys. J. R. Astron. Soc.* **47,** 41–58.
8. Kelly, C. M., Rietbrock, A., Faulkner, D. R., and Nadeau, R. M. (2013), Temporal changes in attenuation associated with the 2004 M6.0 Parkfield earthquake, *J. Geophys. Res. Solid Earth*, **118,** 630–645, doi:10.1002/jgrb.50088.
9. Wang, Y. J., and Ma K. F. (2014), Investigation of the temporal change in attenuation within the ruptured fault zone of the 1999 Mw7.3 Chi-Chi, Taiwan earthquake. Pure Appl. Geophys. doi: 10.1007/s00024-014-0854-3

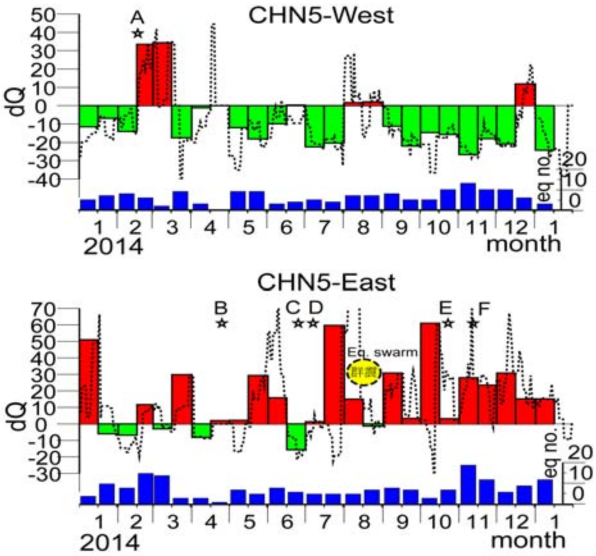

Figure 5. CHN5 is divided into two sides (east and west) to identify the anomalies.

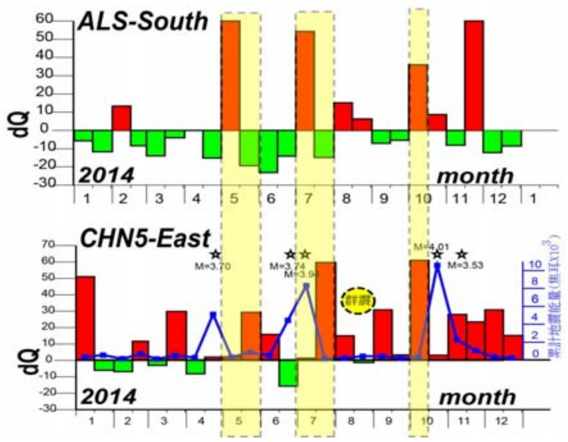

Figure 6. The histograms of the eastern part of CHN5 and southern part of ALS.

Ultimate Story Shear by Direct Moment Equilibrium

Lap Loi Chung [1] Yang Chih Fan [2] and Cho Yen Yang [3]

鍾立來 [1]、范揚志 [2]、楊卓諺 [3]

Abstract

The verification of ultimate story shear is asked by building code to ensure the shear strength is sufficient and no significant variation of stiffness for each story. However, there is no exact definition about calculation of ultimate story shear from the current building code. In this paper, a new method named direct moment equilibrium method is proposed. The ultimate shear is determined by directly taking moment equilibrium for each column. The ultimate story shear is obtained by taking summation of ultimate shear from each column. The proposed direct moment equilibrium method is also compared with two other methods which are familiar in practical application. Finally, the complexity of calculation and feasibility of the direct moment equilibrium method are verified.

Keywords: ultimate base shear, seismic design, plastic moment

Introduction

In recent years, earthquakes in Taiwan such as the Chi-Chi earthquake caused the collapse and destruction of many buildings. These phenomena repeatedly reveal the importance of structure seismic capacity. Because of the rapid development of the cities in Taiwan, it leads to the rapid increase in the number of high-rise buildings. And the high-rise buildings often use the high-ceilinged first floor, causing the buildings to form a weak layer.

The Building Code in Taiwan reviews the relevant provisions of the building ultimate base shear but not describes clearly how to calculate the ultimate shear strength. Many predecessors proposed method of calculating the ultimate base shear in the history of literature. This paper tried to obtain the ultimate base shear by direct moment equilibrium method and compare the results with the others two conventional methods.

This paper proposed a direct moment equilibrium method, and then used the examples in the book which named the Application with Concrete Engineering Design Specification to take the case analysis and compare with the other two methods, stiffness distribution method and elastic-plastic ratio method.

Stiffness Distribution Method

The principle of stiffness distribution method is to distribute the plastic moments of the beams at a joint to the ends of the columns according to the stiffnesses of the columns above and below the joint. In this study, we analyze the base shear of modern buildings, hence we assume the joints are in line with strong columns and weak beams. First, take a column on the first floor and a direction for analysis. Due to the assumption of strong columns and weak beams, we compute the plastic moments of beams M_{bpL} and M_{bpR} at the second-floor joint as shown in Fig. (1)a. Then calculate the stiffness parameters of the columns of the first and second layers E, I, H to get the column stiffness EI/H as shown in Fig. (1b). The summation of plastic moments $M_{\mathrm{bpL}}+M_{\mathrm{bpR}}$ is distributed to the top of first-floor column by the stiffnesses of the first- and second-floor columns:

$$M_{\mathrm{ct}} = \left(M_{\mathrm{bpL}} + M_{\mathrm{bpR}}\right) \frac{\frac{E_1 I_1}{H_1}}{\frac{E_1 I_1}{H_1} + \frac{E_2 I_2}{H_2}} \qquad (1)$$

where the subscripts c and t in moment M_{ct} indicate

[1] National Center for Research on Earthquake Engineering and Department of Civil Engineering, National Taiwan University, 0306005@ncree.narl.org.tw
[2] Department of Civil Engineering, National Taiwan University, r02521235@ntu.edu.tw
[3] KJ United Engineering Consultants INC, d9405004@mail.ntust.edu.tw

column and top. And the subscripts b, p, L and R in M_{bpL} and M_{bpR} indicate beam, plastic, left and right. Also, the subscripts 1 and 2 in E, I and H indicate the first and second floors. In addition, assuming the first floor is rigid, so plastic moment M_{cp} can be developed at the bottom of the first-floor column.

With the moments at the top and bottom of the first-story column and the clear height H_1 of the first story, the ultimate shear of the column line j is computed as:

$$V_j = \frac{M_{cp} + M_{ct}}{H_1} \tag{2}$$

The above steps are repeated and the ultimate base shears of all column lines in the same direction are calculated. Finally, the ultimate base shear V_{bs} is

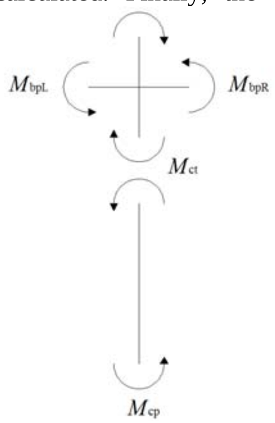

Fig (1)a: Free body diagram of joint in first and second floors

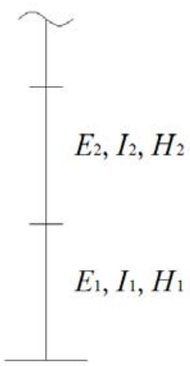

Fig (1)b: The stiffness parameters in first and second floors

obtained by summing up the ultimate shear of each column V_j.

$$V_{bs} = \sum_j V_j \tag{3}$$

Elastic-plastic Ratio Method

The principles of this method are to calculate the elastic and plastic moment of the beam ends, and the amplification factor between them. With this amplification factor, we can calculate the maximum moments of the column ends by magnifying the elastic moments by the factor. Since this paper aims to explore the ultimate base shear, only moments of the first floor are listed in Table 1.

First, calculate the plastic moments M_{bpL} and M_{bpR} of the beam ends of the joints. Then conduct elastic analysis by using ETABS. Given a horizontal seismic force, the elastic moments of the columns and beams ends of the structure are obtained as shown in Fig. (2)a. The subscript e of M_{beL} and M_{beR} shown in the Fig. (2)a indicates earthquake. Thus, we can calculate the amplification factor of the second floor by the elastic and plastic moments M_{bpL}, M_{bpR}, M_{beL} and M_{beR}:

$$\delta = \frac{M_{bpL} + M_{bpR}}{M_{beL} + M_{beR}} \tag{4}$$

Then calculate the plastic moments on the top of the column of the first story by multiplying the elastic moments M_{cet} by the amplification factor δ. In addition, assuming the first floor is rigid, the plastic moment M_{cp} can be developed at the bottom of the first-floor column. With the moments at the top and bottom of the first-story column and the clear height H_1 of the first story, the ultimate shear of the column line j is computed as:

$$V_j = \frac{\delta M_{cet} + M_{cp}}{H_1} \tag{5}$$

The above steps are repeated and the ultimate base shears of all column lines in the same direction are calculated. Finally, the ultimate base shear V_{bs} is

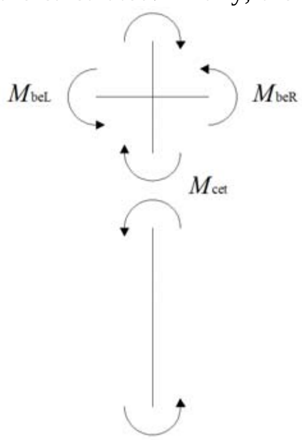

Fig. (2)a: Free body diagram in first-floor and second-floor joint

obtained by summing up the ultimate shear of each column V_j as shown in eq.(3).

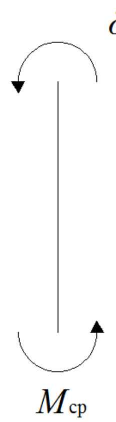

Fig. (2)b: Free body diagram in first floor

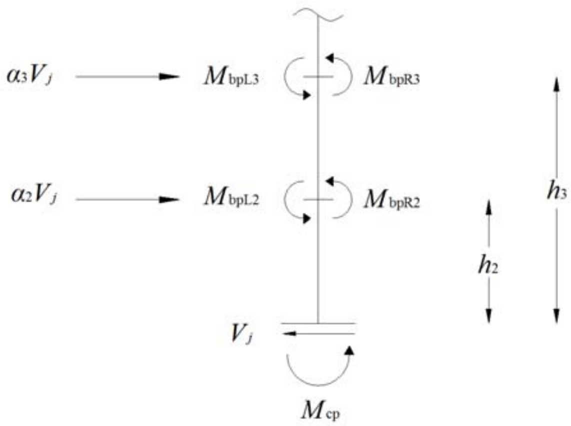

Fig. (3): Free body diagram in Direct Moment Equilibrium Method

Direct Moment Equilibrium Method

The principles of this method are to assume the base shear of the structure is V_{bs} which is distributed to each floor according to the formula for vertical distribution of seismic force:

$$\alpha_x = \frac{W_x h_x}{\sum_{i=2F}^{n+1} W_i h_i} \qquad x = 2F, 3F, ..., n+1 \qquad (6)$$

where the W_x and h_x indicate the weight and elevation of the x-th story. And the subscript n indicates the total number of floors.

In addition, each beam-column joints of each column lines have a moment $M_{\mathrm{p,min},x}$ as shown in Fig. (3). The plastic moment of beam-column joints is defined as the minimum of the summations of the plastic moments of beams and columns:

$$M_{\mathrm{p,min},x} = \min(\sum M_{\mathrm{bp},x}, \sum M_{\mathrm{cp},x}) \qquad (7)$$

Assuming the first floor is rigid, plastic moment M_{cp} can be developed at the bottom of the first-floor column.

As shown in Fig. (3), we take the moment about the base of the column line:

$$\begin{aligned}&\alpha_2 V_j h_2 + \alpha_3 V_j h_3 + \cdots \alpha_{n+1} V_j h_{n+1}\\ &= M_{\mathrm{p,min},2} + M_{\mathrm{p,min},3} + \cdots M_{\mathrm{p,min},n+1} + M_{\mathrm{cp}}\end{aligned} \qquad (8)$$

Furthermore, eq.(8) can be simplified to

$$\sum_{x=2}^{\mathrm{n+1}} \alpha_x V_j h_x = \sum_{x=2}^{\mathrm{n+1}} M_{\mathrm{p,min},x} + M_{\mathrm{cp}} \qquad (9)$$

Equation (9) is called the general moment equilibrium equation of a column line in direct moment equilibrium method. We can obtain the ultimate shear V_j of all column lines in the same direction by solving the eq. (9) repeatedly. Finally, the ultimate base shear V_{bs} is obtained by summing up the ultimate shear of each column V_j as shown in eq.(3).

Case Analysis

The site of the case is located in a new development region on the outskirts of Taichung City in Taiwan. The length and width of the base are 60 m. The area of the base is 3,600 m^2. There are 2 stories under the ground, 10 above the ground and 2 protrusions (penthouses) above the roof. The buildings plan and elevation are shown in the Figs. (4) and (5). The results in Table 1 show that the total base shears by the three methods in Y direction are similar. And the base shears of exterior columns by the direct moment equilibrium method are smaller than those by the others two methods. But the base shears of interior columns by the direct moment equilibrium method are bigger than those by the other two methods. These phenomenon is due to the eq. (9) where the base shear V_{bs} depends primarily on the plastic moments of the beams in the right hand side of the equation.

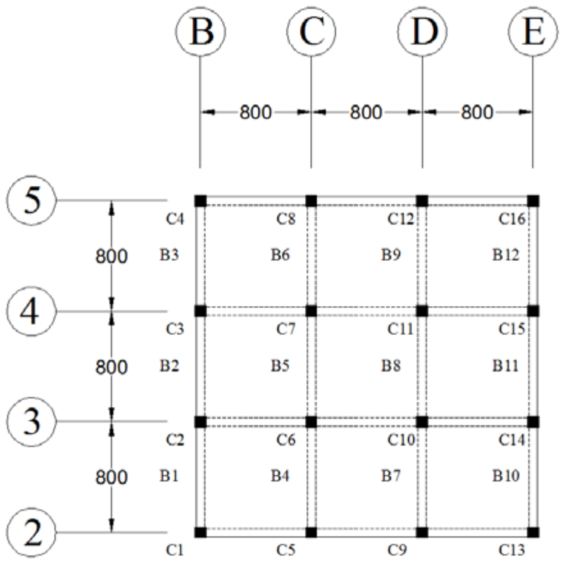

Fig. (4): Building plan in second floor

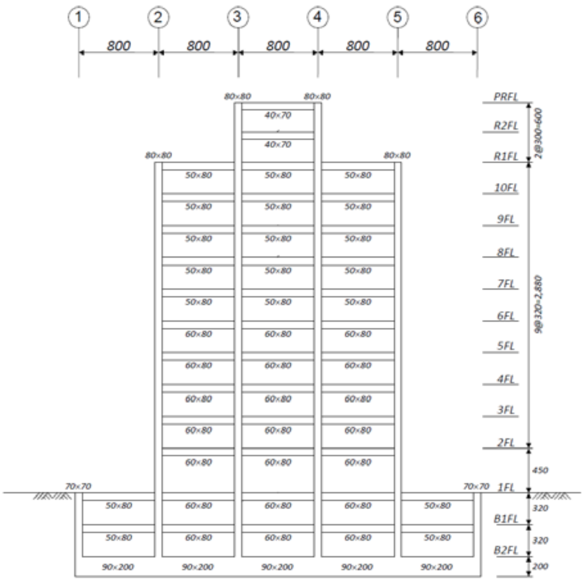

Fig.(5): Building elevation in Y direction

Table 1. Calculation results in three methods

Column Number	Stiffness Distribution Method	Elastic-Plastic Ratio Method	Direct Moment Equilibrium Method
C1	54.23	52.64	33.91
C2	75.95	71.62	74.44
C3	75.97	71.64	75.91
C4	61.18	58.20	51.33
C5	58.32	56.99	35.14
C6	71.75	62.44	81.84
C7	71.74	62.43	82.40
C8	63.51	61.31	47.68
C9	58.32	56.96	35.14
C10	71.75	62.54	81.84
C11	71.74	62.53	82.40
C12	63.51	61.27	47.68
C13	54.23	52.54	33.91
C14	75.95	71.53	74.44
C15	75.97	71.55	75.91
C16	61.18	58.02	51.33
Ultimate base shear in Y direction	1065.30	994.21	965.27

Conclusions

The study results show that the three methods have similar ultimate base shear in Y direction. Thus, it verifies the feasibility of direct moment equilibrium method. For modern buildings, engineers can use the direct moment equilibrium method to analyze the ultimate base shear.

References

ACI Committee 318, “Building Code Requirements for Structural Concrete”(ACI 318-05) &Commentary (ACI 318R-05), 2005.

Generalized Optimal Locations of Viscous Dampers in Two-Way Asymmetrical Buildings

Jui-Liang Lin [1], Manh-Tien Bui [2] and Keh-Chyuan Tsai [3]

林瑞良 [1]、裴孟進 [2]、蔡克銓 [3]

Abstract

This study proposes a simple approach for finding the generalized optimal locations of linear viscous dampers in elastic two-way asymmetrical buildings under bi-directional ground excitations. The control target used in this optimization process is to maximize the average dissipation rate of the overall strain energy of the two-way asymmetrical building under the ground excitation of two bi-directional unit impulses. The proposed control target, referred to as the smeared damping ratio, is an intrinsic property of the building system. There are two advantages of the proposed approach that are appealing to engineering practice. First, the proposed approach does not require a complicated optimization algorithm. Second, due to the employment of an intrinsic property rather than a certain response parameter as the target performance index, the optimal damper locations resulting from the proposed approach are generalized, which are independent on the characteristics of input ground motions.

Keywords: asymmetric-plan buildings; viscous damper; optimal damper placement; seismic response history analysis; control target; optimization

Introduction

Finding an effective method of placing viscous dampers in a building is a common issue in earthquake engineering practice. This issue may be considered from the viewpoint of optimal damper placement, with the constraint of either a given number of added dampers or a specified structural peak response. Many published works have contributed significantly to this topic (Takewaki 1997, Lopez-Garcia 2001, Liu et al. 2005). Liu et al. (2005) classified the previous studies into four categories, *i.e.*, parametric studies, analytical optimization, evolutionary approaches, and heuristic approaches, and carried out extensive literature reviews of these four categories. Liu et al. (2005) pointed out that the optimal damper configuration might be different if the performance index is selected differently. Lopez-Garcia (2001) proposed the simplified sequential search algorithm (SSSA), which appears to be the simplest way of optimizing the damper locations developed thus far. In the SSSA, the designer sequentially adds one damper at the location with the greatest engineering demand, which is determined by performing a response history analysis of the building with the previously added dampers. Obviously, the optimal placement of dampers resulting from the SSSA depends on the applied seismic ground motions. Takewaki (1997) proposed optimizing the damper placement by minimizing the sum of the amplitudes of the transfer functions of the inter-story drifts evaluated at the undamped fundamental natural frequency. Because the transfer functions are dynamic structural properties irrespective of the characteristics of input ground motions, the optimal damper placement resulting from Takewaki's approach (1997) was independent of the input ground motions. These works highlight the fact that an approach optimizing the damper locations without using complicated optimization theories and without depending on the seismic ground motion is attractive to engineering practice.

The aim of this research is to provide a simple

[1] Research Fellow, National Center for Research on Earthquake Engineering, jllin@ncree.narl.org.tw.

[2] Graduate Student, Department of Civil Engineering, National Taiwan University, r98521266@ntu.edu.tw

[3] Professor, Department of Civil Engineering, National Taiwan University, kctsai@ntu.edu.tw.

approach for finding the generalized optimal locations of viscous dampers in two-way asymmetrical buildings. No complicated optimization algorithms or mathematical models will be adopted in this approach. For generalized optimal damper locations, an intrinsic property of the overall building system will be selected as the control target. Thus, the outcome of optimizing the damper locations will be independent of the response states of the building systems subjected to varied seismic ground motion inputs.

The energy-based Approach

When a single-degree-of-freedom (SDOF) oscillator is subjected to a unit impulse, its displacement response is the well-known unit impulse response function, denoted by $h(t)$:

$$h(t) = \frac{1}{m\omega_D} e^{-\xi\omega t} \sin(\omega_D t) \tag{1}$$

where m, ω, and ξ are the mass, vibration frequency, and damping ratio of the SDOF oscillator, respectively, and $\omega_D = \omega\sqrt{1-\xi^2}$. The unit impulse response function is the inverse Fourier transform of the frequency response function, which is a general dynamic property of the oscillator that is independent of the characteristics of the input excitations. The strain energy of the SDOF oscillator, denoted by E_S, is:

$$E_S\left(t\right) = \frac{1}{2}kh(t)^2 = \frac{1}{2m\left(1-\xi^2\right)} e^{-2\xi\omega t} \sin^2(\omega_D t) \tag{2}$$

where k is the stiffness of the SDOF oscillator. Thus, the damping ratio ξ of the SDOF oscillator can be approximated from Eq. 2 as:

$$\xi \approx \frac{\xi}{\sqrt{1-\xi^2}} = \frac{1}{4\pi} \ln\left(\frac{E_S\left(t\right)}{E_S\left(t+\dfrac{2\pi}{\omega_D}\right)}\right) \tag{3}$$

For a multi-degree-of-freedom (MDOF) building, the input seismic energy is the sum of the kinetic energy, the damping energy, and the absorbed energy. The absorbed energy, computed as the integration of the restoring force with respect to the displacement, is the sum of the energy dissipated by yielding and the elastic strain energy of the system. It is clear that the absorbed energy of an elastic MDOF building is only the elastic strain energy, E_S, and can be computed as $\left(\mathbf{Ku}\right)^T \mathbf{u}/2$, where $\mathbf{K}$ and $\mathbf{u}$ are the stiffness matrix and the displacement vector of the MDOF building, respectively. Nevertheless, the damping ratio of a multi-degree-of-freedom oscillator computed from Eq. 3 depends on which cycle of the strain energy history is considered. This is because the vibration of the higher modes usually accompanied by larger modal damping ratios, diminishes faster than the lower vibration modes. It is clear that the influence of an impulse on the structural responses decreases with elapsed time. Thus, for a multi-story asymmetrical building, the first and third peak values of the elastic strain energy history (marked in Fig. 1a), which represent the two peaks that occurred in the same direction during the first cycle of vibration, are used in Eq. 3. In addition, in order to consider two-way asymmetrical buildings under the excitation of bi-directional ground motions, the two loading cases shown in Fig. 1b are used to excite the multi-story buildings. The first case is a pair of in-phase impulses applied as the ground accelerations in the two horizontal directions. The second case is a pair of 180°-out-of-phase impulses applied as the ground accelerations in the two horizontal directions. It is assumed that the probabilities of occurrence of in-phase and 180°-out-of-phase impulses in the two orthogonal components of historical seismic ground motion records are equal. Thus, the index of the dissipation rate of the elastic strain energy, denoted by I_E, for an asymmetrical building is defined as follows:

$$I_E = \frac{1}{2}\left(\frac{\xi_1}{\sqrt{1-\xi_1^2}} + \frac{\xi_2}{\sqrt{1-\xi_2^2}}\right) \approx \frac{\xi_1+\xi_2}{2} \tag{4}$$

where ξ_1 and ξ_2 are the damping ratios computed from Eq. 3 for the building under the exertion of the first and second loading cases, respectively. Furthermore, $E_s(t)$ and $E_s(t+2\pi/\omega_D)$ shown in Eq. 3 represent the first and third peak values of the strain energy history of the building subjected to each loading case. As the I_E value increases, the damping system becomes more effective at dissipating energy. Thus, the control target used in the proposed approach for the generalized optimal damper placement in the asymmetrical buildings is to maximize the value of I_E. It is worth noting that the I_E index can be considered as the smeared damping ratio of an asymmetrical building with supplemental damping. The smeared damping ratio reflects the combined effects of the overall supplemental damping parameters on the suppression of the vibration of two-way asymmetrical buildings under bi-directional ground excitations.

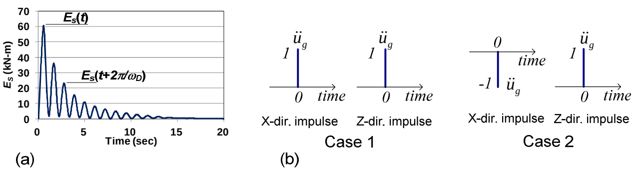

Figure 1. (a) The strain energy history of an elastic

multi-story two-way asymmetrical building subjected to a bi-directional unit impulse, and (b) the two applied loading cases.

This study assumed that the number of added viscous dampers, denoted by *ND*, and the damping coefficient of each damper are known. The design procedures using the proposed control target are as follows:

Step 1: Confirm the possible damper locations in the multi-story two-way asymmetrical building. The number of these locations is denoted by *NL*.

Step 2: Set $j = 1$.

Step 3: Place the *j*th damper at the *i*th possible location in the multi-story asymmetrical building with $j - 1$ previously added dampers. Because there are *NL* possible locations for placing the *j*th damper, *i.e.*, $i = 1$ to *NL*, this results in *NL* buildings with different locations of the *j*th damper. Perform the elastic response history analyses to each of these *NL* buildings using the two loading cases shown in Fig. 1b as the ground excitations.

Step 4: Compute the *NL* values of the index I_E, denoted by $I_{E,ij}$, where $i = 1$ to *NL*. The subscript *ij* indicates that the index value corresponds to the *j*th damper at the *i*th location.

Step 5: Find the *j*th damper's optimal location, in which the corresponding index value is the maximum among $I_{E,ij}$, where $i = 1$ to *NL*. Add the *j*th damper to the building at this obtained optimal location.

Step 6: Set $j = j + 1$. If *j* is larger than *ND*, then stop the design procedure. Otherwise, repeat Steps 3 to 6.

Numerical Validations

Figure 2 shows the floor plan and the elevation of the two nine-story example buildings, which is a variation of the symmetrical building located in Los Angeles that was used in the SAC steel research project (Krawinkler 2000). Each floor was simulated as a rigid diaphragm with a lumped mass located at the center of mass (CM). The center of rigidity (CR) was the geometric center. Details of the member sizes, materials, masses, and so forth can be found in the associated report (Krawinkler 2000). In addition, the CM is intentionally located away from the geometric center, resulting in the 20% and 15% eccentricity ratios in the *x*- and *z*-directions, respectively. Figure 2 indicates that the flexible side (FS) and the stiff side (SS) in the *x*-direction are Frame 6 and Frame 1, respectively. The FS and the SS in the *z*-direction are Frame F and Frame A, respectively. The only difference between these two example buildings is the mass moment of inertia of each story, which is equal to 1 and 2.5 times the values of the original symmetrical building. The example building with the mass moment of inertia equal to that of the original symmetrical building is denoted as Building TS. The other building is denoted as Building TF. Rayleigh damping with a 2% damping ratio for the first and the second vibration modes was assumed to represent the inherent damping.

Five pairs of historical ground motion records were selected for these analyses. The selected ground motion records were designated as LA21 to LA30 in the SAC steel research project for the buildings located in Los Angeles (Krawinkler 2000). The two orthogonal components were interchanged for application along the *x*- and *z*-directions, respectively. In addition, the *x*-directional component was varied by multiplying by plus and minus one. Therefore, this study applied a total of 20 pairs of ground motion records to each example building.

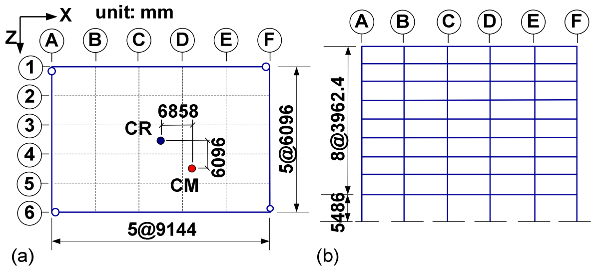

Figure 2. (a) The floor plan and (b) the elevation of Buildings TS and TF.

There were ten linear viscous dampers with a damping coefficient equal to 5×10^4 kN×sec/m to be diagonally installed in each example building. Because each floor was simulated as a rigid diaphragm, there were 36 possible locations for adding dampers. In the numerical validations, it was assumed that the optimal damper location could not be repeated, *i.e.*, there was only one damper at each optimal damper location. For the purpose of comparison, the optimal damper locations were also designed based on the SSSA approach. The control target used in the SSSA approach was the peak inter-story velocity, which is the same as that used by Lopez-Garcia (2001). In addition, the way of considering an ensemble of ground motion records by using SSSA is detailed in Lin et al. (2014). This type of SSSA is designated as the modified SSSA approach in this study.

The optimal damper locations of the ten viscous dampers in Buildings TS and TF resulting from the proposed approach, denoted as GOLD, and the modified SSSA approach, can be found in Lin et al. (2014). The designation GOLD for the proposed approach stands for the generalized optimal locations of dampers. Figures 3 and 4 compare the seismic responses of Buildings TS and TF with the ten dampers resulting from the GOLD with those resulting from the modified SSSA approach. For convenience, the modified SSSA approach is simply denoted as SSSA in these figures. Figure 3 shows the strain energy history of buildings TS and TF with and without the ten dampers under the exertion of the two cases of ground unit impulses (Fig. 1b). It is apparent in Fig. 3 that buildings TS and TF with the ten dampers located using the GOLD reached a stationary state faster than the two buildings with the dampers placed using the modified SSSA approach. In other words, the arrangements of the ten dampers in buildings TS and TF obtained by using the GOLD were more effective at dissipating the strain energy than those obtained by using the modified SSSA approach.

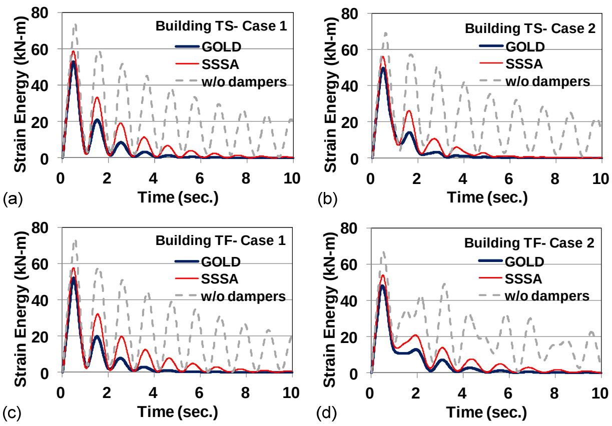

Figure 3. The strain energy histories of Building TS under loading (a) case 1 and (b) case 2, and of Building TF under loading (c) case 1 and (d) case 2.

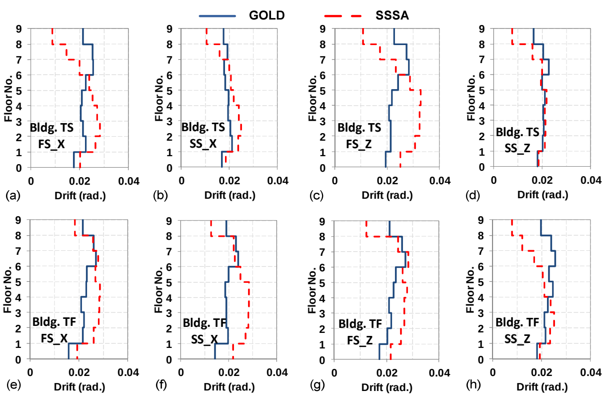

Figure 4. The average peak story drifts on (a) the FS and (b) the SS in the *x*-direction, and on (c) the FS and (d) the SS in the *z*-direction of Building TS. The average peak story drifts on (e) the FS and (f) the SS in the *x*-direction, and on (g) the FS and (h) the SS in the *z*-direction of Building TF.

Figure 4 shows the peak story drifts on the four floor sides. Note that the abscissa values shown in Fig. 4 are the average of the 20 peak values obtained by applying the 20 pairs of ground motions to the buildings. Figure 4 shows that the average peak story drifts on the four floor sides obtained using the GOLD were more uniformly distributed along the building height than those obtained using the modified SSSA approach. Furthermore, the average peak story drifts from the first to the sixth stories were more significantly reduced using the GOLD than the modified SSSA approach, except in the *z*-directional SS (Fig. 4). On the contrary, the average peak story drifts from the seventh to the ninth stories resulting from the modified SSSA approach were less than those resulting from the GOLD. This is reasonable because the layout of the added dampers using the modified SSSA approach concentrated on the upper stories (Lin et al. 2014).

Conclusions

This study demonstrated a satisfactory approach for finding the generalized optimal locations of viscous dampers by maximizing the dissipation rate of the overall strain energy of two-way asymmetrical buildings under the excitation of the two pairs of unit impulses. The defined dissipation rate of the overall strain energy used in this study is referred to as the smeared damping ratio, which is an intrinsic characteristic of the building system rather than any seismic response of the building system. In the numerical validations, the proposed approach ensured that the strain energy of the two example buildings was dissipated as fast as possible, which simultaneously resulted in satisfactory seismic performance. In addition, the optimized damper configuration obtained by using the proposed approach is generalized, *i.e.*, not aimed at any specific set of seismic ground motions. This proposed approach is straightforward and suitable for engineering practice.

References

Krawinkler, H. (2000), “State of the art report on systems performance of steel moment frames subject to earthquake ground shaking”, *Report No. FEMA-355C*, SAC Joint Venture.

Lin, J.L., Bui, M.T., Tsai, K.C. (2014), “An Energy-Based Approach to the Generalized Optimal Locations of Viscous Dampers in Two-Way Asymmetrical Buildings”, *Earthquake Spectra*, 30 (2): 867-889.

Liu, W., Tong, M., Lee, G.C. (2005), “Optimization methodology for damper configuration based on building performance indices”, *Journal of Structural Engineering* (ASCE), 131(11): 1746-1756.

Lopez-Garcia, D. (2001), “A simple method for the design of optimal damper configurations in MDOF structures”, *Earthquake Spectra*, 17: 387-398.

Takewaki, I. (1997), “Optimal damper placement for minimum transfer functions”, *Earthquake Engineering and Structural Dynamics*, 26: 1113-1124.

A Study of the Safety Factor of the Capacity Spectrum Method for Multi-Story Structures

Yeong-Kae Yeh [1] and Te-Kuang Chow [2]

葉勇凱 [1]、周德光 [2]

Abstract

Currently, engineers in Taiwan often use pushover analysis based on the capacity spectrum method to make detailed seismic evaluations of structures. The performance-target ground acceleration is compared with the peak ground acceleration (PGA) at the site of a design earthquake with a 475-year return period to evaluate the sufficiency of a structure's seismic capacity. However, according to FEMA 440, these evaluated results are too conservative for short-period structures. In this report, a nonlinear dynamic analysis of five-story and ten-story structures is performed to study the inherent safety factor of the capacity spectrum method and its relationship to the story number, the dispersive hysteretic energy, and the characteristics of the input seismic record. From the analysis results, this safety factor is found to be 3.09 for the five-story structure and 3.43 for the ten-story structure. It is also found to be less affected by the dispersive hysteretic energy, and to be influenced by the characteristics of the input seismic record. Although the analysis error of the capacity spectrum method with a single mode is probably larger for high-rise buildings than for low-rise buildings, the capacity spectrum method still has a high value for the safety factor.

Keywords: detailed seismic evaluation, nonlinear pushover analysis, capacity spectrum method, nonlinear dynamic analysis,

Introduction

Because of the advancement of seismic research and seismic codes, the seismic capacities of old buildings need to be examined to determine whether they need to be retrofitted or demolished. Detailed seismic evaluation procedures are often used to confirm the seismic capacities of existing buildings. Currently, the most widely used detailed evaluation method is nonlinear pushover analysis, which aims to obtain the capacity curves of structures; that is, establishing of the relationship between the base shear and roof displacement. Based on the building's performance needs, a performance point is set on the capacity curve to seek a design earthquake that can cause this performance-point roof displacement. This performance-target earthquake is represented by the associated design response spectrum and maximum ground acceleration. The methods used to identify the performance-target earthquake from the capacity curve can be divided into two categories: one is the capacity spectrum method suggested by ATC 40 (ATC, 1996), the other is the coefficient method suggested by FEMA 356 (FEMA, 2000).

In Taiwan the most popular detailed seismic evaluation methods are the "Taiwan Earthquake Assessment for structures by Pushover Analysis" (TEASPA) developed by the National Center for Research on Earthquake Engineering (NCREE) and the "Seismic Evaluation of Reinforced Concrete Buildings" (SERCB) developed by the team led by Prof. I-Chau Tsai from the National Taiwan University. Both of these methods are based on the capacity spectrum method of ATC 40. The pushover analysis based on the capacity spectrum method is an approximation method to simulate the roof displacement of a structure calculated by nonlinear dynamic analysis. In the FEMA 440 (FEMA, 2005) report, the capacity spectrum method of ATC 40 is

[1] Research Fellow, National Center for Research on Earthquake Engineering, ykyeh@ncree.narl.org.tw
[2] Assistant Technologist, National Center for Research on Earthquake Engineering, tkchow@ncree.narl.org.tw

noted to be too conservative for single-degree-of-freedom systems with periods less than 0.5 s. The capacity spectrum method has been widely used in the seismic evaluation and retrofitting of existing buildings in Taiwan, so it is necessary to study the implicit safety factor of the method, its relationship with the story number of the structure, the hysteretic energy dissipation of its elements, and the characteristics of the input seismic records.

Last year, our research has shown that the capacity spectrum method is a conservative method for relatively short-period structures and the safety factor increases as the period of the structure is reduced. This year, we researched the relationship between the safety factor and the number of stories of the structure. The analysis models consider five-story and ten-story structures.

The third edition of the NCREE Technology Handbook is used to define the nonlinear hinges of the structure, and the software packages ETABS and PERFORM3D are adopted to perform the nonlinear pushover analysis and the nonlinear dynamic analysis respectively.

Analysis of a Five-Story Structure

As shown in Fig.1, the five-story structure is 900 cm long, 900 cm wide, and 1650 cm high. The reference lines of the beams are set at the upper faces. The height of each story is 330 cm. The floor has a thickness of 12 cm and is set as a rigid diaphragm. The beam section is 30×50 cm and the column section is 45×45 cm. The offsets of the columns and beams are assumed to be semi-rigid with a rigid zone factor of 0.9.

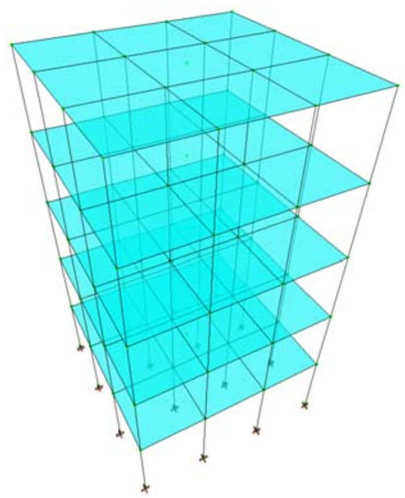

Fig. 1 The three-span five-story structure.

To simulate older buildings, the concrete strength is set at 160 kgf/cm^2 and the reinforcement strength is set at 2800 kgf/cm^2. The vertical load comes from the self-weight of the members and the floor's uniform loading is set at 0.01 kgf/cm^2. The third edition of the NCREE Technology Handbook is used to define the nonlinear hinges at both ends of the beams and columns.

The X-direction is set as the direction for the pushover analysis. At first, a vertical loading is applied under force control. Then, under displacement control, lateral forces are applied to the centers of mass of each floor along the X-direction. The capacity curve is shown in Fig. 2. The site is located in the eastern part of Tainan City and the site ground is class 2. A roof displacement of 21.2 cm is chosen as the performance-target displacement and the damping modification factor is set at 0.33. According to the capacity spectrum method, the performance-target ground acceleration is calculated as 0.469g, which corresponds to a roof displacement of 21.2 cm in an earthquake with a PGA of 0.469g for this structure. However, the real roof displacement in an actual earthquake will be smaller. The ratio between the estimated roof displacement and the actual roof displacement is the studied safety factor.

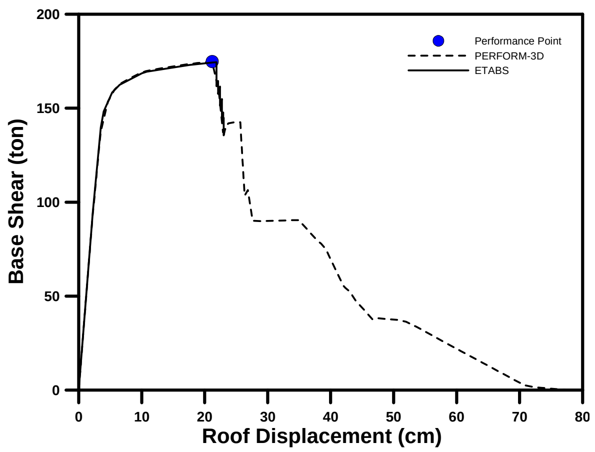

Fig. 2 Capacity curve of the five-storey structure.

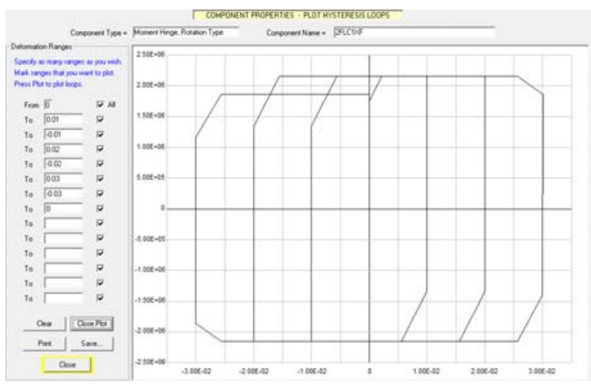

Fig. 3 Hysteretic behavior of a nonlinear hinge of columns with no stiffness degradation.

For the nonlinear dynamic analyses, there are two types of hysteretic behavior to process: one where the stiffness does not degrade during the analysis, as shown in Fig. 3, and another where the stiffness does degrade, as shown in Fig. 4.

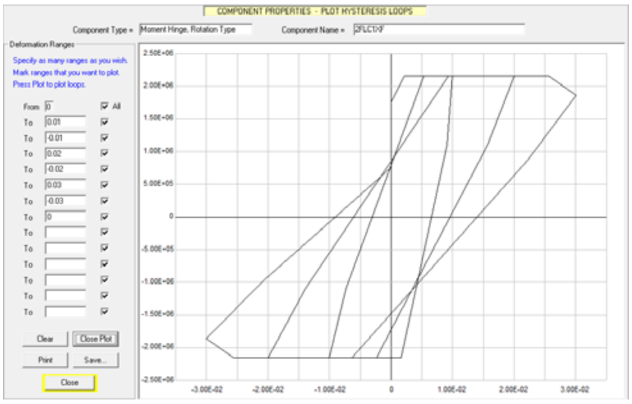

Fig. 4 Hysteretic behavior of a nonlinear hinge of columns with stiffness degradation.

The input earthquakes are chosen from the seismic databank of the Central Weather Bureau. The seismic intensities of all twenty seismic records are larger than 6 and the seismic stations are all located on class-2 ground. The PGAs of these records lie between 250 gal and 550 gal. Their response spectra and the average spectrum are shown in Fig. 5.

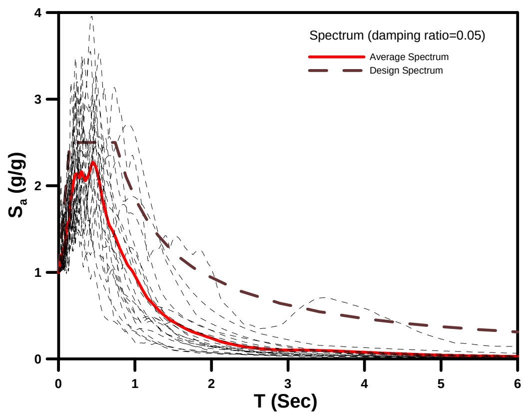

Fig. 5 Response spectra of the twenty chosen earthquakes.

The PGAs of these twenty seismic records were normalized to 0.469 g then used as the input motions for the nonlinear dynamic analyses. The calculated maximum roof displacements were compared with the performance-target displacement of 21.2 cm. As shown in Table 1, the average displacement ratio of the performance-target displacements and the calculated roof displacements of the cases with no stiffness degradation is 3.4, which is the implicit safety factor; for cases with stiffness degradation, the implicit safety factor is 3.09.

Analysis of a Ten-Story Structure

A ten-story structure, as shown in Fig. 6, was also used as an analysis model to discuss the relationship between the implicit safety factor of the capacity spectrum method and number of stories.

The PGAs of the twenty seismic records were normalized to 0.469 g, which is the performance-target ground acceleration for the performance-target displacement of 29.1 cm. They were then used as the input motions for the nonlinear dynamic analyses. The calculated maximum roof displacements were compared with the performance-target displacement of 29.1 cm. As shown in Table 2, the average displacement ratio of the performance-target displacements and the calculated roof displacements of the cases with no stiffness degradation is 3.53, which is the implicit safety factor; for the cases with stiffness degradation, the implicit safety factor is 3.43.

Table 1 The displacement ratios of the performance-target displacements and the calculated roof displacements of the five-story structure.

Earthquake	Disp. Ratio (No Degradation)	Disp. Ratio (Degradation)
1	3.13	3.10
2	2.76	1.66
3	1.96	1.92
4	2.94	2.38
5	6.46	6.46
6	4.23	3.77
7	3.08	2.90
8	4.26	4.26
9	1.78	1.31
10	2.09	1.50
11	2.49	2.16
12	3.23	2.99
13	3.98	3.43
14	4.63	4.59
15	3.80	3.80
16	4.20	3.81
17	2.22	1.77
18	5.06	5.06
19	2.55	2.53
20	3.17	2.49
AVE	3.40	3.09
STD	1.18	1.33

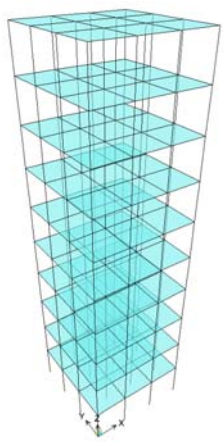

Fig. 6 The three-span ten-story structure.

Table 2 The displacement ratios of the performance-target displacements and the calculated roof displacements of the ten-story structure

Earthquake	Disp. Ratio (No Degradation)	Disp. Ratio (Degradation)
1	3.53	3.53
2	2.21	2.10
3	2.10	2.06
4	2.01	1.88
5	8.20	8.08
6	3.65	3.65
7	4.81	4.46
8	4.30	4.30
9	1.45	1.37
10	2.02	1.42
11	2.08	1.93
12	3.74	3.70
13	6.64	6.71
14	4.34	4.34
15	3.02	3.02
16	3.00	2.95
17	2.18	2.34
18	4.97	4.97
19	2.41	2.41
20	3.90	3.29
AVE	3.53	3.43
STD	1.70	1.73

Conclusions

In this research, a five-story structure with a period of 0.510 s and a ten-story structure with a period 0.741 s were used for nonlinear dynamic analyses. A total of twenty medium-to-large seismic records were adopted as input motions. Two types of hysteretic behavior of the nonlinear hinges were considered for the structural models. The first one is that its stiffness does not degrade during the analysis, and the second one is that its stiffness does degrade. From the analysis results, we can make the following conclusions:

1. Although the FEMA 440 report shows that the capacity spectrum method might not overestimate the roof displacement for systems with periods larger than 0.5 s, according to our research the capacity spectrum method is still a conservative evaluation method for a five-story structure with a period of 0.510 s and a ten-story structure with a period of 0.741 s. For the second type of hysteretic behavior of the nonlinear hinges, the five-story structure has an implicit safety factor of 3.09 and the ten-story structure has an implicit safety factor of 3.43.

2. Because of the small responses of the performance-target seismic motions, the behavior of the structure is close to vibrating along the elastic stiffness. Few complete hysteretic loops are observed, so the roof displacement is less dependent on the hysteretic behavior of the structure.

3. The maximum roof displacement has a positive relationship with the response spectrum at the dominant period of the structure. The nonlinear responses of the structures are closely dependent on the elastic periods of the structures.

4. For the five-story structure, the difference in lateral distribution of story shear between modal pushover and nonlinear dynamic analysis is small. The capacity curve of pushover analysis can be used to simulate the envelope of hysteretic loops.

5. For the ten-story structure the difference of lateral distribution of story shear between the modal pushover and nonlinear dynamic analyses is obvious. The capacity curve of the pushover analysis cannot be used to simulate the envelope of the hysteretic loops, but the capacity spectrum method used to simulate the roof displacement still has a large safety factor.

References

Applied Technology Council (ATC) (1996), “ATC-40 Seismic Evaluation and Retrofit of Concrete Buildings”, prepared by the Applied Technology Council, Redwood City, Calif.

Federal Emergency Management Agency (FEMA) (2000), “Prestandard and Commentary for the Seismic Rehabilitation of Buildings (FEMA Publication 356)”, prepared by the American Society of Civil Engineers, Washington, D.C.

Federal Emergency Management Agency (FEMA) (2005), “FEMA 440 Improvement of Nonlinear Static Seismic Analysis Procedures”, prepared by the Applied Technology Council for the Federal Emergency Management Agency, Washington, D.C.

Cyclic Loading Test for Flanged Joints of the RHR Piping System

Juin-Fu Chai[1] ,Wen-Fang Wu[2] ,Fan-Ru Lin[3] ,Zih-Yu Lai[4] ,Ming-Yi Shen[4] , Yan-Fang Liu[5]

柴駿甫 [1]、吳文芳 [2]、林凡茹 [3]、賴姿妤 [4]、沈明毅 [4]、劉嚴方 [5]

Abstract

According to the results of a seismic risk assessment presented in the Final Safety Analysis Report for a power plant in Taiwan, a failure of the RHR piping system occurs in both of the two accident sequences with the highest contributions to core damage. For the required seismic response-history analysis of the RHR piping systems, we set up the pure bending test to find the flanged joint parameters, such as the translation stiffness and rotation stiffness. Finally, an assessment of the performance of bolted flanged joints is conducted. In the further, we will develop detailed numerical models of flanged joints and validation these studies through bending tests, and will also propose a simplified model to improve the effectiveness of the fragility analysis of the RHR piping system.

Keywords：Pure bending test, flanged joints, stiffness

Introduction

In order to conduct a more accurate fragility analysis of the RHR piping system in Seismic Probabilistic Risk Assessment (SPRA), it is necessary to establish a reliable numerical model of the piping system. However, the commonly used numerical models for piping joints, such as flanges, cannot simulate the non-linear behavior well. Therefore, in this study, a preliminary experimental study was conducted to investigate the mechanical behavior of piping joints under cyclic pure bending and to provide data to enhance the accuracy of the finite element models. The further study, the aim is to propose an acceptable simplified model of the piping joints to improve the efficiency of numerical analysis for RHR piping system. The non-linear behavior of piping joints under cyclic pure bending is also discussed.

Testing Setup

Quasi-static tests under cyclic loading were conducted for bolted flanged joints. In order to apply pure-bending at the flanged joints, the testing setup was arranged to be the four-point bending configuration. As shown in Figure 1, a 1000 kN actuator was employed for the tests. The cyclic loading was applied by an actuator through an adapter composed of a beam and rotary fixtures allocated to both sides of the flanged joint to impose the pure bending load on the segment between rotary fixtures.

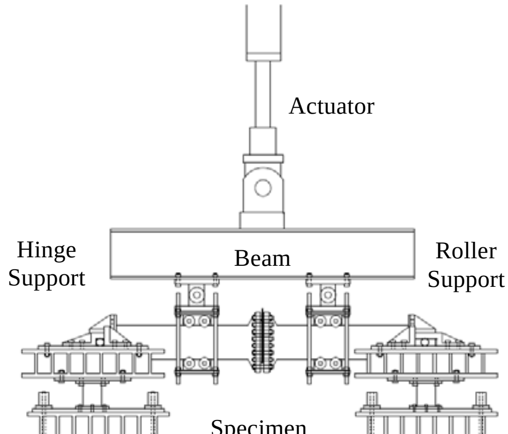

Fig.1. A scheme of testing setup

Test specimens

The specimen consisted of two equal-length

[1] Research Fellow, National Center for Research on Earthquake Engineering
[2] Professor, Department of Mechanical Engineering, National Taiwan University
[3] Assistant Researcher, National Center for Research on Earthquake Engineering
[4] Research Assistant, National Center for Research on Earthquake Engineering
[5] Graduate, Department of Mechanical Engineering, National Taiwan University

straight pipe segments (Schedule 40), which were connected with a flanged joint via welding (Figure 2). The pipe material was SA333Gr6 carbon steel with yield and ultimate tensile strengths of 324 and 449 MPa, respectively. The nominal diameters of the pipes are 300 mm. As shown in Figure3, the flange joint include a spiral wound gasket and sixteen bolts and nuts. In order to observe the leakage behavior, an internal pressure of 8 kgf/cm^2 was applied by feeding water into the specimens.

Fig.2 The appearance of the specimen

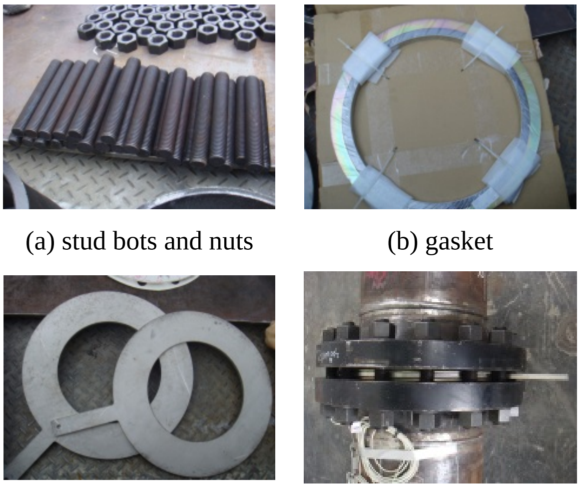

(a) stud bots and nuts

(b) gasket

(c) pressure breakdown orifices

(d) flange

Fig. 3 Components of the specimens

Loading Protocol

The loading protocol was designed according to the cyclic displacement schedules proposed by ISO-16670. The v_u is determined by the mean of the ultimate displacements obtained using monotonic testing. In this study, v_u was decided to be 50 mm according to the analysis results of the preliminary numerical model. Figure 4 depicts the cyclic loading protocol of the tests.

Reverse loading with an amplitude smaller than 10% of v_u was applied for one cycle while other were applied for three cycles. The maximum amplitude of the loading protocol was set to be 70 mm.

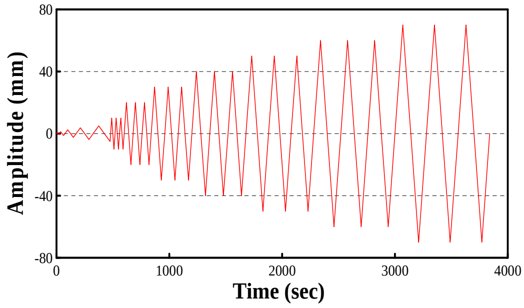

Fig. 4 The cyclic loading protocol

Measurement

In this study, the specimens were instrumented by strain gauges, tiltmeters, load cells, a water pressure gauge and an optical tracking system. The water pressure gauge monitored the changes of internal pressure during tests. In order to observe the strain of the welded connection between the pipe and the joint, the strain gauges SE1 to SE4 and SW1 to SW4 were placed at the welded connection of the flange and SE5, SE6, SW5, SW6 were placed at the pipes with a distance of 50 mm from the welded connections between pipes and the flanged joint (Figure 5). The strain gauges were arranged on the radian or longitudinal axes of the specimens.

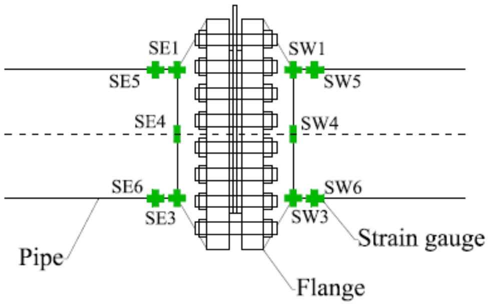

Fig. 5 Placement of strain gauges

Figure 6 depicts the arrangement of the tiltmeters and the optical tracking system. The rotation response measured by sensors A3 and A4 near the flanged joint were used to calculate the deflection angles of the joint on both side. The deflection angles were used to conduct moment-rotation curves and determine the rotation stiffness.

The motion of points measured by optical trackers was used to obtain the deformation of the specimens, the axial offset of roller bearing and the displacement of the centerline of specimens during the tests.

Load cells were placed at the bottom of both supports to measure the reaction forces. The applied moment was calculated by multiplying the reaction forces measured at the supports by the distance from the evaluated point to the support. As shown in Figure 7, sensors labeled as LA measured the axial force in the gravity direction, and sensors labeled as LS measured the shear force in the transverse direction.

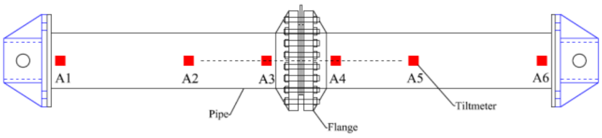

(a) tiltmenters

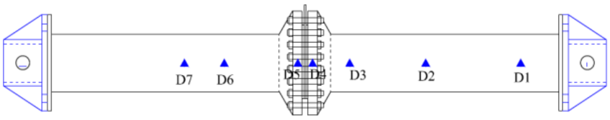

(b) optical trackers

Fig. 6 Placement of measurement devices

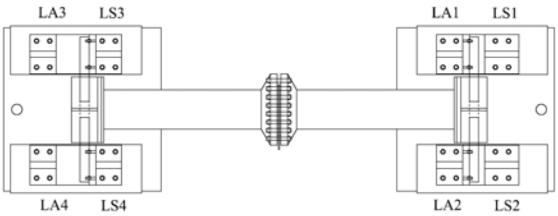

Fig. 7 Placement of load cells

Test results and observations

During the test, leakage occurred as a result of the loosening of bolts without breakage. Figure 8 depicts the measured loading curves and associated measured reaction force for the specimens. Figure 9 shows the rotation response around the transverse axis of the specimens measured by the tiltmeters during testing. The rotation of the specimen remained symmetry. The rotation angle gradually increased as the distance from the measuring point to the zero-slope point increased.

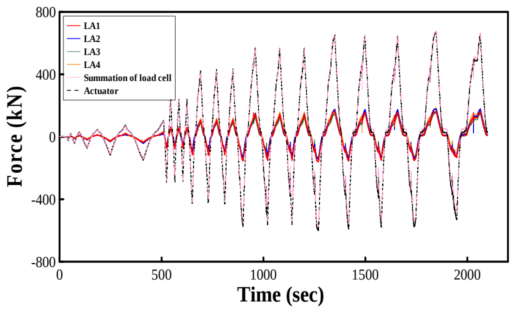

Fig. 8 Measured loading curves

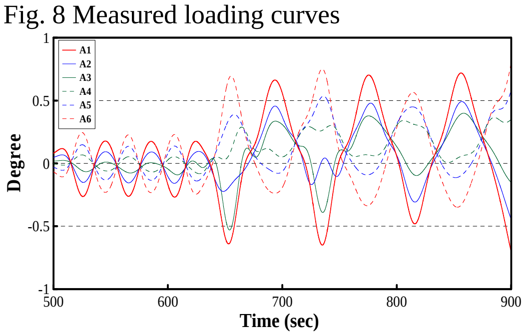

Fig. 9 Rotation responses

The strain curves of specimens are presented in Figure 10 shows the variation of the longitudinal strain at the welded connection between the flanged joint and piping segments SE1X and SE5X can be seen. It was found that the accumulated strain of the welded connection started at this segment. However, the strain value was much smaller than measured at the piping segment. The excessive strain of the piping segment occurred at a large cyclic loading, owing to the plastic deformation at the loading point.

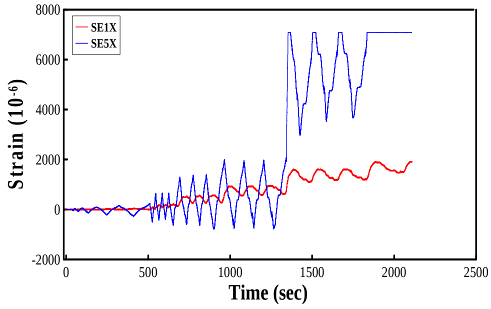

Fig. 10 Strain curves of the specimens

The force-displacement hysteretic loops of the flange specimen were constructed using the measured displacement and associated force of the actuator (Figure 11(a)). The initial stiffness of the vertical displacement in the elastic stage is approximately 30 kN/mm. For the signals measured by the load cells and tiltmeters, the moment-rotation hysteretic loops for the flanged joint are presented in Figure 11(b). The rotation stiffness in the elastic stage is around 1000 kN-m/° and decreases to 250 kN-m/° in the plastic stage, owing to several loosened bolts at the top and bottom of the flange. These bolts were loosened without damage when the displacement applied by the actuator and the associated moment were 20 mm and 100 kN-m, respectively.

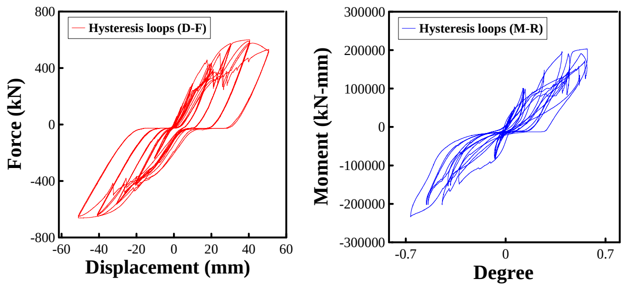

(a)force-displacement (b)moment-rotation

Fig. 11 Hysteresis curves

Assessment of the Performance of Bolted Flanged Joints

Flanged joints belonging to Class 1 components of the nuclear facility, which are subjected to combinations of moment and pressure, shall meet the requirements of the ASME Code and the design specifications. The flanged joint tested in this study belongs to the RHR piping system, the postulated plant events according for ASME Service Levels B and D.

The moment demands for Levels B and D are calculated according to the equations given in the paragraph NB-3658 “Analysis of flange joints” in the ASME Division 1 – Subsection NB in order to prevent excessive leakage at the joints. In the ASME Code, the pressure shall not exceed 1.1 times the rated pressure for Level B service limits. The acceptance criteria of Level B given by Eqs.1 and 2 shall be satisfied. In addition, the acceptance criteria of Level D given by Eqs.3 shall be also satisfied.

$$M_{fs} \leq 21.7(\mathrm{S}_y / 250) \cdot CA_b \quad (1)$$

$$M_{fd} \leq 43.4(\mathrm{S}_y / 250) \cdot CA_b \quad (2)$$

$$M_{fd} \leq [78.1A_b - (\pi / 16)\,\mathrm{D}_f^2 \mathrm{P}_{fd}]C(\mathrm{S}_y / 250) \quad (3)$$

where,

A_b: total cross-sectional area of bolt at the root of thread or section of least diameter under stress, mm^2.

S_y: yield strength of the flange material at the design temperature, MPa;

M_{fs}: bending or torsion moment (considered separately) applied to the joint as a result of weight, thermal expansion of the piping, sustained anchor movements, relief valve steady-state thrust, and other sustained mechanical loads applied to the flanged joint during the design of service conditions, N-mm;

M_{fd}: bending or torsion moment (considered separately) as defined for M_{fs}, but including dynamic loading, N-mm;

D_f: outside diameter of the raised face, mm; and

P_{fd}: pressure concurrent with M_{fd}, MPa.

According to the test results, the leakage occurred when the bending moment was 100 kN-m, and was due to the loosened flange bolts, which showed no permanent deformation or damage to other components of the flanged joint. It can be found that the capacity of the flanged joints against leakage is well above the allowable bending moment of 50.58 kN-m defined for Service Level B under the consideration of loads induced by Operating Basis Earthquake (OBE) and normal operation or system operational transients. However, the allowable bending moment is defined by 176 kN-m for Service Level D under the consideration of loads induced by normal operation, Safe Shutdown Earthquake (SSE), the break Loss of Coolant Accident (LOCA) and/or Safety/relief valves. This implies that the code-defined capacity for Service Level D may be less conservative for the purpose of preventing excessive leakage at the flanged joint as a result of loosened bolts.

Conclusions

A failure of the RHR piping system occurs in both of the two accident sequences with the highest contributions to core damage. The findings are summarized as following:

(1) Leakage occurred at a moment of around 100 kN owing to the loosening of bolts without breakage.

(2) The stiffness values of the piping joints were preliminarily derived from the test results to establish simplified models for future studies. According to the force applied by the actuator, the initial stiffness of vertical translation is approximately 30 kN/mm for the flange joint. Moreover, the initial and final stiffness of transverse rotation are approximately 1000 and 250 kN-m/° for the flanged joint.

References

International Organization for Standardization, (2003). ”Joints made with mechanical fasteners-Quasi-static reversed cyclic test method”, ISO-16670.

2007 ASME BPVC, (2009). Section III, Division 1, Subsection NB, “Rules for Construction of Nuclear Facility Components - Class 1 Components”, ASME.

G&E Engineering Systems Inc., (1997). “Preliminary Safety Analysis Report for Lungmen Units 1&2”, Taiwan Power Company, Taiwan.

Study on Composite Bridge for Emergency Disaster Relief

Fang-Yao Yeh[1], Kuo-Chun Chang[2], Yu-Chi Sung[3] and Hsiao-Hui Hung[4]

葉芳耀 [1]、張國鎮 [2]、宋裕祺 [3]、洪曉慧 [4]

Abstract

Owing to the recent extreme climate conditions, threats from natural disasters such as typhoons, floods, and earthquakes have increased in Taiwan over the years. Such natural disasters cause damage to bridges, consequently preventing the provision of emergency relief services to communities living in remote areas. In order to provide quick emergency relief, the simple construction of a temporary bridge becomes critical for the transportation of food and medical supplies to disaster areas. While composite materials for footbridges and vehicular traffic applications have been widely used overseas, they are not suitable for disaster relief applications. The objective of this paper is to present a novel bridge structure for a portable, reusable, and lightweight bridge. This paper focuses on the design concept and experimental verification of a temporary composite bridge for disaster relief. Ultimately, it advocates composite bridges for disaster relief applications.

Keywords: Composite emergency bridge; Cable-stayed composite bridge; lightweight, portable, and reusable bridge

Introduction

Owing to the recent extreme climate conditions, typhoons, floods, and earthquakes have caused great damage to Taiwan. For instance, 88 floods were caused by Typhoon Morakot in 2009, causing damage to more than 200 bridges and washing away more than 100 bridges (Fig. 1a). Chi-Chi Earthquake in 1999 also caused damage to more than 150 bridges (Fig. 1b), resulting in communities trapped in isolated mountain regions to which emergency relief supplies could not be easily delivered.

(a)

(b)

Fig. 1 Damage of a bridge and disaster rescue due to: (a) Morakot Typhoon and (b) Chi-Chi Earthquake

During the last few years advanced composite materials have been increasingly used in the aerospace, marine, and automobile industries due to their favorable engineering properties such as high specific strength and stiffness, lower density, high fatigue endurance, and high damping. The advantages of Fiber Reinforced Polymer (FRP) composites make them attractive for use in replacement decks or in new bridge systems, such as (1) bridge decks, including FRP rebar reinforced concrete deck systems, FRP grid and grating reinforced concrete deck systems, deck systems made completely from FRP composites, and hybrid FRP plate reinforced concrete deck systems; (2) FRP composite bridge girders and beams, including Glass Fiber Reinforced Polymer (GFRP) composite girders, Carbon Fiber Reinforced Polymer (CFRP) composite girders, and hybrid girders; and (3) slab-on-girder bridge systems [Cheng et. al., 2006; Hollaway, 2001].

Nowadays, FRP composites are used mostly in deck systems, footbridges, and vehicle bridges. This

[1] Research Fellow, National Center for Research on Earthquake Engineering, fyyeh@ncree.narl.org.tw
[2] Director, National Center for Research on Earthquake Engineering, kcchang@ncree.narl.org.tw
Professor, Department of Civil Engineering, National Taiwan University, ciekuo@ntu.edu.tw
[3] Professor, Department of Civil Engineering, National Taipei University of Technology, sungyc@ntut.edu.tw
[4] Research Fellow, National Center for Research on Earthquake Engineering, hhung@ncree.narl.org.tw

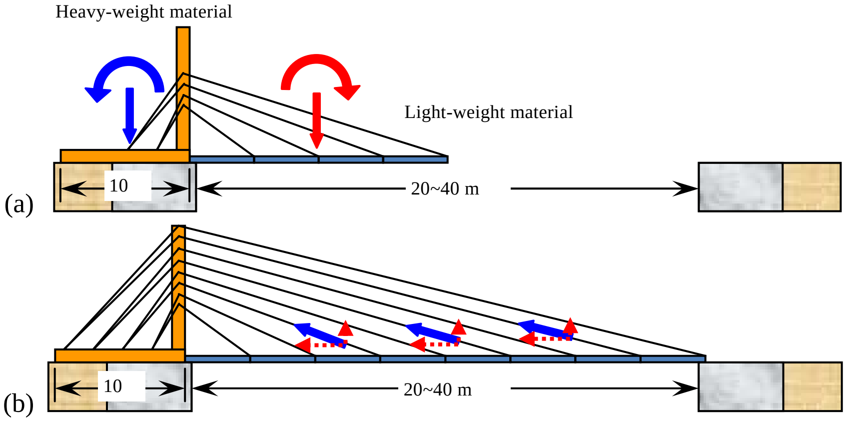

Fig. 2 Innovation and concept of a composite bridge for emergency disaster relief: (a) the construction stage and (b) the commissioning completion stage

paper focuses on the advantages of FRP composites in applications for typhoon, flood, and earthquake disaster rescue in Taiwan. The objective of this paper is to present a novel bridge structure for a portable, reusable, and lightweight bridge. It also focuses on the design concept and experimental verification of a temporary composite bridge for disaster relief and promotes composite bridges for disaster relief applications.

Concept of Temporary Composite Bridge

This study develops a temporary bridge system by using a self-weight balance approach and a cantilever incremental launching method. An asymmetric self-anchored cable-stayed bridge is proposed. The structural segments constructed by heavyweight materials (e.g., steel and concrete) are used as counter-weights at the rescue end and the cross-river segments are constructed by lightweight materials (e.g., composite materials) in order to increase the span to easily reach the isolated island end without any supports or foundations (Fig. 2).

The advantages of this composite bridge include the following: (1) during the construction stage, the asymmetric self-anchored cable-stayed bridge is easily constructed from the rescue end to the isolated island end by using the self-weight balance of heavyweight structural segments and lightweight cross-river segments. The wires of the cable-stayed bridge are suitable for the construction of cross-river segments by using the cantilever incremental launching method (Fig. 2a), and (2) during the commissioning completion stage, these wires are effective in reducing the deformation of the bridge caused by live loads from traffic (Fig. 2b).

Design of Temporary Composite Bridge

In order to confirm the construction and usability of the lightweight temporary bridge for disaster relief, a potential scenario for testing is required, and is as follows: a bridge with a span of 20 m was damaged in a disaster area, and thus, a temporary bridge for the transportation and delivery of relief supplies is needed. The concept of weight balance and the incremental launching method proposed in the previous section are considered in the novel emergency bridge design. We have designed a steel-composite cable-stayed bridge with a span of 20 m, a width of 3 m, and a live load of 5 tons (for transportation of rescue goods via a truck weighing 3.5 tons) and a deflection-to-span ratio of L/400 for the assembled and river-crossing test. Fig. 3 shows the design results of the asymmetric self-anchored cable-stayed bridge. Seven parallel steel girders and H-shape pillars using A572 grade 50 steel with a 294 mm × 200 mm × 8 mm × 12 mm cross section on the A1 side abutment are used as the weight balance structural module, five parallel FRP girders using GFRP with a 410 mm × 200 mm × 18 mm × 20 mm cross section are used as crossing structural module, and double-H-shape steel cross beams are used to aid the crossing of the river (Fig. 3a). We used a steel frame on the A1 side abutment as a counterweight and a cable-stayed type bridge to quickly assemble the lightweight GFRP temporary bridge via the incremental launching method to cross the river and therefore achieve the goal of providing disaster relief. By using the same capacity for the connection design, the numerical result shows that the connection between the steel girder and the GFRP girder is not the critical connection; instead, the critical connection is located at connection G4 between GFRP segment C and GFRP segment D (Fig. 3b).

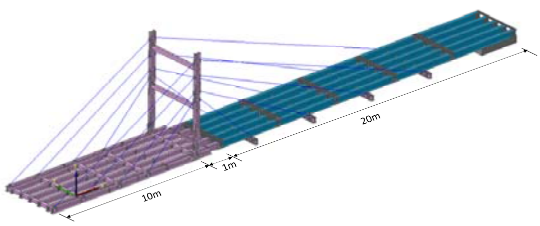

(a)

(b)
Fig. 3 Design results of the 20 m span temporary composite bridge: (a) the 3D view and (b) the shape of deformation

Experimental Verification of Composite Bridge for Emergency Disaster Relief

Construction Sequences and River-crossing Tests

The lightweight temporary composite bridge system includes a weight balance structural module, a bridge tower structural module, a crossing structural module, and connection cables. The weight balance structural module and the bridge tower structural module are constructed of steel, concrete, and any other heavyweight materials as structural segments. The crossing structural module is constructed of composites and any other lightweight materials. The construction sequence is as follows: (1) assemble the structural segments to complete the weight balance structural module (Fig. 4a); (2) assemble the structural segments to complete the bridge tower structural module, fix the bottom part to the weight balance structural module, and couple the top part to the weight balance structural module via at least one connection cable (Fig. 4b); and (3) assemble the crossing segments between the rescue end and the isolated island end gap (Fig. 4c) to complete the crossing structural module and couple it to the top part of the bridge tower structural module via at least one connection cable (Fig. 4d).

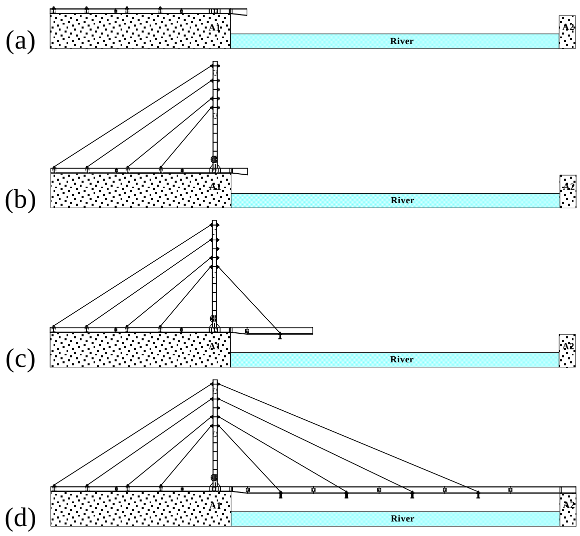

Fig. 4 Construction sequences: (a) assemble the weight balance structural module, (b) assemble the bridge tower structural module, (c) assemble the crossing structural module, and (d) complete the construction of the bridge

The construction sequence is shown in Fig. 5 and is as follows: (1) assembly of seven parallel steel girders with 294 mm × 200 mm × 8 mm × 12 mm cross sections and a total length of 12 m (3@4m), and a bolted connection at the web of the girder with box cross beams (200 mm × 200 mm × 6 mm) (Fig. 5a and 5b); (2) assembly of H-shape pillars with 18 connection devices for the steel cable, with 294 mm × 200 mm × 8 mm × 12 mm cross sections and a total height of 6.5 m (Fig. 5c), and a bolted connection with the top flange of the outer girders of the seven parallel steel girders at the third segment (Fig. 5d); (3) assembly of the first segment of the five parallel GFRP girders (Fig. 5e) and then connection to the third segment of the weight balance structural module (Fig. 5f); (4) assembly of the second segment of the five parallel GFRP girders by using the same sequence as the previous step (Fig. 5g) and then connection to the first segment of the crossing structural module (Fig. 5h); and (5) assembly of the third to final segment of the five parallel GFRP girders by using the same procedure as the previous step (Fig. 5i) and completion of the construction sequence to cross the river (Fig. 5j). The test results show that the 20 m span temporary composite bridge for emergency disaster relief was constructed by 30 workers within 6 hours via manpower, simple tools, and a small truck with a crane – ultimately meeting the requirements for emergency disaster relief.

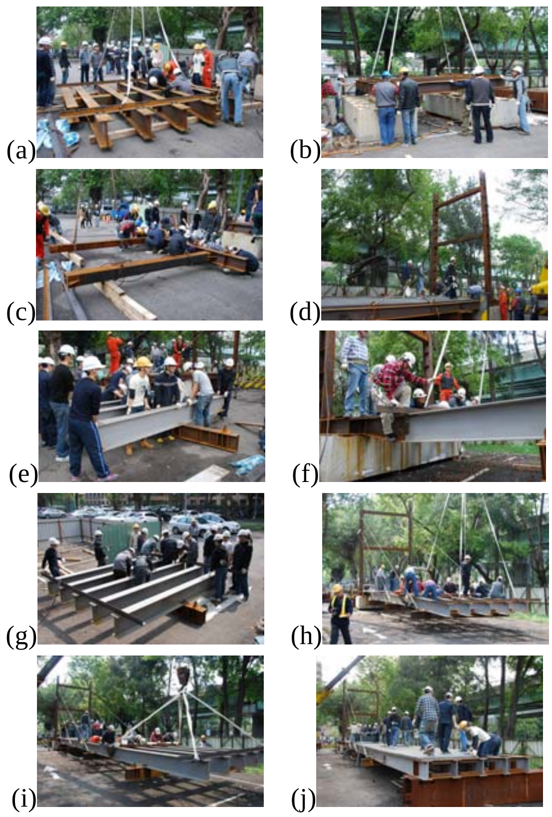

Fig. 5 Construction sequence of the 20 m span temporary composite bridge: (a) seven parallel steel girders assembly, (b) connection of the weight

balance structural module, (c) the H-shape pillars assembly, (d) connection of the bridge tower structural module, (e) first segment of the GFRP girders assembly, (f) connection of the crossing structural module, (g) second segment of the GFRP girders assembly, (h) and (i) connection of the crossing structural module, and (j) completion of the composite bridge construction

In Situ Full Scale Flexural and Dynamic Tests

The experimental setup of a temporary composite bridge with a span of 20 m is shown in Fig. 6a and the different loading positions of a small truck weighing 3.5 tons (total weight 5 tons) is shown in Fig. 6b. The test program includes a flexural test, an off-axis flexural test, and a dynamic test. The results of the flexural and dynamic tests are shown in Fig. 7. The deformed shapes are shown in Fig. 7a and Fig. 7b. The maximum displacements are 53.41 mm (flexural test) and 56.23 mm (off-axis flexural test) and occurred at connection G4. The maximum longitudinal strains are 5.05×10^{-4} (flexural test) and -5.53×10^{-4} (off-axis flexural test) and occurred on B3 at the left hand side of connection G4 (Fig. 7c). The deflection versus time at connection G4 is shown in Fig. 7d. The flexural and dynamic test results indicate that the deflection-to-span ratio is around L/356, which is very close to the design requirement of L/400, for a live load of 5 tons.

(a)

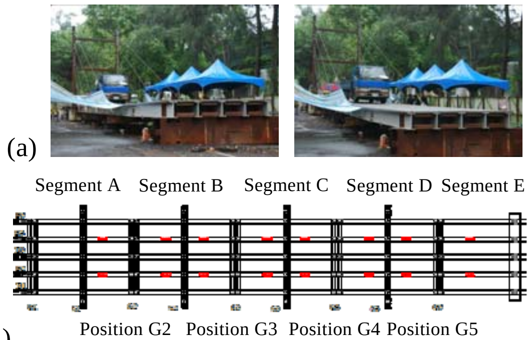

(b)

Fig. 6 The experimental setup of the 20 m span temporary composite bridge: (a) the test setup and (b) the wheel position of a small truck

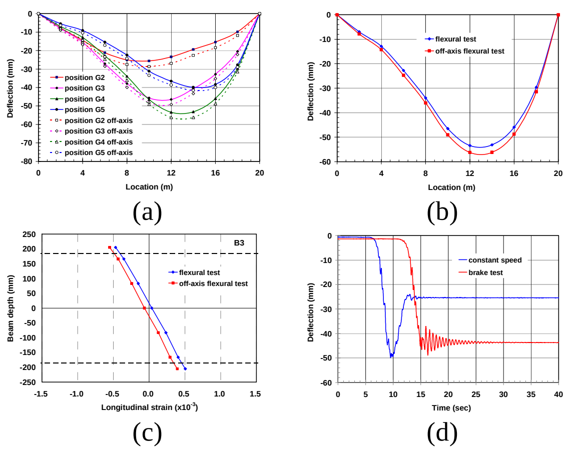

Fig. 7 Flexural and dynamic test results of the 20 m span temporary composite bridge: (a) the deformed shape (different loading position), (b) the deformed shape (loading at position G4), (c) the longitudinal strain along the depth of the B3 girder, and (d) deflection versus time at connection G4

Concluding remarks

This paper developed a lightweight, portable, and reusable temporary composite bridge for emergency disaster relief. This bridge is an asymmetric self-anchored cable-stayed bridge designed using steel-FRP composite materials to improve the stiffness of the composite frame, reduce the deflection of the bridge, and allow easy travel across a river without any supports or foundations. This allows us to reach the goal of disaster relief through the use of the concept of weight balance and the incremental launching method. The current research results are summarized as follows: (1) for bolted connections of the GFRP girder, the longitudinal pitch and transverse pitch should be greater than or equal to four times the bolt diameter (4d) for the web and the flange of the girder; (2) for the flexural test of the GFRP bridge with a span of 10 m, the deflection-to-span ratio is around L/376, which is very close to the design requirement of L/400, under a live load of 5 tons; (3) for the fatigue test of the GFRP bridge with a span of 10 m, there is no stiffness degradation over 2×10^5 cycles of loading with amplitude of target design loading 50 kN; (4) for the strength test the GFRP bridge with a span of 10 m, the design of the proposed composite bridge is deflection-driven, instead of being strength-driven, and the strength is higher than is required for a safety factor of more than 4; (5) for the in situ test of a 20 m temporary composite bridge for emergency disaster relief, the novel bridge was constructed by 30 workers within 6 hours through the use of manpower, simple tools, and a small truck with a crane to meet the requirements of emergency disaster relief. The flexural and dynamic test results indicate that the deflection-to-span ratio is around L/356, which is very close to the design requirement of L/400, for a live load of 5 tons.

References

Cheng L, Karbhari VM. "New bridge systems using FRP composites and concrete: a state-of-the-art review", *Progress in Structural Engineering Materials*, Vol. 8, No. 4, pp 143-154, 2006.

Hollaway LC. "The evolution of and the way forward for advanced polymer composite in the civil Infrastructure", *Proceedings of the International Conference on FRP Composites in Civil Engineering*, Hong Kong, Elsevier Science Ltd., pp. 27-40, 2001.

Study on the Methodology for Reliability-based Bridge Design Considering the Equivalent Scour Load

Chun-Chung Chen[1], Kuo-Chun Chang[2], Chi-Ying Lin[3], Chih-Hao Chen[4]

陳俊仲[1]、張國鎮[2]、林其穎[3]、陳志豪[4]

Abstract

Owing to the frequent occurrence of worldwide hydraulic hazards, scour has become the major cause of failure for cross-water bridges in many countries. Currently, the effect of scouring on bridges is not considered as an external loading; as a result, current bridge design codes are merely used to verify the stability of structures with specific scour exposure conditions. In order to design bridges while considering the scour effect, along with external and other loadings of hazardous events, developing a load model to represent the change of structural characteristics under different scour conditions is required. This study introduces a methodology that applies an innovative idea which conceptually transforms the reduction of capacity of a bridge due to the effects of scouring into an equivalent scour load which can be used as a demand load for structural design. A series of lateral loading tests of a pile model were conducted to revise the equivalent scour load formula in the literature. The proposed formula was used to establish a load model that considers the lateral failure mode and calculates the failure probability by applying conditional failure probability and introducing an acceptable failure condition factor. The experimental results are employed to construct the parametric scour fragility curves through the application of equivalent scour load formulae. The scour depths observed from the flume experiments are used to develop a scour fragility curve that can be applied to evaluate the vulnerabilities to scouring of piled bridge piers in preliminary studies. This study presents a feasible methodology for constructing a scour fragility curve from flume experiments.

Keywords: Bridge scour, equivalent scour load, fragility curve

Introduction

There are more than 28,000 bridges in Taiwan and scour is a growing threat to bridge structures due to the distinctive topography and the subtropical climate features of Taiwan. Due to frequent natural disasters (e.g., earthquakes, typhoons, and rainstorms), numerous scour problems (e.g., general scour and local scour) have caused the collapse of some of these bridges in recent decades. Such accidents have caused severe economic loss and have resulted in the deaths of many people. For instance, in 2008, Typhoon Sinlaku's debris flows broke down Hou-Fon Bridge and swept away three cars, killing six people. In 2009 during Typhoon Morakot, Shuang-Yuan Bridge toppled when four cars drove across it, consequently causing those cars to fall into the river. At present, the bridge design codes (Nowak, 1995 and AASHTO, 2012) generally consider scour and other regular load effects separately; thus, the design load combinations for bridges do not involve the scour load effect. Instead, bridge design takes a reduction of boundary conditions due to an assumed or expected scour depth. In order to design bridges with scour and expected external or other hazardous event loadings, Liang and Lee (2013a, b) and Liang (2013) proposed an innovative approach for converting resistance reduction into an equivalent scour load effect and also offered preliminary models of different failure modes

[1] Associate Researcher, National center for Research on Earthquake Engineering, jingochen@narlabs.org.tw
[2] Director, National Center for Research on Earthquake Engineering, kcchang@ncree.org.tw
[3] Research Assistant, Department of Civil Engineering, National Taiwan University, R98521219@ntu.edu.tw
[4] Graduate Student, Department of Civil Engineering, National Taiwan University, R01521210@ntu.edu.tw

for a scoured pier.

An equivalent scour load formula is required in order to transform the scouring effect that reduces the sediment resistance around the foundation into an equivalent load; the scouring effect can then be combined with any other load effect. This study modifies the equivalent scour load model through lateral loading tests of a pile model, and primarily focuses on the inclination failure mode. To test the validity of the proposed approaches and to understand how the scour depth affects bridge pier stability, the lateral bearing capacity of the pile foundation was investigated. The test results were compared via an educational software analysis with the utilization of the revised equivalent scour load. Consequently, the revised equivalent scour load model of the inclination failure mode was developed.

Furthermore, for combining the equivalent scour load into the reliability-based design procedure, this study applies the equivalent scour load model in evaluating scour failure probability and constructing scour fragility curves. The conditional failure probability approach was applied and an acceptable failure probability factor related to the allowable damage condition was introduced in order to calculate the failure probability. The scour fragility curves can be constructed by utilizing the observed data from field bridges or laboratory flume test results. The proposed preliminary methodology focuses on the lateral inclination failure mode of the pile foundation bridge. Other foundation types and failure modes should be included in future research. Although a complicated scale effect still exists, the failure probability calculated with an equivalent scour load can be used as a reference to indicate the safety and stability of a bridge pier.

Equivalent Scour Load and Lateral Capacity Test

Liang and Lee (2008) proposed that multi-hazard must be integrated into the Load and Resistance Factor Design (LRFD). Design procedures for extreme and time-dependent load effects, such as earthquakes, scour, and truck loads, are established separately. The major concern in this study is scour, for which Liang and Lee have provided an applicable approach that considers the scour effect as an equivalent load effect. The effect of resistance reduction is converted into an equivalent load effect, and the scour phenomenon can then be combined with other load effects and considered in the design procedure. Liang and Lee (2013a, b) have constructed an equivalent scour load model based on the direct approach for the settlement failure mode. However, the indirect approach is used to build an equivalent scour load model for the instability failure mode. Thus, comparison studies of equivalent scour load derivations using both direct and indirect approaches for inclination failure modes were conducted in this study. Therefore, single pile bearing capacity experiments were conducted to verify the proposed method for the inclination failure mode serving as a preliminary study case, and 11 lateral load and displacement curves were obtained. The results of a single pile lateral capacity test are shown in Fig. 1

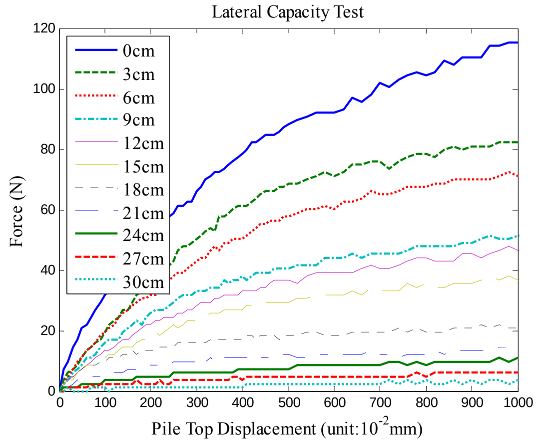

Fig. 1. Lateral capacity test results

The pile top lateral displacement was chosen as the conspicuous failure criterion; consequently, the relationship between the normalized scour depth or scour depth ratio (SDR), DS/H0, and the resistance reductions corresponding to five determined pile top lateral displacements are shown in Fig. 2.

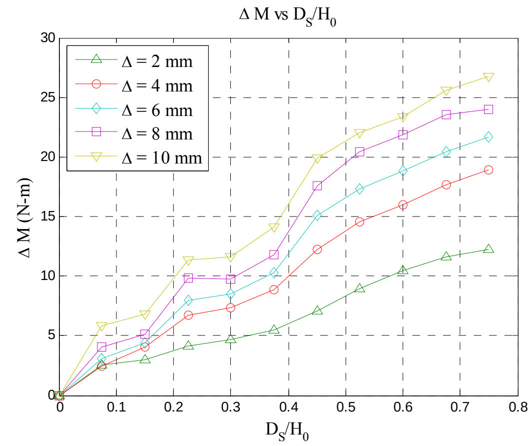

Fig. 2. Capacity reduction from test results

This study revises the equivalent scour load model of the direct method according to the results of the experiments and compares the revised value of the equivalent scour load with analysis results by using LPILE. The program computes deflection, bending moment, shear force, and soil response over the length of a pile. One of the reasons that the proposed load model overestimates the equivalent scour load, which is in fact the reduction of structural resistance, is overestimation of the equivalent stiffness of soil by the model. Furthermore, the simplified model proposed in the preliminary study may not clearly depict the complex condition for a scoured pier. From the results in the static pushover analysis using LPILE, the rotation point on the pile is located at the lower range of the pile length varying with scour depth instead of being located at the bottom, and does not conform to the assumption of the derivation. A parameter analysis is then conducted to investigate the influence of ξ on the calculated results. The result shows that a fixed ξ equal to 0.25 can acceptably match the analysis result of using a consecutive ξ varying with scour depth. Furthermore, compared to the pile top displacement, the degree of inclination is more widely used as a damage index in practical designs. As a result, the pile top displacement Δ is replaced with the production of total height H and the inclination on the top of the pile θ in the revised derivation. Hence, the revised equivalent scour load model or formula can be expressed as

$$S = \frac{n_h \Delta}{8}\left[\frac{H_0^{\,4}}{4H - H_0} - \frac{\left(H_0 - D_S\right)^4}{4H - \left(H_0 - D_S\right)}\right] \tag{1}$$

$$R = \frac{n_h \Delta}{8}\left[\frac{H_0^{\,4}}{4H - H_0}\right] \tag{2}$$

Failure Probability Calculation

A modified approach to calculate the failure probability and the corresponding limited state equation is established. A factor *k* is introduced and defined as an acceptable failure probability factor between 0 and 1, indicating that failure should occur before the equivalent resistance is exhausted. Furthermore, the factor *k* sets an acceptable failure criterion. A large *k* implies that the equivalent resistance can be utilized up to a higher portion. Therefore, a large *k* corresponds to a lower failure probability and a more severe failure condition, i.e., a greater pile top inclination state. The relationship between the acceptable failure probability factor *k* and pile top inclination angle θ corresponding to a failure criterion can be determined by examining the laboratory experimental data or collecting the damage data of real bridge structures. Then the conditional failure probability approach is used to calculate the failure probability

$$\begin{aligned} P_f &= \int_0^\infty p_f\left(x\right)dx \\ &= \int_0^\infty f_{n_h}\left(x\right)\left\{1 - F_S\left[kR\left(x\right)\right]\right\}dx \end{aligned} \tag{3}$$

The failure probability of different scour depths can be calculated by substituting parameters into the probability distribution function of S and R in Eq. 3. The parameters of the probability distribution function can be determined by using experimental results or collecting field data of bridge structures. The relationship between acceptable failure probability factor k and allowable pile top inclination angle θ corresponding to a specific failure criterion should be established first by investigating the laboratory experimental results. A large *k* indicates that a large portion of the equivalent resistance is provided to resist the lateral displacement. This will result in a lower failure probability but a more severe damage state, and a larger pile top inclination angle; therefore, the terms k and θ are positively correlated. The methodology to construct scour fragility curves must be verified with data either from the results of laboratory experiments or from observed data from bridges in the field. Since it is somewhat difficult to obtain satisfactory field data for bridge structures, this study focuses on constructing scour fragility curves using experiment results. Following the proposed flow chart of this study and the experimental scour fragility curves, the iteration could be begin with the COV_{DS} (*i.e.*, the coefficient of variation of the scour depth) equaling 0.3 (Ghosn *et al*., 2003) and then minimizing the objective function. The acceptable failure probability factors *k* (*i.e.*, *k* factor) corresponding to major, moderate, and minor damage are found in each iteration, and *R*-squared values calculated through the parametric curves constructed with the *k* factors and the experimental scour fragility curves are required to be higher than 0.99. If the *R*-squared results are not satisfied with the requirement, then the next iteration begins with the *k* factor calculated from the previous step and finds a COV_{DS} to further minimize the objective function and to check its *R*-squared values.

An inclination of 0.002 rad is used as the strictest allowable pile inclination in this study and 0.0089 rad, the maximum inclination state obtained from experiments, is used to construct the experimental scour curves. The corresponding *k* factor of the allowable inclination can be obtained by establishing the relationship between the *k* factor and the allowable pile top inclination θ through the experimental scour fragility curves. The major failure criteria are set from 0.002 to 0.008 and 0.0089, so a total of eight sets of failure criteria can be used to construct the relationship between *k* and θ. Each major failure criterion has one-third and two-thirds of its value corresponding to moderate and minor failure, and therefore 24 sets of failure criteria referring to different *k* factors can be found, and a nearly linear relationship between *k* and θ can be built and drawn in Fig. 3. Parametric scour fragility curves can be developed with a flexibly defined allowable inclination angle or acceptable failure criterion. In order to construct a scour fragility curve that can be more easily adopted for a real bridge pier, the allowable inclination of the pier is defined as 0.02 rad according to the bridge code used in Taiwan. Figure 4 shows the scour fragility curves for a major failure criterion equaling 0.02 rad and one-third and two-thirds of 0.02 rad corresponding to moderate and minor failure criteria.

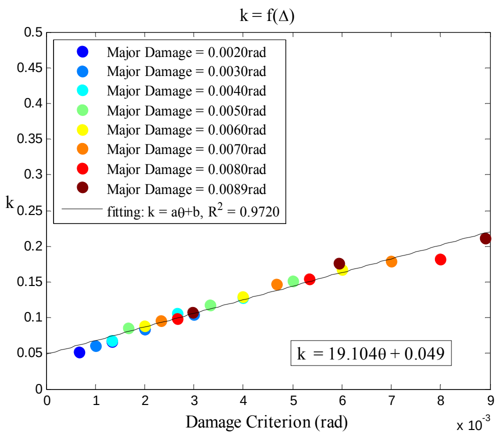

Fig. 3. Relationship between k factor and allowable pile top inclination θ

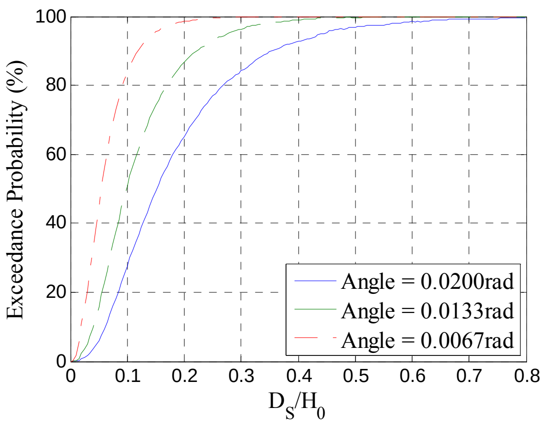

Fig. 4. Plots of scour fragility curves (major failure criterion: 0.02 rad)

Discussion and Summary

In this paper, a formula which was used to establish a load model that considered the inclination failure mode was proposed and the failure probability was calculated by applying conditional failure probability and introducing an acceptable failure condition factor. Consequently, the scour fragility curves related to a specific failure condition could be constructed, and the proposed methodology was verified with experimental results.

A methodology was proposed to construct the scour fragility curves of bridges with pile foundations by transferring the scour depth to the equivalent scour load and evaluating the failure probability with the limit state equation of the equivalent scour load and the equivalent resistance under certain scour depths. By using a series of experimental single-pile bridge lateral loading tests, the relationship between the reduction of resistance of the bridge pier and the corresponding scour depth was obtained. Consequently, the revised equivalent scour load model was established by examining the test results. The revised equivalent scour load model was also used for comparison with the test results in the analysis. Moreover, with the lateral loading tests, the revised equivalent scour load formula that could be used for the estimation of bridge failure probability was proposed.

An important factor that directly influences the safety of a bridge pier is the scour depth. This study presents observations on the relationship between scour depth and bridge pier inclination to better understand how increases in scour depth affect the lateral bearing capacity of the foundation. The behavior of the scour depth ratio of the pile versus time and the behavior of the inclination versus time were observed and recorded through the flume experiments. By establishing the relationship between the *k* factor and allowable pile top inclination θ, scour fragility curves could be constructed for each definable failure criterion. The corresponding parametric scour fragility curves can also be constructed to be fitted with any failure criterion. Once the scour depth is measured by a monitoring system or predicted by the scour depth formula, the failure probability of the bridge pier can be estimated and can serve as a warning index.

This research used a two-dimensional model to formulate the equivalent scour load formula. Further studies should be conducted by using a three-dimensional model for more accurate results. In addition, for simplicity, this study only discussed the equivalent scour load of a single pile foundation due to the instability failure mechanism. Other foundation types, compound failure mechanisms, and scale effects should be examined in future research by collecting more experimental results and field data. Further studies focusing on diverse soil and flow conditions and different failure modes are necessary in order to establish a more precise and generalized approach to form practical fragility curves that can be applied in diverse situations.

Reference

American Association of State Highway and Transportation Officials. (2010) “AASHTO LRFD Bridge Design Specifications, Fifth Edition”

Liang, Z., Lee, C. G. (2013), Bridge pier failure probabilities under combined hazard effects of scour, truck and earthquake. Part I: occurrence probabilities, Earthquake Engineering and Engineering Vibration, Volume 12, Issue 2, pp 229-240

Liang, Z., Lee, C. G. (2013), Bridge pier failure probabilities under combined hazard effects of scour, truck and earthquake. Part II: failure probabilities, Earthquake Engineering and Engineering Vibration, Volume 12, Issue 2, pp 241-250

Ghosn, M., F. Moses, & Wang, J. “NCHRP Report 489: Design of Highway Bridges for Extreme Events” Transportation Research Board, 2003.

Life-cycle Based Management System for Inspection and Evaluation of Bridges

Chia-Chuan Hsu [1], Chun-Chung Chen[2], Hsiao-Hui Hung [3], Kuang-Yen Liu[4]

許家銓 [1] 陳俊仲 [2] 洪曉慧 [3] 劉光晏 [4]

Abstract

The rising number of natural disasters has been a major threat to worldwide infrastructures. Civil engineers nowadays have to enhance the mitigation of hazards by increasing the service period of structures. The application of life-cycle of structures is a novel idea that was invented to assist engineers in planning, designing, building, and comprehensively maintaining a longer service life for structures. In this study, a life-cycle based bridge management system for disaster prevention is developed to improve the efficiency and the quality of bridge inspection work, evaluate the capacity of bridge disaster resilience and to ameliorate the accuracy of bridge information. The proposed system consists of distinguishing the evaluation functions for bridge resistance to earthquakes, floods, service loads, and deteriorations. This is achieved by collecting field inspection data and taking the planning and design information of existing bridges into consideration. The time-variant curves of the structural resistance of bridges to hazards during service time were built by applying expert system technologies to construct evaluation algorithms for bridge management, accompanied by strategies for the prevention of disasters. Moreover, modular aid tools and the mobile portable system were also developed and tailored to field inspection works. Effective strategies and practical methods were studied in this paper as well. The proposed system provides the functions to successfully evaluate the trend of changes in structural resistance required by the bridge authorities and engineers for bridge management and disaster prevention. The next and most important stage of this work is to put the system into use; the results from such implementation can provide practical feedback to further improve the system.

Keywords: BMS, Life-cycle

Bridge Management System

Due to the rising number of various disasters that has increasingly posed a threat to worldwide infrastructures, engineers and researchers put more and more effort into improving the knowledge of disaster prevention work in order to mitigate hazards via increasing the service period of structures. The effective bridge management system (BMS) can help authorities draw up productive strategies to maintain, enhance, and ensure the serviceability of bridges. Consequently, it is necessary to develop a BMS which is practical and useful for disaster prevention. This paper presents the present stage of this study and proposes a framework for life-cycle based BMS that should be capable of providing practical information and useful recommendations to assist authorities in managing bridge structures and mitigating disasters.

The purpose of this study is to develop a life-cycle based BMS that can improve the efficiency and the quality of bridge inspection work, to evaluate the capacity of bridge disaster resilience, and to ameliorate the accuracy of bridge information. The

[1] Assistant Researcher, National Center for Research on Earthquake Engineering, chiachuan@ncree.narl.org.tw.
[2] Associate Researcher, National Center for Research on Earthquake Engineering, ccchen@ncree.narl.org.tw.
[3] Research Fellow, National Center for Research on Earthquake Engineering, hhung@ncree.narl.org.tw.
[4] Associate Researcher, National Center for Research on Earthquake Engineering, kyliu@ncree.narl.org.tw.

application of the life-cycle of structures is a novel idea that was invented to assist engineers in planning, designing, building, and comprehensively maintaining a longer service life for structures.

BMS For Inspection And Evaluation Work

Field inspection is the basic task of bridge management for evaluating the condition of bridges. The authority of bridges have come to know that in order to make correct management decisions, proper predictive models have to be developed based on accurate data collected from field bridges. Consequently, the efficiency of the management work is heavily dependent on bridge inspectors recording detailed information for all of the structural elements and to evaluate bridge condition based on that record. Engineers and authority of bridges can benefit from up-to-date information on the capabilities of the most advanced bridge inspection technologies that are used to record detailed and accurate structural conditions and to provide useful references for evaluation work. However, this will generally require a lot of effort to gather such detailed information and therefore will not be feasible as a regular inspection protocol for field bridges. As a result, undertaking a full and accurate inspection on field bridges is a challenge as engineers are faced with the dilemma of choosing how to spend their limited time; engineers are forced to choose between spending less effort on field work or acquiring more structural information for evaluation in order to provide representative or significant results for disaster prevention.

The visual inspection of field bridges generally includes two types of information: general information and bridge components rating information. Bridge inspectors have to collect the general information such as the bridge name, bridge location, date of inspection, design code used, load classification, date built, structural sections, structural length, number of spans, inspection records, and bridge structural descriptions. The bridge components rating information includes traffic safety features, bridge deck conditions, load bearing components, abutments, piers/bents or pile bents, superstructure, substructure, channel and channel protection, and the approach. The purpose of BMS is to manage information about bridges and to assure their long-term serviceability for public use under the budgetary constraints of the owners. An inspection database is the core part of a BMS, which is built up of records obtained from maintenance activities.

Figure 1 shows elements of bridge inspection modules and Figure 2 presents the tree structure of inspection items that have to comply with inspection codes and are verified by experienced engineers. On the other hand, the main purpose of bridge inspection work is to support the bridge management system in identifying the needs of bridges for repairs, maintenance, preservation, reconstruction and replacement. The engineers or owners of bridges need such information to respond to critical deficiencies warranting immediate attention and for the long-term management of these critical infrastructure assets to assure both public safety and proper performance.

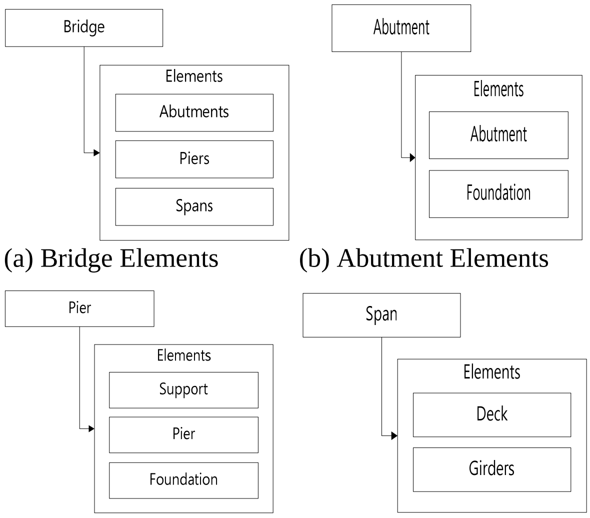

(a) Bridge Elements (b) Abutment Elements

(c) Pier Elements (d) Span Elements

Figure 1. Elements of Bridge Inspection Modules

Inspection items have to be filtered in order to differentiate which items or parts of items are related to structural safety and performance. However, using inspection records to evaluate the condition of field bridges sometimes involves subjective judgments. The various methodologies used to evaluate the structural condition usually lead to varying evaluation results. Rating the performance of each structural component from the field by referencing against each structural component in the records requires professional and engineering empirical knowledge; the main challenge will therefore be on the mapping relationship between local component information and global structural conditions. Each structural component should have a different contribution to the performance of the structure, which means the weighting for each inspected data of each component is different in the overall evaluation result. The interaction effects between each component and the deterioration model of each component have to be also considered appropriately. Therefore, a comprehensive evaluation procedure needs to be the strong foundation for BMS; the evaluation method should enhance and complete the BMS. In Taiwan, there are more than 25,000 existing bridges and many of them stride across the river. Many bridges are reaching the oldest stage of their designed service life. While earthquakes and floods are two of the major types of disasters that can result in damage to or failure of bridge structures, long-term considerations like the deterioration of structural elements and events of immediate disservice might cease the effective function of bridges more frequently. The BMS should actually put such thoughts into the management philosophy and try to provide more reliable and concrete strategies to the owners and authorities for disaster prevention of bridge structures.

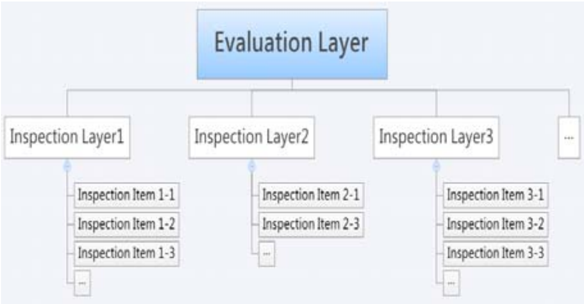

Figure 2. Illustration of the tree Structure of BMS

Developing System

The BMS developed in this study includes three main parts with complimentary functionalities. The first part is the modularization function. Figure 3 shows the concept of the National Center for Research on Earthquake Engineering (NCREE) life-cycle based bridge management system (NCREE-LCB-BMS) service bus that has been developed. By adopting the idea of Web 2.0 and Web 3.0, the NCREE-LC-BMS will satisfy the service-oriented architecture design and provide a full web service application program interface in the information layer of the system. The service bus will flexibly connect the NCREE-LCB-BMS with other application functions for extended modules use. NCREE-LCB-BMS integrates the distinguishing evaluation functions for the bridge resistance to earthquakes, floods, service loads, and deteriorations. For this reason, the design of NCREE-LCB-BMS and other systems with extended functions is more flexible. The designed systems can be either connected together or operated separately to get the independence of maintenance among the systems and, if needed, reduce the cost of modification of systems.

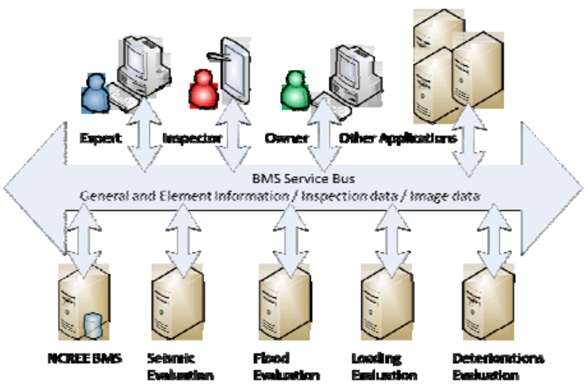

Figure 3. Concept of service bus of NCREE-LCB-BMS

The second functional part of NCREE-BMS is the information database which will store with bridge inspection data. The principle of design of this part is the customization functions. Figure 4 displays the guiding policy of NCREE-BMS. And the system design frame of this part is called MVC standing for Model, View and Controller (Figure 5). The Microsoft ASP.NET MVC design frame can reduce the component coupling between each part of components in the system and raise system capability on extension flexibility. The tools used for the data processing are MySQL Database and CouchDB, which are able to substantiate the table-column object in the database with flexibility.

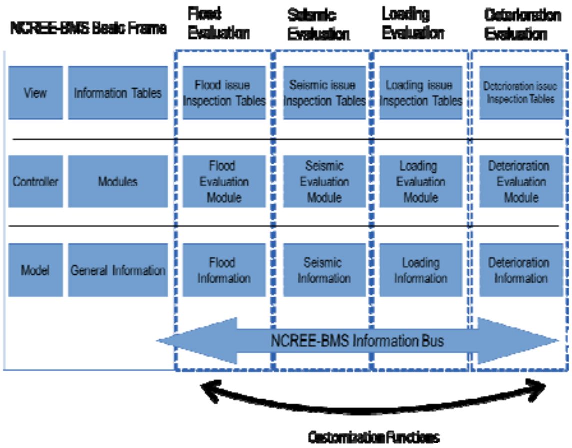

Figure 4. Customization Functions of NCREE-LCB-BMS

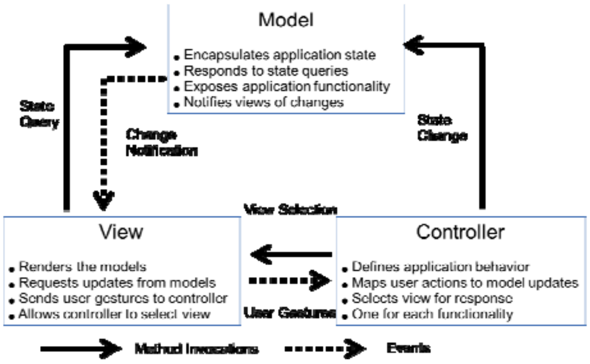

Figure 5. MVC design frame for NCREE-LCB-BMS

The third functional part of the NCREE-LCB-BMS is the module that will apply expert system algorithms to evaluate and rate the condition of structures. This part will accomplish the design and implementation of the visual interface interacting with expert knowledge, the integration engine of expert algorithms, the analysis core of a Neural-aided expert system, the graphic user interface of the expert system operation, and the management of the database for bridge inspection data and principles.

To sum up, the structural evaluation of bridge deterioration needs the knowledge of experts. However, adequately training and educating experts requires a lot of time and resources. As for the large amount of data from bridge inspection work, an expert system that can simulate thinking algorithms to the caliber of experts is needed to help engineers or owners to evaluate the condition of a bridge before a disaster occurs. In general, the algorithms embedded in the BMS have to be reviewed and modified according to the feedback information from field observations of bridges. NCREE-LCB-BMS will integrate extendable and modifiable modules to put the developed system into practical use. Overall, the operation layout of developing NCREE-LCB-BMS is outlined in Figure 6.

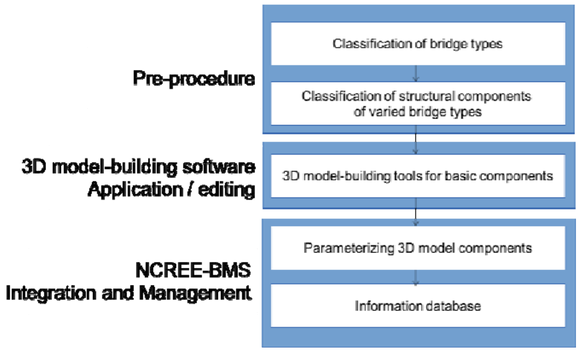

Figure 6. Operation layout of NCREE-LCB-BMS

Summary

In this paper, the developing framework of a life-cycle based bridge management system for bridge inspection and evaluation is introduced. The NCREE-LCB-BMS system is expected to be employed to improve the efficiency and the quality of bridge inspection work, to evaluate the capacity of bridge disaster resilience, and to ameliorate the accuracy of bridge information. Thus, the system under development will provide the functions to evaluate the trend of changes in structural resistance required by the bridge authorities and engineers for bridge management and disaster prevention. The next and most important stage of this work is to put the system into use, which can then provide practical feedback for further improvement of the system.

References

Mirzaei, Z., Adey, B.T., Klatter, L., Kong, J.S. 2012, The IABMAS Bridge Management Committee Overview of Existing Bridge Management Systems, IAMBAS 2012.

Ohio Department of Transportation 2010, Manual of Bridge Inspection, ORC 5501.47.

Paul D., Thompson, A New Bridge Management System for Ontario, Brian Kerr, ITX Stanley Ltd., Canada.

Reed M. Ellis, Pau D. Thompson, Rene Gagnon, Guy Richard, Design and Implementation of a New Bridge Management System for the Ministry of Transport of Quebec. Stantec Consulting Ltd.

Loading Test and Long-Term Monitoring on Wugu-Yangmei Viaduct of Taiwan National Highway

Zheng-Kuan Lee[1], Chun-Chung Chen[2], Hsiao-Hui Hung[3] and Yu-Chi Sung[4]

李政寬 [1] 陳俊仲 [2] 洪曉慧 [3] 宋裕祺 [4]

Abstract

Wugu-Yangmei Viaduct Bridge is the second widening project of Taiwan National Highway. The viaduct stretches from Wugu in the north to Yangmei in the south on the west coastal plain of the island, with the total length of 39 km. It was constructed from November 2009 to December 2012. Before the official opening to the public, the bridge owner, Taiwan Area National Expressway Engineering Bureau, entrusted NCREE with loading tests on the bridge. Besides, after the opening, the deflected shapes of three spans are long-term monitored by optic fiber sensors. This paper describes the mentioned loading tests and optical instruments application in the field.

Keywords: bridge loading test, optic fiber sensor, deflected shape measurement

Introduction

The Wugu-Yangmei Overpass (hereafter referred to as the Wuyang Overpass) is the second highway improvement on the Zhongshang Freeway following the Xizhi-Wugu Overpass (hereafter referred to as the Xiwu Overpass). The Wuyang Overpass is connected to the Xiwu Overpass at the north and the northern section of the Yangmei Toll Station at the south. The Wuyang Overpass measures 39 km in length, which comprises 6.3 km of embankment and cutting slopes and 31.7 km of elevated highway. The construction of this overpass was executed through numerous tenders. The objectives of this construction project were to relieve traffic bottlenecks between Taipei and Taoyuan, improve intercity transportation functions, and expand the service performance of the Xiwu Overpass. The construction of the Wuyang Overpass commenced in November 2009 and was completed in approximately 3 years. After construction was completed and prior to the launch, the Taiwan Area National Expressway Engineering Bureau (TABEEB) commissioned the National Center for Research on Earthquake Engineering (NCREE) to conduct a series of load tests on the overpass. The test results showed that girder deflection and design response values were similar and that deflection presented an elastic response with no residual reaction. The Wuyang Overpass became accessible to the public in April 2013 after a series of inspections. Succeeding the load tests, the TABEEB commissioned the NCREE to undertake a 2-year project to monitor three single-span bridge piers of the overpass. This study explained the process and results of relevant vehicle load tests performed during this project, long-term monitoring method used, and current observational progress.

Load Test Planning

Figure 1 illustrates C907 of the Freeway Improvement Project, which focuses on the construction of Luzhu and the airport system interchange sections in Taoyuan (of the Wugu to Yangmei section). The three single-span bridge piers on which vehicle load tests were performed comprised sections between Northbound Overpass Sections P19N and P20N (hereafter referred to as Section A), Southbound Overpass Sections P21S and P22S

[1] Associate Researcher, National Center for Research on Earthquake Engineering, zklee@ncree.narl.org.tw
[2] Associate Researcher, National Center for Research on Earthquake Engineering, jingochen@narlabs.org.tw
[3] Research Fellow, National Center for Research on Earthquake Engineering, hhung@ncree.narl.org.tw
[4] Professor, National Taipei University of Technology
and Division Head, National Center for Research on Earthquake Engineering, sungyc@ntut.edu.tw

(hereafter referred to as Section B), and Southbound Overpass Sections P31S and P32S (hereafter referred to as Section C). The TABEEB commissioned the NCREE to perform static vehicle load tests on the three single-span bridge piers to measure the deflection changes of the bridges at different loads and to collaborate with the design unit, CECI Engineering Consultants, Inc., in comparing the obtained deflection results with original designs to ensure that the bridges conform to design specification requirements.

According to the Standard Specifications for Highway Bridges, designers should initially adopt four-lane HS20-44 freeway live loads and consider numerous relevant regulations, such as 25% overloading, a 75% four-lane reduction factor, and impact factors, to determine the maximal design live load requirements for their bridge designs, which can then be converted into equivalent truck weights. For example, if each truck weighed approximately 20 tons, the required number of trucks for Sections A, B, and C for testing would be 16, 28, and 12, respectively. The test process was characterized into four steps: (1) no load, (2) half load, (3) full load, and (4) unloading. Figure 2 illustrates the testing process for Section A. The processes for the remaining two sections are similar to those shown in Fig. 2.

Figure 1. Load tests performed at three single-span sections

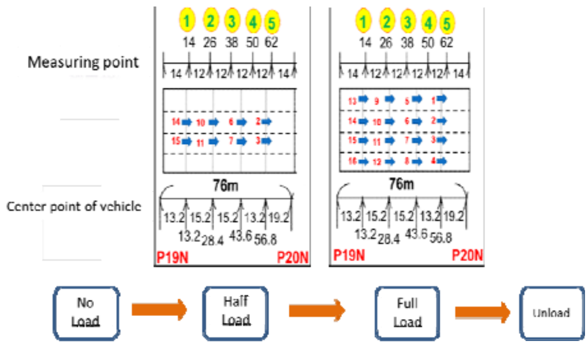

Figure 2. Testing process

Load Test Results and Discussion

The test parameters and structural analysis values of the various sections are listed in Table 1. The test conclusion is summarized as follows:

1. The test results for no load and full loads showed that the bridge structures demonstrated elastic responses.

2. The midpoint deflection results of the various sections were less than the upper structure restrictions according to the Standard Specifications for Highway Bridges, which stipulates that deflection should be less than 1/800 of the bridge span.

3. After unloading was performed, the midpoint deflection of Sections A and B returned to 0. However, a deflection remnant of 0.2 cm remained in Section 3, which may be attributed to bridge deformity caused by an excess number of vehicles, prolonged test times, and sunshine and temperature changes.

4. The tests results obtained at full loads revealed that the midpoint deflection values were relatively similar to the structural analysis values for all three sections, except for Section A, for which the test values were slightly higher than the analytical values. Therefore, Section A should be continually monitored.

Girder No.	P19N ~P20N	P21 ~P22S	P31 ~P32S
Girder Span	76m	136m	60m
Number of Half-Loaded Vehicles (20 tons)	8	14	6
Number of Fully Loaded Vehicles (20 tons)	16	28	12
Midpoint Deflection at Half Load	1.3 cm	2.2 cm	0.5 cm
Midpoint Deflection at Full Load	2.6 cm	4.4 cm	1.0 cm
Midpoint Design Deflection at Full Load*	2.3 cm	4.7 cm	1.1 cm
1/800 Span	9.5 cm	17.0 cm	7.5 cm
Midpoint Deflection After Unloading	0.0cm	0.2 cm 0.0 cm**	0.0 cm

*Numerical analysis results provided by CECI Engineering Consultants, Inc.
** Re-tested after 2 days

Development of a Long-Term Level-Monitoring Instrument

To verify the long-term deflection changes at the three sections, the TABEEB commissioned the NCREE to execute a follow-up monitoring project. Previous load tests were performed prior to public access. The conventional method of manually mapping and surveying levels was employed for measuring the deflection curve of the girders, as shown in Fig. 3. However, after public access was granted, conventional level-monitoring instruments could no longer be assembled on the bridge. Therefore, the current project involved installing optical fiber subsidence meters into the hollows of the girders to replace conventional manually operated methods and achieve long-term mapping and surveying operations. The following section discusses the concepts and applications of the optical fiber subsidence meter developed by the NCREE.

Figure 3. Load tests and level measurements performed on the Wuyang Overpass

Fiber Optic Sensing

Optical fibers apply the principle of total reflection to transmit light energy and signals. The optical fibers used for telecommunication are typically single-mode quartz fibers, which yield a light loss rate of approximately 0.2 dB/km and communication band of between 1520 to 1580 nm. Optical fibers are a transmission medium and do not have sensing functionality. However, such fibers can be exposed to artificial ultraviolet irradiation to form fiber Bragg gratings (FBG). FBGs are sensing components and thus have sensing functionality (Fig. 4).

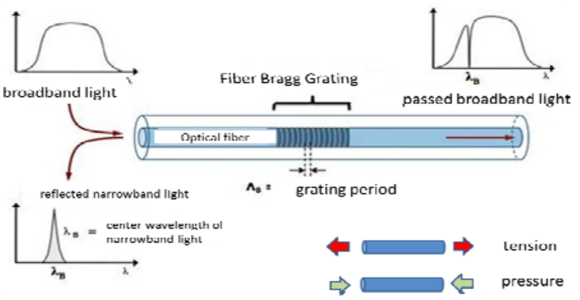

Figure 4. Fiber Bragg grating sensing component

Broadband light is introduced into one end of the optical fiber, the FBGs reflect specific narrowband light (determined by Grating Period Λ), and the "remaining" broadband light progresses through the fiber. When the FBGs experience tension, the grating periods widen, the center wavelength (λB) of the reflected narrowband light increases, and the spectrum shifts to the right. By contrast, when the FBGs experience pressure, the grating periods shorten, the center wavelength (λB) of the reflected narrowband light decreases, and the spectrum shifts to the left. In addition, the periods between the FBGs change according to the temperature. The material behavior of FBGs when influenced by force or temperature can be mathematically expressed as follows:

$$\frac{\Delta\lambda_B}{\lambda_B} = C_S \Delta\varepsilon + C_T \Delta T \tag{1}$$

where, λ_B represents the center wavelength of the reflected narrowband light, $\Delta\varepsilon$ represents the response of the gratings under stress, ΔT represents the amount of temperature change of the gratings, and CS and CT represent correlation coefficients. In theory, two FBGs should simultaneously be used for determining how $\Delta\varepsilon$ and ΔT influences $\Delta\lambda$. Of which one FBG must be influenced by only temperature (stress free) to eliminate the temperature effects of the other FBG. In practice, the effects of temperature can be rationally overlooked in construction applications if the level of influence of ΔT does not exceed the critical value of 10%; in other words, using one FBG instead of two FBGs to decrease construction burden.

The aforementioned discussion verifies that FBGs can essentially be considered as a type of sensing meter. Subsequently, FBGs can be fabricated into designated sensing instruments, such as displacement and subsidence meters, after mechanical processing. The key process method proposed in this study is to clamp the optical fiber with heat shrinkable sleeves, which are used as a connector for introducing external forces into the FBG (Fig. 5a). By using this connector, instrument components fabricated from local organizations can exert prestress, which serves as the sensing origin (Fig. 5b).

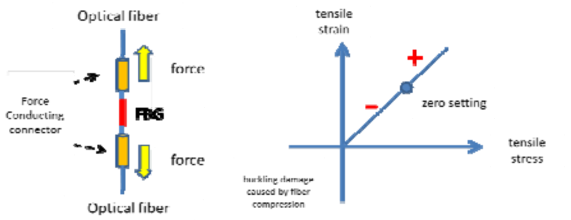

(a) (b)

Figure 5. Connector introducing external force

Optical Fiber Subsidence Meter

The optical fiber subsidence meter constitutes fiber Bragg gratings and floats, and its application is based on the communicating pipe principles, floating mechanics, and FBG elastic range (Hooke's law), as illustrated in Fig. 6. When bridge piers subside or rise, or when the midpoint deflection of the girders changes (relative change), the water within the pipes shift from a higher position to a lower position until the water surface elevation within the pipes are consistent. Therefore, changes in the buoyancy of the floats alter the tension exerted on the FBG, subsequently changing the light wavelength. The datalog was placed below the bridge pier (Fig. 7), and optical wires ran along the bridge columns and into the box girders, where they connected with a series of subsidence meters. These wires then remotely connect the subsidence meters in the other sections. Engineering staff were required to only analyze the light wavelength data under the bridge to determine the deflection conditions of the bridge girder. Conventional electronic sensing instruments lack the remote capabilities of optical fibers. Such electronic sensing instruments are limited by wiring distance, signal quality, and wiring costs, which indicate the benefits of optical fiber sensing instruments.

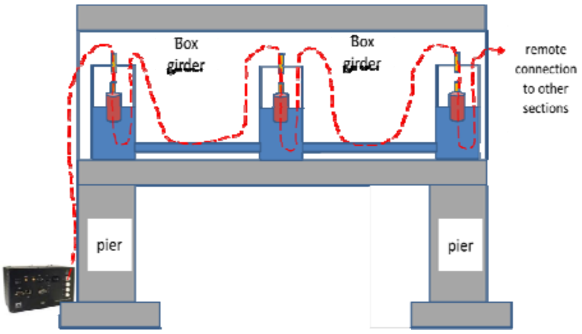

Figure 6. Layout of the optical fiber subsidence meters

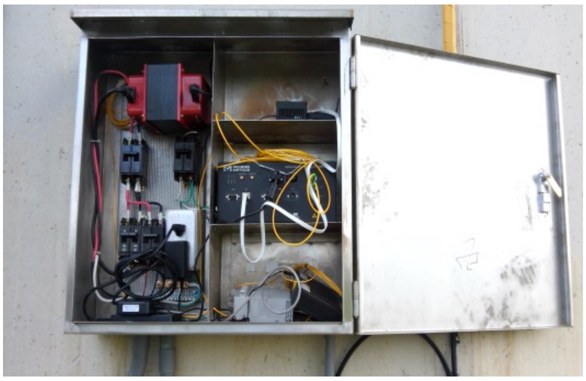

Figure 7. Observation station and measurement equipment under the bridge column

Laying the Optical Fiber Level-Monitoring Instrument on the Wuyang Overpass

Figure 8 illustrates the layout of the optical fiber subsidence meters. For Section A, 57 and 42 represent 1557 nm and 1542 nm, respectively. The two subsidence meters were linked using a connecting pipe. Subsequently, the exertion of prestress caused 1557 nm to present 1558 nm and 1542 nm to present 1543 nm. If the girder presented midpoint vertical deflection, then the FBG readings were estimated to indicate the values tabulated in Table 2. Figure 9 illustrates the midpoint vertical deflection observation data of the three sections within 24 h

.

Table 2. FBG Reading Descriptions

Initial State of Grating	Prestress Exertion on Subsidence Meter	Girder Presents a Midpoint Subsidence of 2 cm	Girder Presents a Midpoint Elevation of 2 cm
1557nm	1558nm	1558nm+0.4nm	1558nm-0.4nm
1542nm	1543nm	1543nm+0.4nm	1543nm-0.4nm

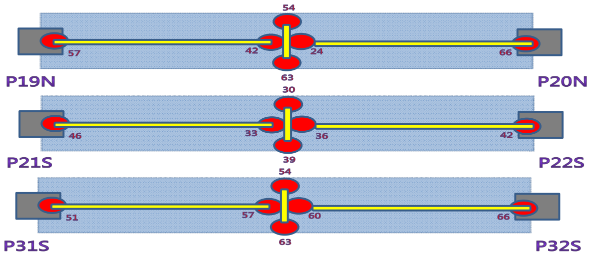

Figure 8. Layout of the optical fiber level-monitoring instrument on Wuyang Overpass (Top View)

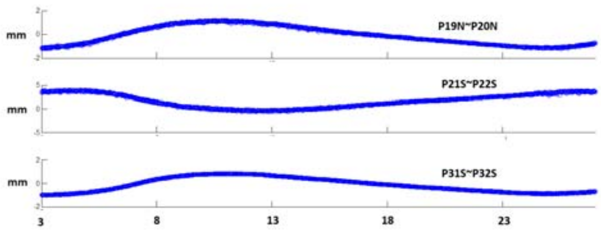

Figure 9. Midpoint vertical deflection observation data of the three sections within 24 h

Conclusion

This study performed a series of vehicle load tests and determined that the original design values were similar to the test values. In addition, this study developed an optical fiber subsidence meter, which was subsequently installed beneath the overpass to replace conventional manually operated mapping and surveying activities. The extended communications capability of optical fibers eliminated signal failure and compensation problems that may have occurred when using conventional electronic instruments to observe the girders of three overpass sections at different locations. The monitoring data obtained in this study were processed to establish initial values. This study anticipates using half-load reactions as the warning values for the 2-year monitoring project.

Mathematical Modeling and Experimental Validation for Hysteresis Behavior of High-Damping Rubber Bearings

Yin-Han Yang[1], Chia-Yi Shiau[2], Shiang-Jung Wang[3] and Jenn-Shin Hwang[4]

楊印涵[1]、汪向榮[2]、蕭佳益[3]、黃震興[4]

Abstract

High-damping rubber (HDR) bearings are a common isolator used in seismic isolation systems. Because of the complex rubber compound, the mechanical properties of HDR bearings are highly nonlinear, such that the existing bilinear analytical model may not be appropriate for describing their hysteresis behavior. A mathematical model regarding the shear force experienced by HDR bearings as a combination of the restoring force and damping force was developed in previous research to characterize the hysteresis behavior of HDR bearings. However, it was found that different load patterns or displacement and velocity responses of HDR bearings have a significant influence on the mathematical modeling of their hysteresis behavior. In this research, the proposed mathematical model is further investigated and modified on the basis of sinusoidal and triangular cyclic loading tests on HDR bearings. By comparing the analytical predictions to the experimental results, the accuracy of the model calibration is discussed.

Keywords: high-damping rubber bearing, hysteresis loop, mathematical model, experimental verification

Introduction

As shown in previous research, the hysteresis behavior of high-damping rubber (HDR) bearings may strongly depend on material compounding, vulcanization, excitation frequency, ambient temperature, experienced shear strain level, and axial load. These factors lead to the complexity of the shear force-displacement relationship of HDR bearings, which possess highly nonlinear, viscoelastic, viscoplastic, and thixotropic constitutive properties [1]. In current engineering practice, the simplified bilinear hysteresis model [2] is adopted as an expedient representation for seismic isolation design with HDR bearings; however, the bilinear approximation may not properly represent their actual behavior [3].

To more appropriately characterize the hysteresis behavior of HDR bearings, a mathematical model was proposed by Hwang *et al.* [4]. In this proposed mathematical model, the shear force experienced by HDR bearings was regarded as a combination of the restoring force and damping force. Furthermore, because of the Mullins and scragging effects [5][6] on the hysteresis behavior of HDR bearings, the concept of energy dissipation by elastomeric bearings during each cycle was introduced into the proposed mathematical model to incorporate the prediction capability of the cyclic softening and strain hardening behavior of HDR bearings at high shear strain levels. It was found that even if the hysteresis behavior of the HDR bearings under a sinusoidal wave loading was accurately captured by the proposed mathematical model, the proposed model was not applicable to describing the hysteresis behavior of HDR bearings subjected to a triangular wave loading. Hence, the proposed mathematical model is modified in this study and then verified through a series of sinusoidal and triangular cyclic loading tests on HDR bearings. The modification process and its accuracy are further discussed.

[1] Research Assistant, National Center for Research on Earthquake Engineering, yinhanyang@narlabs.org.tw
[2] Research Fellow, National Center for Research on Earthquake Engineering, sjwang@ncree.narl.org.tw
[3] Assistant Researcher, National Center for Research on Earthquake Engineering, cyshiau@ncree.narl.org.tw
[4] Division Director, National Center for Research on Earthquake Engineering, jshwang@ncree.narl.org.tw

Mathematical hysteresis model for HDR bearings

Hwang's mathematical hysteresis model proposed and an experimental study

In the mathematical hysteresis model proposed by Hwang *et al.* [4], the shear force experienced by an elastomeric bearing is characterized as:

$$F(x(t),\dot{x}(t)) = K(x(t),\dot{x}(t))x(t) + C(x(t),\dot{x}(t))\dot{x}(t) \quad (1)$$

where $x(t)$ and $\dot{x}(t)$ are, respectively, the relative displacement and relative velocity of the elastomeric bearing at time t. The stiffness and damping coefficient at time t are respectively given by

$$K(x(t),\dot{x}(t)) =$$

$$a_1 + a_2 x^2(t) + a_3 x^4(t) + \frac{a_4 e^{a_9 \int_0^t F(x(t),\dot{x}(t))dx(t)}}{\cosh^2(a_5 \dot{x}(t))} \quad (2)$$

and

$$C(x(t),\dot{x}(t)) =$$

$$\frac{a_6 + a_7 x^2(t)}{\sqrt{a_8^2 + \dot{x}^2(t)}}\left[1 + e^{a_{10} \int_0^t F(x(t),\dot{x}(t))dx(t)}\right] \quad (3)$$

where $a_1 \sim a_{10}$ are to-be-determined coefficients from cyclic loading reversals. As the cyclic softening behavior of HDR bearings can be regarded as a function of energy dissipation, the integral term $\int_0^t F(x(t),\dot{x}(t))dx(t)$, together with the to-be-determined coefficients, was applied to Eqs. (2) and (3) to respectively describe the degradation of stiffness and the variation of the hysteresis loop area.

In order to identify the to-be-determined coefficients, the quasi-static cyclic loading tests were conducted on scaled-down HDR bearings. A single test bearing comprising 25 HDR layers, each with a thickness of 1.97 mm and a diameter of 150 mm, was used. The tests were displacement-controlled, and the test shear strain level ranged from 50% up to 250% with an increment of 50%. Note that the test bearings were subjected to three full cyclic displacement reversals at each shear strain level.

Under an axial load of 130 kN, the experimental results under a triangular wave loading with a velocity of 24.63 mm/s, and a sinusoidal wave loading with a frequency of 0.125 Hz are demonstrated herein. Table 1 lists two sets of ten coefficients identified from the test results. A comparison of the experimental and analytical hysteresis loops is shown in Fig. 1. Obviously, the hysteresis behavior of the HDR bearings under a triangular wave loading may not be appropriately captured by the proposed mathematical model.

Table 1. Coefficient identification results: Hwang's model.

Test name	(a) Triangular	(b) Sinusoidal
a_1	0.024	0.072
a_2	-2.98e-08	-1.12e-07
a_3	5.90e-10	3.31e-10
a_4	0.177	0.101
a_5	0.024	0.022
a_6	4.476	5.757
a_7	2.59e-04	4.43e-04
a_8	15.28	54.34
a_9	-5.73e-05	-4.87e-05
a_{10}	-0.016	-0.003

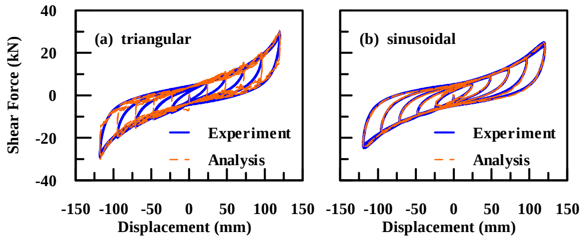

Figure 1. Comparison of hysteresis loops: Hwang's model

Discussion of Hwang's model

To further clarify the physical meaning of the mathematical model proposed by Hwang *et al.* [4], the components in the restoring force of Eq. 2 and the damping force of Eq. 3 are separately illustrated in Fig. 2. Note that the components of the restoring force are presented in Figs. 2(I) to 2(IV), whereas the components of the damping force are presented in Figs. 2(V) and 2(VI).

For the components of the restoring force, the x term is used to model the main stiffness skeleton of the hysteresis loops, the x^3 term is used to represent the variation of stiffness at high shear strain levels, and the x^5 term is used to characterize the strain hardening effect. The to-be-determined coefficients $a_1 \sim a_4$ are adopted as participation factors for each term in the stiffness. Cooperating with the to-be-determined coefficient a_5, the $x/\cosh^2(a_5\dot{x})$ term is used to take the effect of frequency on the HDR bearings into consideration. However, because the first-order derivation of a triangular displacement wave loading (*i.e.*, velocity) is a step function, the denominator of the $x/\cosh^2(a_5\dot{x})$ term turns out to be a constant and the term loses its contribution to the stiffness when triangular displacement wave loading is applied.

For the components of the damping force, the $a_6 + a_7 x^2$ term is used to adjust the damping force at high shear strain levels. The $\dot{x}/\sqrt{a_8^2 + \dot{x}^2}$ term is a damping model controlled by the to-be-determined coefficient a_8. As a_8^2 is sufficiently larger compared to $\dot{x}$, the $\dot{x}/\sqrt{a_8^2+\dot{x}^2}$ term becomes a viscous damping model. In contrast, as a_8^2 is sufficiently smaller compared to $\dot{x}$, the $\dot{x}/\sqrt{a_8^2+\dot{x}^2}$ term can be simplified as $\dot{x}/|\dot{x}|$, which is a friction-type damping model. Initially, this damping model $\dot{x}/\sqrt{a_8^2+\dot{x}^2}$ was developed based on an element subjected to an axial load, such as viscous dampers. For the element under the simple shear loading condition and subjected to triangular displacement wave loading, this damping model $\dot{x}/\sqrt{a_8^2+\dot{x}^2}$ fails to immediately capture the actual hysteresis behavior of the HDR bearings whenever the applied loading changes its direction.

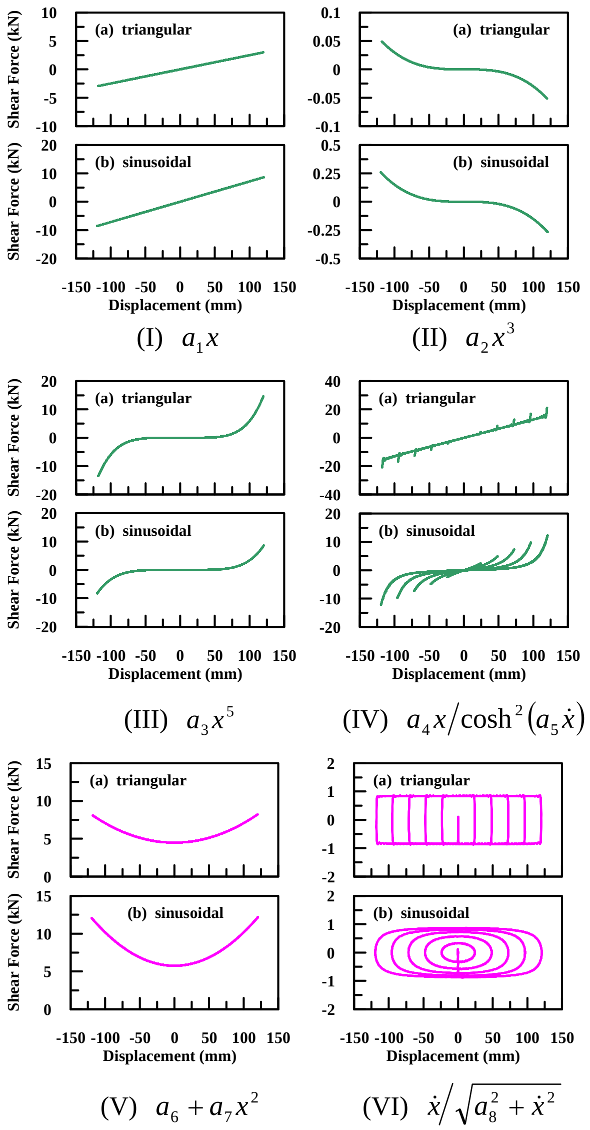

Figure 2. Components of Hwang's mathematical hysteresis model.

Modification of Hwang's model

To develop a suitable model for characterizing the hysteresis behavior of HDR bearings under either sinusoidal or triangular wave loadings, the mathematical hysteresis model proposed by Hwang *et al.* [4] was modified by incorporating the analysis model proposed by Abe *et al.* [7][8]. In Abe's model, the shear force experienced by the HDR bearings is regarded as a combination of a nonlinear elastic spring force, an elasto-plastic spring force, and a hardening spring force. Among these three spring force components, the elasto-plastic spring force, simplified from a rate-independent model proposed by Özdemir [9], was used to simulate the damping force of the HDR bearings. The mathematical representation of the elasto-plastic spring force at time t is given by:

$$\dot{F}_2(t)=\frac{Y_t}{x_t}\left[\dot{x}(t)-|\dot{x}(t)|\left|\frac{F_2(t)}{Y_t}\right|^n \operatorname{sgn}\left(\frac{F_2(t)}{Y_t}\right)\right] \tag{4}$$

where F_2 is the elasto-plastic spring force, n is the nonlinearity controlled parameter, and Y_t and x_t are the parameters used to adjust the damping force at high shear strain levels. These are represented by:

$$Y_t = Y_0\left(1+\left|\frac{x(t)}{x_H}\right|^p\right) \tag{5}$$

$$x_t = x_0\left(1+\frac{x_{\max}(t)}{x_S}\right) \tag{6}$$

where Y_0 is the initial yielding force parameter, x_0 is the initial yielding displacement parameter, x_H is the strain hardening displacement parameter, p is the strain hardening parameter, x_S is the yielding displacement parameter, $x_{\max}$ is the experienced maximum displacement response.

According to the detailed discussion of the mathematical hysteresis model proposed by Hwang *et al.* [4] in Section 2.2, the stiffness of a HDR bearing can be well characterized using the combination of terms x, x^3, and x^5, together with the to-be-determined coefficients. Hence, the stiffness in the modified mathematical model at time t is given by:

$$K(x(t),\dot{x}(t))=a_1+a_2x^2(t)+a_3x^4(t) \tag{7}$$

Furthermore, the elasto-plastic spring model in Abe's model [7][8] is adopted in the modified mathematical model to represent the damping force experienced by the HDR bearings. Note that the Y_t/x_t term in the elasto-plastic spring model is simplified by the $a_6+a_7x^2$ term because both terms are identical in their contribution to the damping force. Consequently, the modified mathematical hysteresis model can be demonstrated as follows:

$$F\left(x(t), \dot{x}(t)\right) = \left[a_1 + a_2 x^2(t) + a_3 x^4(t)\right] x(t) + F_2(t) \quad (8)$$

$$\dot{F}_2(t) = \left(a_4 + a_5 x^2\right)\left[\dot{x}(t) - \left|\dot{x}(t)\right| \left|\frac{F_2(t)}{Y_t}\right|^{a_6} \operatorname{sgn}\left(\frac{F_2(t)}{Y_t}\right)\right] \quad (9)$$

$$Y_t = a_7 \left(1 + \left|\frac{x(t)}{a_8}\right|^{a_9}\right) \quad (10)$$

Analytical predictions using the modified model

The to-be-determined coefficients in the modified mathematical model can also be identified from the test results, as listed in Table 2. A comparison of the experimental and analytical hysteresis loops is shown in Fig. 3. It was found that the analytical predictions using the modified mathematical model show better agreement with the experimental results when the HDR bearings were subjected to either a sinusoidal wave loading or a triangular wave loading.

Table 2. Coefficient identification results: modified model.

Test name	(a) Triangular	(b) Sinusoidal
a_1	0.116	0.107
a_2	-3.02e-06	-2.88e-06
a_3	3.74e-10	2.73e-10
a_4	0.335	0.549
a_5	5.37e-05	7.28e-05
a_6	0.373	0.224
a_7	2.741	3.376
a_8	47.827	60.297
a_9	1.10	1.334

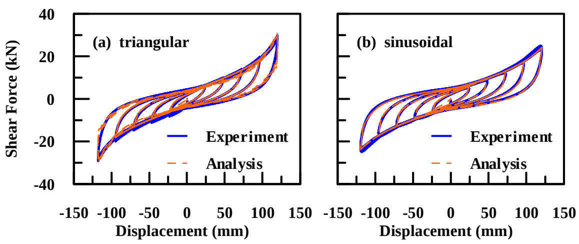

Figure 3. Comparison of hysteresis loops: modified model.

Conclusions

A mathematical hysteresis model was previously proposed by Hwang *et al.* [4] to characterize the highly nonlinear hysteresis behavior of HDR bearings. However, different load patterns or displacement and velocity responses of the HDR bearings may have a significant influence on how this mathematical model predicts their hysteresis behavior, and especially when the bearings are subjected to a triangular wave loading. To obtain more accurate predictions, the mathematical model was modified in this study by incorporating another analysis model. Through a comparison with the experimental results, the modified mathematical model was found to be superior to the mathematical model proposed by Hwang *et al.* [4] in characterizing the hysteresis behavior of HDR bearings.

References

Stanton, J.F. and Roeder, R.W. "Elastomeric Bearings Design, Construction and Materials," NCHRP Report 248, Transportation Research Board, National Research Council, Washington, D.C. (1982)

Naeim, F., and Kelly, J.M. "Design of Seismic Isolated Structures: From Theory to Practice." New York: John Wiley & Sons, Inc. (1999)

Grant, D. N., G. L. Fenves, and A. S. Whittaker. "Bidirectional Modelling of High-Damping Rubber Bearings." J Earthq Engrg 8 S(1): 161–185. (2004)

Hwang, J.S., Wu, J.D., Pan, T.C., and Yang, G. "A Mathematical Hysteresis Model for Elastomeric Isolation Bearings." Earthq Engrg Struct Dyn, Vol. 31(4), pp. 771-789. (2002)

Mullins, L. "Softening of Rubber by Deformation." Rubber Chem Tech, Vol. 42(1), pp. 339-362. (1969)

Clark, P.W., Aiken, I.D., and Kelly, J.M., "Experimental Studies of the Ultimate Behavior of Seismically Isolated Structures." UCB/EERC-97/18, Earthq Engrg Res Ctr. (1997)

Abe, M., Yoshida, J., and Fujino, Y., "Multiaxial Behaviors of Laminated Rubber Bearings and Their Modeling. I: Experimental Study." J Struct Engrg, Vol. 130(8), pp. 1119–1132. (2004).

Abe, M., Yoshida, J., and Fujino, Y., "Multiaxial Behaviors of Laminated Rubber Bearings and Their Modeling. II: Modeling." J Struct Engrg, Vol. 130 (8): pp. 1133–1144. (2004)

Özdemir, H. "Nonlinear Transient Dynamic Analysis of Yielding Structures." Doctoral dissertation, Dept. of Civil and Environ. Engrg, UC Berkeley. (1976)

A Generalized Analytical Model for Sloped Rolling-Type Isolation Bearings

Wang-Chuen Lin [1], Chung-Han Yu [2], Shiang-Jung Wang [3], Chia-Yi Shiau [4], Jenn-Shin Hwang [5] and Kuo-Chun Chang [6]

林旺春 [1]、游忠翰 [2]、汪向榮 [3]、蕭佳益 [4]、黃震興 [5]、張國鎮 [6]

Abstract

This research aims to derive generalized equations of motion and propose a generalized analytical model for a sloped rolling-type isolation bearing in which the two V-shaped surfaces in contact with one cylindrical roller are designed with arbitrary sloping angles. The influences arising from the neglect of higher order terms of sloping angles and vertical excitations in the derivation of the horizontal acceleration prediction of the isolation bearing are numerically examined. It is indicated that the effect of higher order terms of sloping angles on the prediction accuracy is very limited. However, if the acceleration excitation possesses a considerable vertical component, adopting the exact generalized equations of motion, rather than the simplified ones, can obtain more desirable and conservative analysis results for the isolation bearing.

Keywords: sloped rolling-type isolation bearing, generalized analytical model, sloping angle, vertical excitation, numerical verification

Introduction

Among various types of rolling-based metallic isolation bearings, the sloped rolling-type isolation bearings discussed in Lee's (Lee et al., 2010) and Wang's (Wang et al., 2014) studies have attracted sustained attention. As shown in Figure 1, the sloped rolling-type isolation bearings discussed in Lee's and Wang's studies were basically composed of three bearing plates (hereinafter denoted as upper, intermediate, and lower bearing plates) and cylindrical rollers. In Lee's study, the upper and lower bearing plates were designed with flat surfaces in contact with the rollers, while the intermediate bearing plate was designed with V-shaped surfaces. In Wang's study, the three bearing plates were designed with V-shaped surfaces of the same angles. Because of different designs of rolling surfaces, the equations of motion derived in Lee's and Wang's studies were essentially different and cannot be exchanged. This study aims to derive generalized equations of motion for a sloped rolling-type isolation bearing in which the rollers move between two arbitrary sloping surfaces. The derived results are capable of describing the dynamic behavior of the two different isolation bearings discussed in Lee's and Wang's studies respectively. In addition, the influences arising from the neglect of higher order terms of sloping angles and vertical excitations on the transmitted horizontal acceleration responses of the isolation bearing are numerically discussed.

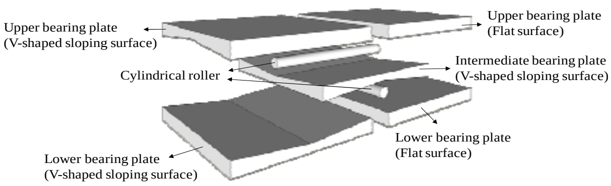

Figure 1. Schematic drawings of sloped rolling-type isolation bearings in Lee's and Wang's studies

[1] Assistant Researcher, National Center for Research on Earthquake Engineering, wclin@narlabs.org.tw
[2] Ph.D. Student, Department of Civil Engineering, National Taiwan University, D03521002@ntu.edu.tw
[3] Research Fellow, National Center for Research on Earthquake Engineering, sjwang@narlabs.org.tw
[4] Assistant Researcher, National Center for Research on Earthquake Engineering, cyshiau@narlabs.org.tw
[5] Division Director, National Center for Research on Earthquake Engineering, jshwang@narlabs.org.tw
[6] Director General, National center for Research on Earthquake Engineering, kcchang@narlabs.org.tw

Derivation of Generalized Equations of Motion

A simplified model comprising a cylindrical roller sandwiched between two V-shaped surfaces designed with different sloping angles θ_1 and θ_2, to represent the dynamic behavior of a sloped rolling-type isolation bearing in one principle horizontal direction and in the vertical direction, is illustrated in Figure 2(a). Here, M, m_1, and m_2 are the seismic reactive masses of the protected object, superior bearing plate, and roller, respectively; r is the radius of the roller; θ_1 and θ_2 are the sloping angles of the superior and inferior bearing plates, respectively. The free body diagrams when $\mathrm{sgn}(x_1)=\mathrm{sgn}(x_2)=1$ and $\mathrm{sgn}(\dot{x}_1)=\mathrm{sgn}(\dot{x}_2)=1$ are shown in Figure 2(b), in which g is the acceleration of gravity; $\ddot{x}_g$ ($\ddot{z}_g$) represents the horizontal (vertical) acceleration excitations; x_1 (z_1), $\dot{x}_1$ ($\dot{z}_1$), and $\ddot{x}_1$ ($\ddot{z}_1$) are the horizontal (vertical) displacement, velocity, and acceleration responses of the protected object and superior bearing plate relative to the origin O, respectively; x_2 (z_2), $\dot{x}_2$ ($\dot{z}_2$), and $\ddot{x}_2$ ($\ddot{z}_2$) are the horizontal (vertical) displacement, velocity, and acceleration responses of the roller relative to the origin O, respectively; I is the moment of inertia of the roller; α is the angular acceleration of the roller; $f_1(f_2)$ and $N_1(N_2)$ are the rolling friction force and normal force acting between the superior bearing plate and roller (between the roller and inferior bearing plate), respectively; and F_D is the built-in friction damping force acting parallel to the slope of the bearing plates.

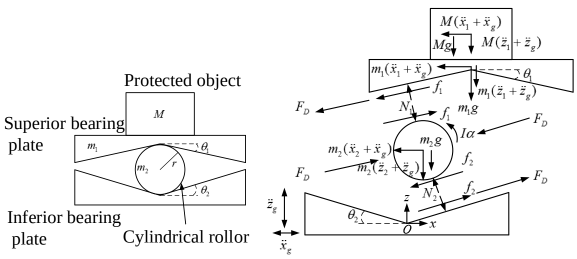

(a) static condition (b) free body diagrams

Figure 2. Simplified models in this study

By considering the dynamic force and moment equilibrium shown in Figure 2(b), and reasonably neglecting m_2, which is in general much smaller than $M+m_1$, the total of nine variables named the exact generalized solutions, α, $\ddot{x}_1$, $\ddot{x}_2$, $\ddot{z}_1$, $\ddot{z}_2$, N_1, N_2, f_1, and f_2, can be solved. The horizontal acceleration response of the protected object and superior bearing plate relative to the origin O is given in Equation (1).

$$\begin{aligned}\ddot{x}_1 = &\frac{-(\cos\theta_1+\cos\theta_2)}{2(M+m_1)[1+\cos(\theta_1-\theta_2)]}\{2F_D\,\mathrm{sgn}(\dot{x}_1)\\ &+(M+m_1)[\ddot{x}_g(\cos\theta_1+\cos\theta_2)\\ &+(g+\ddot{z}_g)(\sin\theta_1+\sin\theta_2)\mathrm{sgn}(x_1)]\}\end{aligned} \tag{1}$$

It can be seen that insightful information might not be easily observed from the exact generalized solutions. Therefore, the following two assumptions for further simplification are taken into consideration: (1) Based on the assumption that the sloping angles θ_1 and θ_2 are small enough, the higher order terms of θ_1 and θ_2 are negligible, i.e. $\cos^2\theta_1 \approx 1$, $\sin^2\theta_1 \approx 0$, and $\sin\theta_1\sin\theta_2 \approx 0$; and (2) Assuming the vertical acceleration excitation $\ddot{z}_g$ is much smaller than the horizontal acceleration excitation $\ddot{x}_g$, the term involving $\ddot{z}_g$ is neglected. Thus, the nine variables can be obtained and named the simplified generalized solutions. The simplified form of Equation (1) is denoted as Equation (2):

$$\begin{aligned}\ddot{x}_1 = &\frac{-(\cos\theta_1+\cos\theta_2)}{4(M+m_1)}[2F_D\,\mathrm{sgn}(\dot{x}_1)+(M+m_1)g\\ &(\sin\theta_1+\sin\theta_2)\mathrm{sgn}(x_1)]-\ddot{x}_g\end{aligned} \tag{2}$$

The simplified generalized solution given in Equation (2) can be applied to represent the dynamic behaviors of the two different sloped rolling-type isolation bearings presented in Lee's and Wang's studies, as shown in Figure 3. Assume θ_1 and θ_2 are correspondingly equal to zero and θ in Lee's study and are both equal to θ in Wang's study to obtain the transmitted acceleration responses along the horizontal direction, as shown below respectively:

$$\ddot{x}_1+\ddot{x}_g = -\frac{g\sin\theta}{2}\mathrm{sgn}(x_1)-\frac{F_D}{(M+m_1)}\mathrm{sgn}(\dot{x}_1) \tag{3}$$

$$\ddot{x}_1+\ddot{x}_g = -\frac{g\sin 2\theta}{2}\mathrm{sgn}(x_1)-\frac{F_D\cos\theta}{(M+m_1)}\mathrm{sgn}(\dot{x}_1) \tag{4}$$

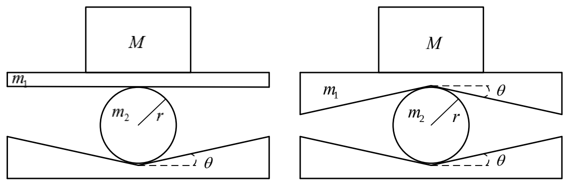
(a) Lee's study (b) Wang's study

Figure 3. Simplified models in Lee's and Wang's studies

Influences of Further Simplifications on Generalized Equations

By ignoring the effects arising from higher order terms of sloping angles and vertical acceleration excitations, the exact generalized solutions can be reduced to the simplified generalized solutions. However, if the sloping angle or vertical acceleration excitation becomes larger, the difference between the numerical results obtained from the exact and simplified generalized solutions might be noticeable. A simplified model composed of a roller with a radius (r) of 100mm is employed, as shown in Figure 2(a). A total of 25 cases of sloped rolling-type isolation bearings in which a commonly used combination of θ_1 and θ_2 respectively varying from 2° to 6° with an increment of 1° is designed, are numerically studied. The built-in friction damping forces (F_D) are designed to be the same for the 25 cases, and are equal to 301N. The total seismic reactive mass of the protected object and superior bearing plate, $M + m_1$, is designed to be 1000N-sec^2/m. Considering the pounding prevention mechanism suggested in Wang's study, an arc rolling range of 21.6mm in the horizontal direction is designed at the intersection of the two inclines of the V-shaped surfaces. When the sloping angle varies from 2° to 6°, the curvature radiuses (R) are designed to be 618mm, 206mm, 155mm, 124mm, and 104mm, respectively. As detailed in Table 1, three recorded earthquake histories obtained from the PEER Ground Motion Database (PEER, 2014), and three generated acceleration histories compatible with the required response spectra (RRS) specified in AC156 (AC156, 2007) and IEEE Std. 693TM-2005 (IEEE, 2005), are adopted as the unilateral and biaxial acceleration inputs with different peak acceleration (PA) scales. The hysteresis loops of different design cases obtained from the exact and simplified generalized solutions respectively given in Equations (1) and (2) under unilateral and biaxial inputs of 100%-Kobe are presented in Figure 4. It can be found from these figures that the exact generalized solutions reflect many obvious fluctuations rather than a perfect constant for the horizontal acceleration response when the roller moves between two sloped surfaces.

Table 1. Acceleration input program

Acc. input	Input earthquake information or response spectrum condition	Excitation direction		Different input PA scales (g) 25%	50%	75%	100%
El Centro	IMPVALL/I-ELC180 IMPVALL/I-ELC-UP Imperial Valley, U.S., 1940/05/19	Unilateral	X	0.08	0.16	0.23	0.31
		Biaxial	X	0.08	0.16	0.23	0.31
			Z	0.05	0.11	0.16	0.21
Kobe	KOBE/KJM000 KOBE/KJM-UP Kobe, Japan, 1995/01/16	Unilateral	X	0.21	0.41	0.62	0.82
		Biaxial	X	0.21	0.41	0.62	0.82
			Z	0.09	0.17	0.26	0.34
ChiChi	CHICHI/CHY028-N CHICHI/CHY028-V Chi-Chi, Taiwan, 1999/09/21	Unilateral	X	0.19	0.38	0.57	0.76
		Biaxial	X	0.19	0.38	0.57	0.76
			Z	0.09	0.17	0.26	0.34
AC 156-1	RRS specified in AC156	Unilateral	X	0.13	0.25	0.38	0.50
	Isolated equipment is placed at 3rd floor (8.75m in elevation) of a 7-story building (24m in height) at Taipei City	Biaxial	X	0.13	0.25	0.38	0.50
			Z	0.06	0.13	0.19	0.25
AC 156-2	RRS specified in AC156	Unilateral	X	0.25	0.50	0.75	1.00
	Isolated equipment is placed at 3rd floor (8m in elevation) of a 3-story building (12m in height) at Nantou County	Biaxial	X	0.25	0.50	0.75	1.00
			Z	0.13	0.25	0.38	0.50
IEEE	RRS specified in IEEE Std 693TM-2005 for high performance level	Unilateral	X	0.25	0.50	0.75	1.00
		Biaxial	X	0.25	0.50	0.75	1.00
			Z	0.20	0.40	0.60	0.80

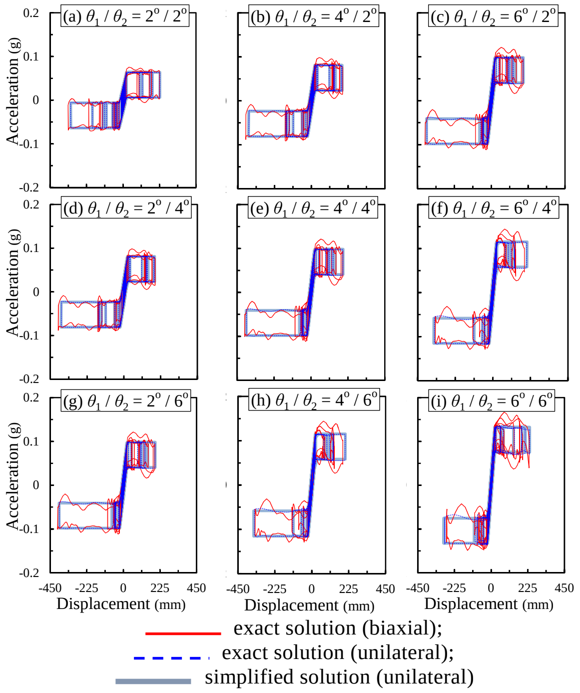

Figure 4. Comparison of hysteresis loops of different design cases under 100%-Kobe

To separately and clearly discuss the extent of influences arising from neglecting of higher order terms and vertical acceleration excitations on the horizontal acceleration predictions, two indices, ER_1, and ER_2, are defined:

$$ER_1 = \frac{\max\left(\left|A_{uni,exact}\right|\right) - \max\left(\left|A_{uni,simplified}\right|\right)}{\max\left(\left|A_{uni,simplified}\right|\right)} \times 100\% \quad (5)$$

$$ER_2 = \frac{\max\left(\left|A_{bi,exact}\right|\right) - \max\left(\left|A_{uni,exact}\right|\right)}{\max\left(\left|A_{uni,exact}\right|\right)} \times 100\% \quad (6)$$

where $A_{uni,exact}$ and $A_{bi,exact}$ are the horizontal acceleration predicted by Equation (1) under unilateral and biaxial excitations, respectively; $A_{uni,simplified}$ is the horizontal acceleration predicted by Equation (2) under unilateral excitations. It is found from Figure 5 that the larger the design sloping angle is, the more apparent effect revealed from neglect of higher order terms of sloping angles on the ER_1 value exerts. In this study, nevertheless, the maximum ER_1 value is only 5.10% for the design case of (θ_1, θ_2)=(6°,6°) under unilateral-100%-ChiChi. Therefore, it can be concluded that the effect of higher order terms of sloping angles on the acceleration prediction accuracy is very limited and can be rationally negligible in engineering practice. It can be found in Figure 6 that the differences between the maximum horizontal acceleration predictions by using the exact generalized solutions under unilateral and biaxial excitations, i.e. the ER_2 value, might be worthy of attention. It is apparent that a larger vertical PA value will lead to a more significant effect without regard to vertical acceleration excitations on the ER_2 value. As shown in Figure 7, it is evident that in the same design case, the larger the vertical PA value is, the more significant effect without considering vertical acceleration excitations on the ER_2 value produces. In this study, the maximum ER_2 value is 36.59% in the design case of (θ_1,θ_2)=(2°,2°) under biaxial-100%-IEEE, which might not be very acceptable compared to the maximum ER_1 value mentioned, i.e. 5.10%. Therefore, to preclude a non-conservative design result, the effect of vertical acceleration excitations on the maximum transmitted horizontal acceleration response of the isolation bearing should be taken into account, especially when the vertical excitation possesses a larger PA value.

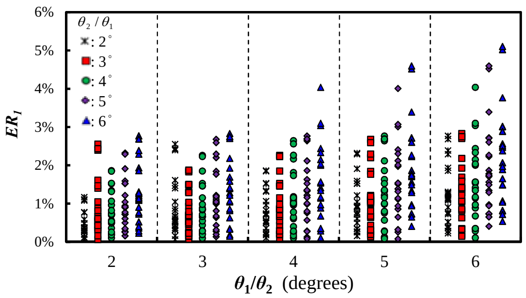

Figure 5. Variations of ER_1 values under all unilateral acceleration inputs

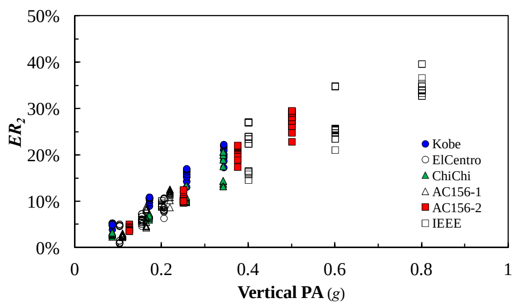

Figure 6. Variations of ER_2 values under all biaxial acceleration inputs

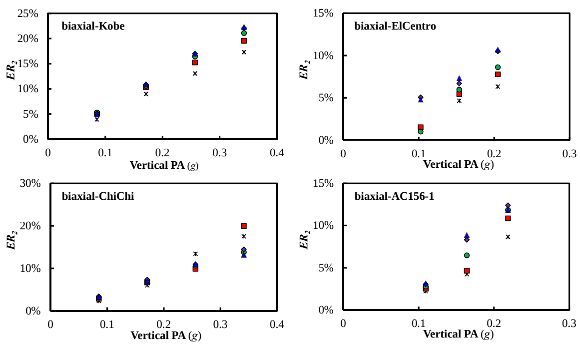

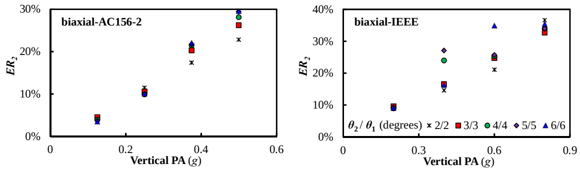

Figure 7. Variations of ER_2 values with various vertical PA scales for five design cases of $\theta_1=\theta_2$ under all biaxial acceleration inputs

Conclusions

To obtain a more comprehensive performance design procedure for the sloped rolling-type isolation bearing in which the cylindrical rollers move between two V-shaped surfaces designed with arbitrary sloping angles, an analytical model that takes into account more generalized equations of motion is developed in this study. Under the specific design conditions, the proposed analytical model can make a valid generalization in Lee's and Wang's mathematical models by theoretical verification. A series of numerical studies are performed to quantitatively discuss the influences arising from neglecting of higher order terms and vertical excitations on the transmitted horizontal acceleration responses of the isolation bearing. The numerical results reveal that the effect of vertical acceleration excitations play~~s~~ a crucial role in prediction accuracy compared to that of higher order terms of sloping angles. When the acceleration excitation possesses a considerable vertical component, adopting the exact generalized equations of motion, rather than the simplified ones, can achieve more precise and conservative analysis results for the sloped rolling-type isolation bearing.

References

Lee GC, Ou YC, Niu T, Song J and Liang Z. (2010). "Characterization of a roller seismic isolation bearing with supplemental energy dissipation for highway bridges," Journal of Structural Engineering, ASCE, 136(5): 502-510.

Wang SJ, Hwang JS, Chang KC, Shiau CY, Lin WC, Tsai MS, Hong JX and Yang YH. (2014). "Sloped multi-roller isolation devices for seismic protection of equipment and facilities," Earthquake Engineering and Structural Dynamics, 43(10): 1443-1461.

Pacific Earthquake Engineering Research (PEER) Ground Motion Database. Retrieved Aug. 15, 2014 from the World Wide Web: http://peer.berkeley.edu/peer_ground_motion_database/.

AC156. (2007) "Acceptance criteria for seismic qualification by shake-table testing of nonstructural components and systems," ICC Evaluation Service Inc..

IEEE Std 693TM-2005. (2006). "IEEE recommended practice for seismic Design of Substations," Institute of Electrical and Electronics Engineers (IEEE) Power Engineering Society, NY.

Shaking Table Tests for the Seismic Improvement of a Typical Sprinkler Piping System Used in Hospitals

Zen-Yu Lin[1], Fan-Ru Lin[2], Juin-Fu Chai [3], Jian-Xiang Wang[4] and Kuo-Chun Chang[5]

林震宇 [1]、林凡茹 [2]、柴駿甫 [3]、王鑑翔 [4]、張國鎮 [5]

Abstract

The objective of this paper is to identify the failure modes of a typical sprinkler piping system used in hospitals and to propose appropriate improvement strategies for higher seismic performance. An actually damaged sprinkler piping system from a “designated as responsible” hospital during the Taiwan Jiashian earthquake in 2010 was duplicated for the shaking table tests. The same damage that occurred during the earthquake event was reproduced in the original configuration of the sprinkler piping. In addition, the modified configurations with the proposed seismic restraint devices were also tested. The test results show that the screwed fitting of the small-bore tee branch is the most vulnerable part of the tested piping system. The optimum improvement strategy is not only to strengthen the main pipe with braces but also to use flexible hose near the tee branch to decrease both the force and displacement demands on the screwed fittings.

Keywords: sprinkler piping systems, shaking table testing, seismic improvement strategy

Introduction

Based on the lessons learned from the 1999 Chi-Chi earthquake, specifically that the immediate operation of critical facilities after strong earthquakes relies heavily on the performance of important nonstructural components, critical facilities are now required to ensure the seismic capability of their water supply, power supply, and fire suppression systems. Owing to the lack of mature evaluation methods and an approved code of practice for seismic upgrading of nonstructural components, in hospitals for instance, the mechanical/electrical systems have still not been evaluated or retrofitted. An example of this was observed in a designated hospital during the 2010 Jiashian earthquake in Taiwan, where a reduction in medical functionality was caused by serious flooding due to a broken small-bore pipe of the sprinkler system. For fire sprinkler systems in general buildings, NFPA 13 [1] provides a common code of practice for seismic installation. Instead of stress analysis, a rule-based approach is proposed by the NFPA standard. However, its effectiveness for seismic upgrading needs to be verified by more extensive studies. An ongoing research program covering assessment and improvement strategies for typical configurations of sprinkler piping systems in hospitals was organized by the National Center for Research on Earthquake Engineering (NCREE). This paper focuses on the seismic behavior of a typical subsystem of horizontal sprinkler piping using shaking table tests, which is a part of the research program. The damaged sprinkler piping system in the hospital mentioned above was partially duplicated on the shaking table. The objective of this testing is to identify the failure modes of a typical sprinkler piping system in hospitals and to propose appropriate improvement strategies for higher seismic performance. The configurations with seismic restraint devices, including braces, mechanical couplings and flexible hoses, were also preliminarily tested to investigate efficiencies.

In-Situ Investigation

In order to assess the typical configuration of

1 Research Assistant, National Center for Research on Earthquake Engineering.
2 Assistant Researcher, National Center for Research on Earthquake Engineering.
3 Research Fellow, National Center for Research on Earthquake Engineering.
4 Research Assistant, National Center for Research on Earthquake Engineering.
5 Professor, Department of Civil Engineering, National Taiwan University.

fire sprinkler piping at hospitals, an in-situ investigation was carried out at the hospital building where the fire sprinkler piping system was damaged during the 2010 Jiashian earthquake (Fig. 1). As shown in Fig. 2 the broken segment of the piping system was located in a patient room at the top floor of the six story building. Restricted by the confined space above the suspended ceiling system, four pipes along the corridor of diameters 6", 2-1/2", 6" and 4" (from left to right) were carried by the same trapeze frame supports, where the left 6" diameter pipe was the cross main of the sprinkler piping system (Fig. 3). Based on the results of ambient vibration tests and impact hammer tests, the fundamental frequency of the building structure was identified to be about 2.0 Hz in both horizontal directions, and 5.37 Hz in the piping in the transverse direction of the cross main pipe. Limited to the scale of the shaking table, only the typical unit of sprinkler piping for the area of the patient room and a part of the cross main were duplicated in the laboratory (Fig. 3). To obtain reasonable assumptions about the boundary conditions of the tested segment of the cross main in the shaking table tests, preliminary numerical models of the complete piping system on the 6th floor and the test specimen were both established according to the in-situ investigation of the configuration and restraint conditions in the hospital and that of the actual test specimen.

Fig. 1 Flooding at a hospital during the 2010 Jiashian earthquake

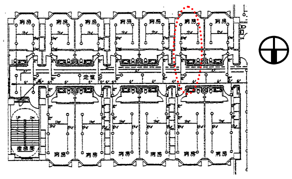

Fig. 2 Plane drawing of the sprinkler system and damaged part in the 2010 Jiashian earthquake

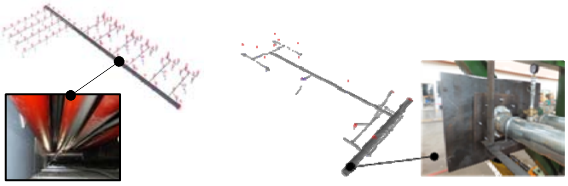

Fig. 3 Numerical model of the horizontal piping system

Test Setup

The objective of this test was to identify the failure modes of a typical sprinkler piping system in hospitals and to propose appropriate improvement strategies for higher seismic performance (Fig. 4 and 5A). We attempted to reproduce the same damage that occurred in the 2010 Jiashian earthquake in a sample with the original configuration of screwed fittings. In addition, the modified configurations with proposed seismic restraint devices, including braces, flexible hoses and couplings, were also arranged at the proper positions to verify their improvement efficiencies (Table 1 and Fig. 5). The tested sub-system was hung by a rigid steel frame that was designed to be stiff enough to transfer the motion of the shaking table without significant effects. Two types of earthquakes consisting of horizontal motions were measured in tests near the hang points on the steel frame [2]. The purpose of Type A was to verify whether seismic restraint devices satisfy the requirement of the building code in Taiwan [3], whereas the purpose of Type B was to simulate the floor response in the hospital during the Jiashian earthquake. Fig. 6 shows the layouts of the instruments including accelerometers, magnetic transducers and strain gages in the DBF testing case.

Table 1 Testing configurations

OC	Original configuration
CT	Coupling near the tee branch
DB	Double braces
FH	Flexible hose
CB	Coupling between the tee branch and partition
DBF	Double braces with flexible hose

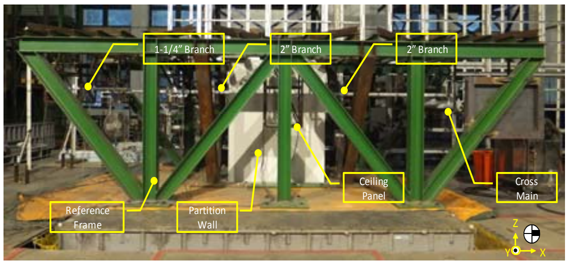

Fig. 4 Shaking table test for the sub-system.

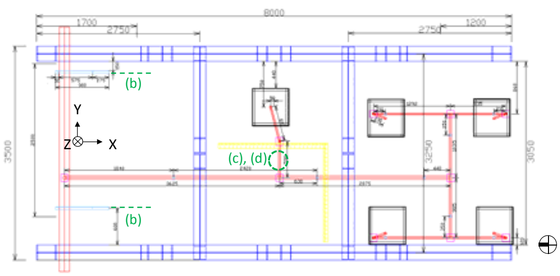

(a) Basic test configuration

(b) Braces (c) Flexible hose (d) Coupling

Fig. 5 Test configuration and seismic restraint devices

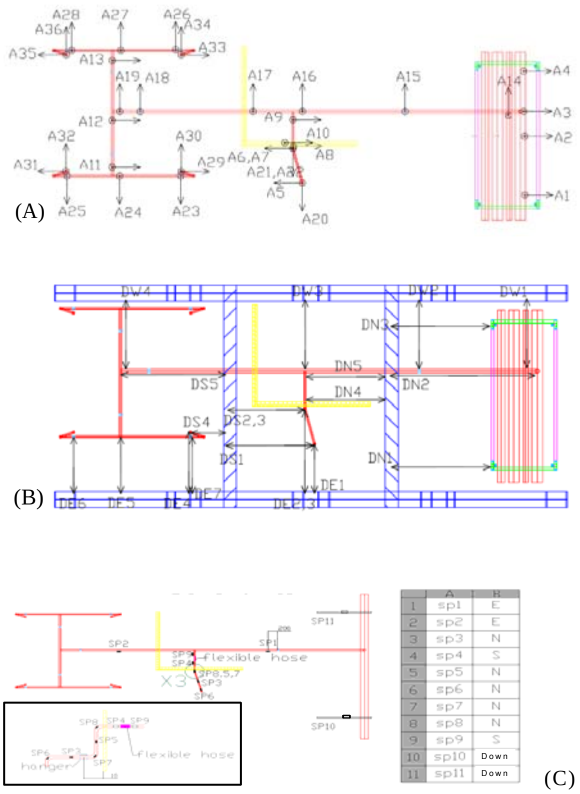

Fig. 6 Layouts of (A) accelerometers and (B) transducers (C) Strain gages for DBF case

Test Results

Fig. 7 depicts the identified natural frequency and the first mode shape along the X-axis of each test configuration from the results of the resonant frequency survey tests. The first mode of the original configuration of the sub-system was translation along the X-axis. It can be seen that the braces increased the natural frequencies significantly, whereas couplings and flexible hoses decreased the natural frequencies and changed the stress distribution of the local segments.

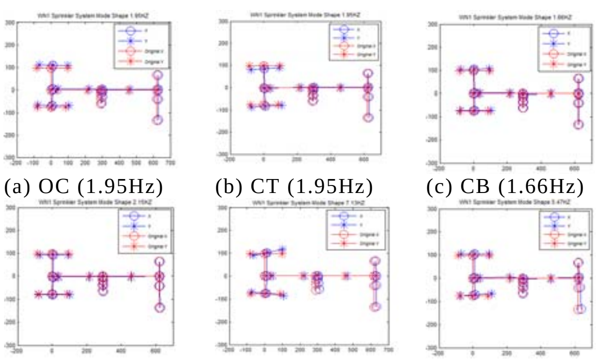

(a) OC (1.95Hz) (b) CT (1.95Hz) (c) CB (1.66Hz)
(d) FH (2.15Hz) (e) DB (7.13Hz) (f) DBF (5.47Hz)

Fig. 7 The first Mode shape and natural frequency along X-axis of each test configuration

In order to avoid leakage in the sprinkler piping system and associated damage to the adjacent architectural components due to seismic interaction, three performance indexes were examined during and after each test: (1) the damage of the piping segments; (2) enlarged diameters of the reaming on ceiling boards and partition walls due to impacts caused by the sprinkler heads and piping segments; and (3) the leakage of contained water. The test results of the original configuration showed that the screwed fitting of the 1” drop at the tee branch was the most vulnerable part of the tested piping system, and was damaged at 100% intensity in the Type B test (Fig. 8A). Although there was no leakage in the tests of the configuration with the flexible hose (FH, Fig. 9), all ceiling boards were broken, which could seriously impair medical service (Fig. 8B and Fig. 10). On the other hand, due to the brittle failure caused by the screwed fitting and couplings, the mechanical behavior of both devices should be further studied (Fig. 8C and D). The optimum improvement strategy is not only to strengthen the main pipe with braces but also to use flexible hose near the tee branch to decrease both the shear and displacement demands on the screwed fittings (Fig. 8E).

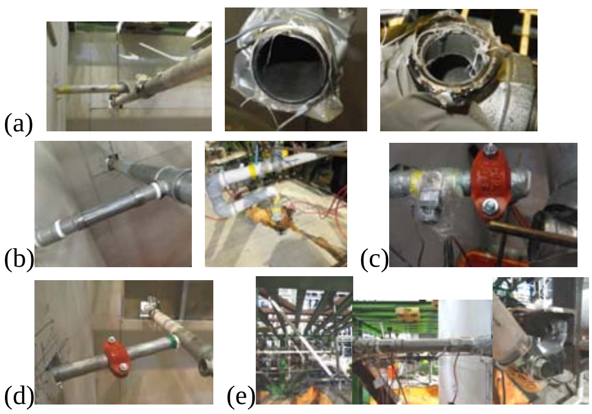

Fig. 8 Damage states of each test configuration: (A) OC; (B) FH; (C) CT; (D)CB; (E)DBF.

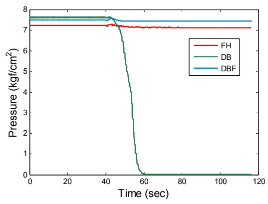

Fig. 9 Leakage conditions in Type A tests

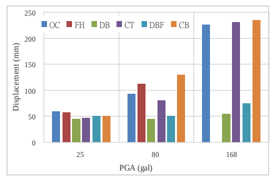

Fig. 10 Diameter of the reaming on the ceiling board in Type B tests

Fig. 11 to Fig. 13 depict the seismic behavior observed in Type A and B tests of different configurations. Note that leakages occurred at 20.4 seconds and 40 seconds in the Type B test (Fig. 11 and 12) of the original configuration (OC) and in the Type A test (Fig. 13) of the configuration with Double Braces (DB). Comparing the responses of the 6” cross main (Fig. 11A and 12A) and the damaged 1” drop (Fig. 11B and 12B) in the OC test, it can be seen that the partition wall partially restrained the displacement response of the 1” drop but enlarged its acceleration response. Comparing this with the OC test, the configurations with braces (DB and DBF) successfully reduced the displacement response of the whole piping system (Fig. 11) and also reduced the impact effects on the 1” drop (Fig. 12). The strain responses of the 1” drop in the DB, FH and DBF configurations (Fig. 13A) demonstrate that using both braces at the main pipe and flexible hoses at the drops near the partition walls can effectively decreases the internal force of small-bore pipes and reduces the possibility of leakage. However, it should be noted that the braces and related attachments in the DBF configuration were subjected to more seismic force than those in the DB configuration due to there being less restraint offered by the partition wall (Fig. 13B). A more detailed design of the attachments of the braces is needed to avoid the damage observed in the Type A test of the DBF configuration (Fig. 8E).

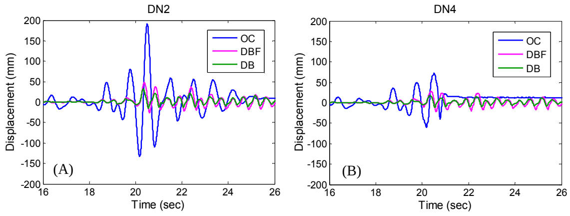

Fig. 11 Displacement response in Type B tests of OC, DB and DBF: (A) 6” cross main; (B) 1” drop.

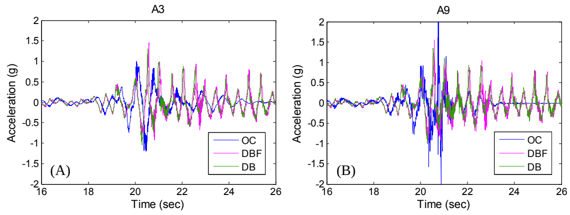

Fig. 12 Acceleration response in Type B tests of OC, DB and DBF: (A) 6” cross main; (B) 1” drop.

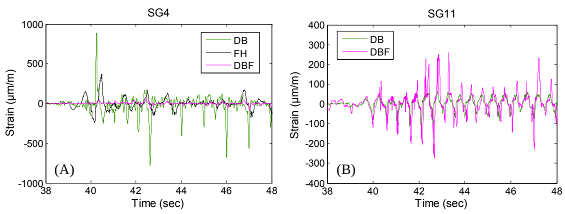

Fig. 13 Strain response in Type A tests of DB, FH and DBF: (A) 1” drop; (B) Bracing.

Conclusions

In view of the immediate needs of emergency medical services provided by hospitals after strong earthquakes, an ongoing research program covering assessment and improvement strategies for a typical configuration of sprinkler piping systems in hospitals has been organized by the NCREE. From the results of shaking table tests, the main cause of the damaged case was found to be the poor moment capacity of the screwed fitting of the small-bore tee branch. Due to the brittle failure caused by the screwed fitting and couplings, the mechanical behavior of both devices were investigated further and introduced in a study by Lin’ [4]. The optimum improvement strategy to achieve higher nonstructural performance for the piping system is to strengthen the main pipe with braces and to decrease moment demands on the small-bore piping at the tee branch by using a flexible hose. It should be noted that well designed attachments for the braces were needed to avoid the damage observed in the DBF tests.

References

National Fire Protection Association (2010), “Standard for the Installation of Sprinkler Systems”, NFPA 13, U.S.

Lin, F.R., Chai, J.F., Lin, Z.Y., Wang, J.X., Chang K.C., Liao, W.I. (2014), “Shaking Table Tests for Seismic Improvement of A Typical Sprinkler Piping System in Hospital”, *The 5th Asia Conference on Earthquake Engineering*, Taipei, Taiwan.

Ministry of the Interior, MOI (2011), “Seismic Design Specifications and Commentary of Buildings” (in Chinese), Taiwan.

Lin, Z.Y., Huang, J.G., Lin, F.R., Chang K.C., and Chai, J.F. (2014), “A Study on Seismic Behavior of Mechanical Couplings for Fire Protection Sprinkler Piping Systems In Hospital”, *The 5th Asia Conference on Earthquake Engineering*, Taipei, Taiwan.

Development of Simplified Seismic Evaluation Program for Equipment in Hospitals

Tzu-Chieh Chien [1], Juin-Fu Chai [2] and Fan-Ru Lin[3]

簡子婕 [1]、柴駿甫 [2]、林凡茹 [3]

Abstract

In order to ensure the reliability of hospitals designated responsible for the provision of post-earthquake acute services, a project was organized by the National Center for Research on Earthquake Engineering to propose seismic evaluation and strengthening guidelines for nonstructural components in hospital buildings. Owing to the onerous work required to improve the seismic performance of various nonstructural components in hospitals, a simplified program was established in this study to execute a preliminary seismic evaluation for individual components needed to support the medical services in critical care areas. The objective of this program is to obtain the evaluation results rapidly and effectively by inputting the characteristic parameters of the selected components, and also to determine the seismic demands if needed. Finally, depending on the capacity of the bolts used for strengthening, the program could provide a preliminary resolution of outliers to improve unacceptable seismic responses as mentioned above.

Keywords: Nonstructural components, Hospital equipment, Simplified evaluation.

Introduction

In the study cited in "Rehabilitation Objectives and Evaluation Criteria for Hospitals" (Hwang et al., 2013), which was organized by the National Centre for Research on Earthquake Engineering (NCREE), a program was established to execute preliminary seismic evaluation for individual medical equipment. This article introduces the interface, framework, and process of the program, and then explains the detailed logic of each step. Finally, for equipment that is likely to overturn or slide during seismic events, the program provides analyses of anchor bolts by calculating the demand and capacity of the tension and shear force.

Although the evaluative formulation has been used generally, if it is over simplified it may not correspond with the actual forces working in real situations. To avoid underestimating the result, this study establishes a series of coefficients by using software simulation to modify the formula.

Program Sheets and Framework

Users should follow the steps shown in Figure 1 and key in the parameters of the hospital and nonstructural components separately into two MS Excel spreadsheets. Figure 2 shows the hospital spreadsheet, and the cells include the classification and location of the hospitals, the seismic related coefficient, and the height of each floor. The equipment spreadsheet is shown in Figure 3, having one column for one item, and the cells include information about the components (e.g., name, sort, location, weight). The estimated process will run on other spreadsheets in the background of the program.

Users are required to fill in the anchor bolt spreadsheet (Figure 4), and the design information will provide the database for evaluation. Once the blank anchor bolt information for the equipment that should be strengthened has been filled in, the program will determine whether the strength of the anchor bolts is sufficient.

[1] Research Assistant, National Center for Research on Earthquake Engineering
[2] Research Fellow, National Center for Research on Earthquake Engineering
[3] Assistant Researcher, National Center for Research on Earthquake Engineering

Logic of Each Steps

Performance Level

Performance level depends on the classification and service space of the hospital equipment (Figure 5). The space in a hospital can be classified as either a human occupied area or non-human occupied area, or as either an essential care area (including critical medical space and emergency exit access) or general area. As per Hwang et al., (2013), the performance level will be classified differently for the same equipment that serves in different places.

Earthquake Hazard Level

According to accredited hospitals, hospitals are classified into three levels: 'academic medical centers', 'metropolitan hospitals', or 'local community hospitals'. Furthermore, hospitals designated responsible for acute services are also classified into three levels: 'severe', 'moderate', and 'general', according to their assigned capability for particular emergency treatments. As illustrated in Figure 6, the same performance level is assigned to different earthquake hazard levels based on the hospital classification.

Seismic Response of Equipment

The evaluation of the equipment Seismic response is based on the theory (Ishiyama, 1982) expressed in Eq. 1 to Eq. 3, where A is peak acceleration at each floor (Hwang et al., 2013), and V is peak velocity at each floor (Chen, 2008).

$$A > \mu g \quad \text{(Sliding)} \qquad \text{(Eq.1)}$$

$$B/H < A/g \quad \text{(Rocking)} \qquad \text{(Eq.2)}$$

$$V > 10 \times B^{*}/\sqrt{H} \quad \text{(Overturning)} \qquad \text{(Eq.3)}$$

The seismic response evaluation process is shown in Figure 7. Depending on the evaluation result, which is determined to be "sliding" or "overturning", the equipment should undergo certain follow-up steps for strengthening.

Evaluation and Strengthening of Bolts

Common Evaluation

To calculate the tension and shear demand force (T_{ua} and V_{ua}), Eq.4 and Eq.5 are used in common. For T_{ua}, the dead load and seismic force are combined and simplified into one equation, where it is necessary only to examine the X-axis and Y-axis and then select the maximum value of these two axes. For V_{ua}, it simply divides the horizontal seismic force into each restraint joint.

$$T_{ua} = \lfloor F_{ph} \times h_G - (W_p - F_{pv}) \times l_G \rfloor / (L \times n_t) \qquad \text{(Eq.4)}$$

$$V_{ua} = F_{ph} / n \qquad \text{(Eq.5)}$$

Reaction of Joint Restraint Modification

Eq.4 and Eq.5 ignore that the force might concentrate on parts of the restraints, meaning that the demand force could be underestimated. Therefore,Eq.6 and Eq.7 were established to modify the condition mentioned above.

For T_{ua} and using load combination *0.9D+1E*, the dead load and seismic force are considered separately, and only the bolt is examined, which is suspected to be the maximum value. In the equation, T_W is the tension force caused by the dead load (Eq.8), T_E is caused by seismic forces T_{QX}, T_{QY} , and T_{QZ}, which lie on three different axes (Eq.9), Considering that the condition with the maximum value lying on the horizontal axes does not appear at the same time, the maximum value should be calculated by permutation and combination in the ratio 1:0.3.

In Eq.10, V_E is the shear force caused by the seismic force. In this study, the X and Y-axis seismic forces appear at the same time, and so we combined them using SRSS in the ratio 1:0.3 as in Eq.9.

$$T_{ua} = 0.9 \times \phi_{TW} \times T_W + \phi_{TE} \times T_E \qquad \text{(Eq.6)}$$

$$V_{ua} = \phi_{VE} \times V_E \qquad \text{(Eq.7)}$$

Coefficient for Amendment

From the analysis using SAP2000, we derived a series of coefficients ϕ_{TW} , ϕ_{TE} , and ϕ_{VW} by comparing the analytic results with the equation we used generally. It would be more conservative if we multiply the coefficients in Eq.6 and Eq.7.

The coefficients are simplified as in Figure 7 (using ϕ_{TE} as an example) for the program evaluating process. In this figure, the coefficient values have an impact on aspect ratio, the eccentric condition, and the restraint conditions. The program will determine the coefficients based on the parameters that users filled in Figure 3.

$$T_W = \min\left(W_p \times \min(l_{xG}, L_x - l_{xG}) / L_x \times n_y, W_p \times \min(l_{yG}, L_y - l_{yG}) / L_y \times n_x\right) \qquad \text{(Eq.8)}$$

$$T_E = \max\left(T_{QX} + 0.3 \times T_{QY} + T_{QZ}\ ,\ 0.3 \times T_{QX} + T_{QY} + T_{QZ}\right) \qquad \text{(Eq.9)}$$

$$T_{QX} = \frac{F_{ph} h_G}{L_x n_y}\ ,\ T_{QY} = \frac{F_{ph} h_G}{L_y n_x}\ ,\ T_{QZ} = \max\left(\frac{F_{pv} \times \max(l_{xG}, L_x - l_{xG})}{L_x \times n_y}, \frac{F_{pv} \times \max(l_{yG}, L_y - l_{yG})}{L_y \times n_x}\right)$$

$$V_E = \sqrt{(F_{ph}/n)^2 + (0.3 \times F_{ph}/n)^2} \qquad \text{(Eq.10)}$$

Capacity of anchor bolt strengthening

As per the criteria used in Hwang et al., (2013), the capacities of the anchor bolts ϕT_n and ϕV_n are evaluated using Figure 4, which users fill in. It is then calculated with T_{ua} and V_{ua} using Eq.6 and Eq.7. If it satisfies Eq.11, the blank "Result" in Figure 3 will show "OK", otherwise, it will show "NO!!"

If the result does not satisfy the equation, users should adjust the size of the anchor bolt or restraint condition using trial and error until it shows "OK". The equipment can be strengthened in this way.

$$(T_{ua} / \phi T_n)^{1.5} + (V_{ua} / \phi V_n)^{1.5} \leq 1.0 \qquad \text{(Eq.11)}$$

Conclusions

Even though the evaluation process in the study is more complex than a common evaluation, it would be more convenient for users because all the processes are pre-coded into MS Excel.

Furthermore, we will develop the condition where the equipment is fixed on the wall or ceiling and has been strengthened by a z-shape stopper or weld. We look forward to the program becoming more complete and convenient.

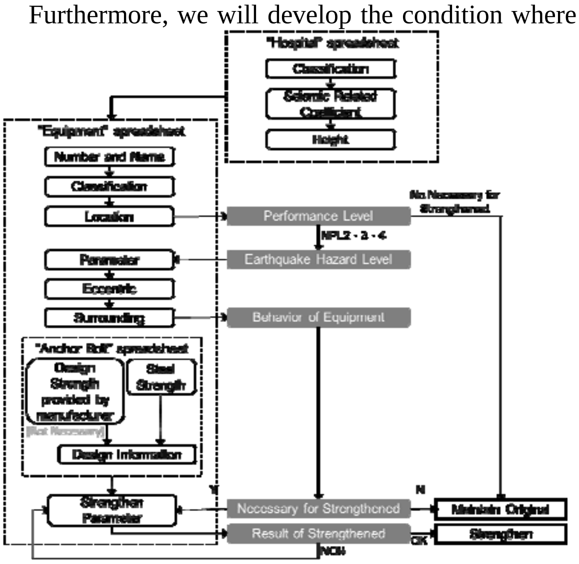

Figure 1. Program framework and flow chat.

Hospital Accreditation：	Medical Center
Emergency Responsibility Hospitals：	General Designated Responsibility Hospitals
Coefficient in seismic code of Taiwan	
Site：	Near Fault
DBE Coefficient of Horizontal Design Spectrum Acceleration-factor (S_S^D)：	0.8
DBE Nea-Fault Factor(Na)：	1.42
DBE Coefficient of Fa：	1
MCE Coefficient of Horizontal Design Spectrum Acceleration-factor (S_S^M)：	1
MCE Nea-Fault Factor(Na)：	1.32
MCE Coefficient of Fa：	1
Floor	**Height of Each Floor(cm)**
RF	5450
15F	
14F	
13F	
12F	5050
11F	4650
10F	4250
9F	3950
8F	3450
7F	3050
6F	2650
5F	2100
4F	1580
3F	1050
2F	540
1F	0

Figure 2. Hospital Spreadsheet.

References

J.S. Hwang et al., (2013). Seismic Evaluation and Strengthening Guidelines for Hospital Buildings, Taipei: National Center for Research on Earthquake Engineering, NCREE-13-037.

Ishiyama Y., (1982). "Motions of Rigid Bodies and Criteria for overturning by earthquake excitations", Earthquake Engineering and Structural Dynamic, 10, pp.635-650.

W.C. Chen, (2008), A Research on Evaluating Floor Vibration in Earthquakes for Non-structural Elements Damage Estimate, Master thesis, National Cheng Kung University, Tainan.

Number and Name		
Number:		Normal Supply System-001
Name:		Water Chiller Unit
Classification		
Types:	(LIST)	Mechanical Equipment
Sorts:	(LIST)	HVAC System Component
Categories:	(LIST)	Vibration isolated
Location		
Location:	(LIST)	Others Human Occupied
Floor:	Number (R for Roof,-1~-5 for Basement)	R
Parameter		
Weight (W_p)：	kgf	2000
設備固定點位置：	(選單)	樓板
Dimension:	Length of X-Axies (L_x) m	2.26
	Length of Y-Axies (Ly) m	2.15
	Heught (Container Included) (h) m	2.40
Distance between top to floor:	(Container Included) m	2.22
Eccentric		
X-Axis Eccentric：	(Filled with Y or N)	Y
X-Axis Distance between the Edge to the Center of Gravity：	(Blank Space for Non-Eccentric or Uncertain) (L_{xG}) m	1.00
Y-Axis Eccentric：	(Filled with Y or N)	Y
Y-Axis Distance between the Edge to the Center of Gravity：	(Blank Space for Non-Eccentric or Uncertain) (L_{yG}) m	1.00
Z-Axis Eccentric：	(Filled with Y or N)	N
Z-Axis Distance between the Edge to the Center of Gravity：	(Blank Space for Non-Eccentric or Uncertain) (h_G) m	
Surrounding		
Connection with Structure :	(LIST)	Non-Fixed
Material of Floor Surface :	(LIST)	Rubber
Material of floor :	(LIST)	Concrete
Lean on the Wall :	(LIST)	Independent
是否需耐震評估(易損程度)：		Y
Performance Level		NPL4
Earthquake Hazard Level		DBE
Seismic Response of Equipment		Sliding
Necessary for Strengthening		**Y**
Bolt Strenrthening	(Blank Space for No Necessary Strenthen)	
Number of bolts on X-Axies :		4
Number of bolts on Y-Axies:		4
Type or Size:	(LIST)	Hilti-M10
Depth in concrete:	in	4.00
Anchorage on Concrete or Other Material :	(LIST)	
Strength of Base Material :	psi	2800
Result		**OK**

Figure 3. Equipment Spreadsheet.

Steel Strength of Anchor Bolt	**(psi)**				
	f_{ya}	92800			
	f_{uta}	116000			
Design Information of Anchor Bolt	**Data**	d_o	he(min)	Ase	Np
	Item Number	in	in	in^2	lb
	Hilti-M8	0.47	2.36	0.057	2810
	Hilti-M10	0.59	2.76	0.090	4496
	Hilti-M12	0.71	3.15	0.131	
	Hilti-M16	0.94	3.94	0.243	
Design Strength (Design Strength of Anchor Bolt in Different Base - Provided by Manufacturer)	**ϕ Tn (psi)**	Strength of Concrete			
	Item Number	2500	3000	4000	6000
	Hilti-M8	1825	2000	2310	2830
	Hilti-M10	2920	3200	3695	4525
	Hilti-M12	4360	4775	5515	6755
	Hilti-M16	6095	6675	7705	9440
	ϕ Vn (psi)	Strength of Concrete			
	Item Number	2500	3000	4000	6000
	Hilti-M8	2160	2365	2730	3345
	Hilti-M10	7685	8420	9720	11905
	Hilti-M12	9390	10285	11880	14550
	Hilti-M16	13125	14375	16600	20330

Figure 4. Anchor Bolt Spreadsheet.

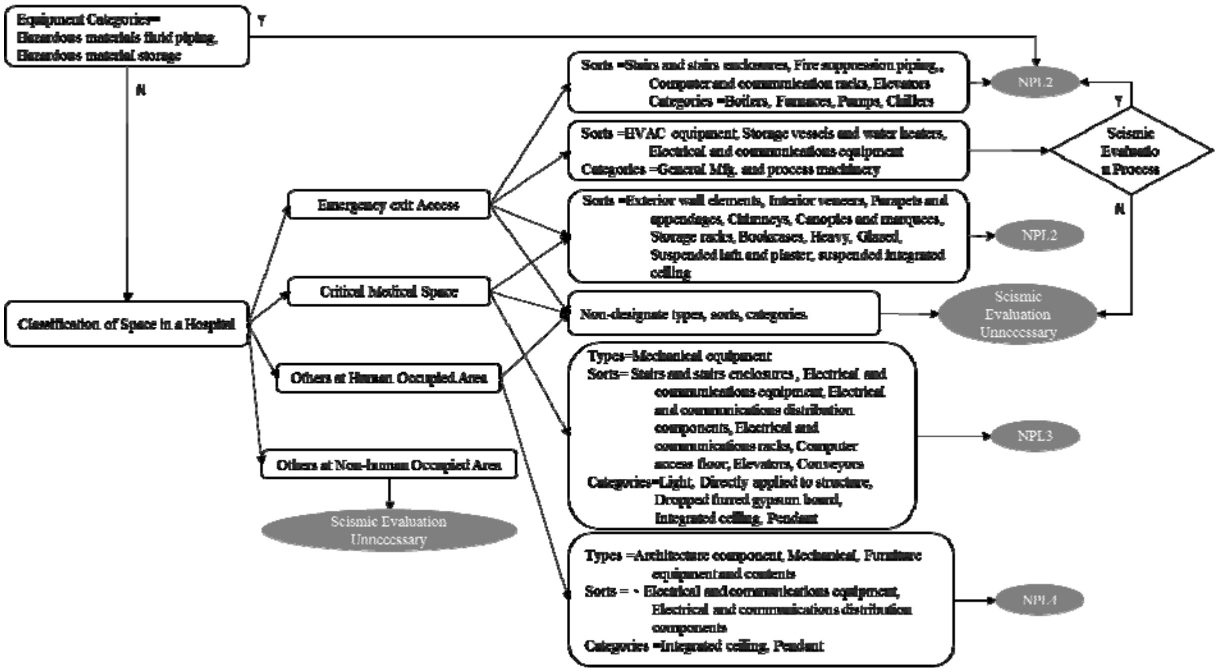

Figure 4. Performance level evaluation process.

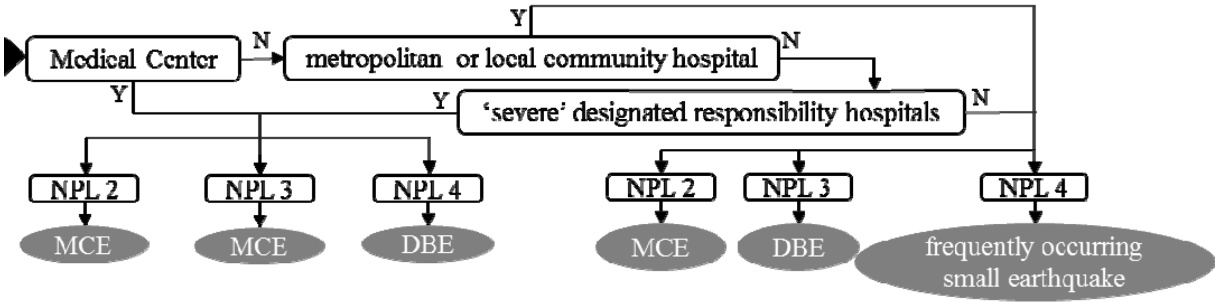

Figure 5. Earthquake hazard level determination process.

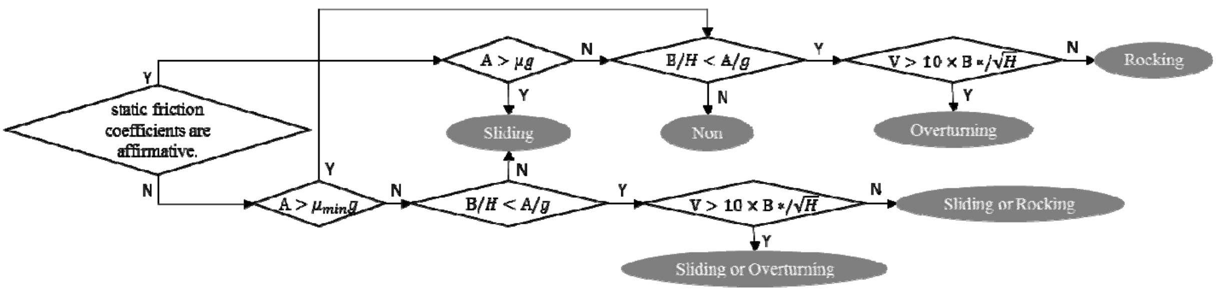

Figure 6. Seismic response evaluation process.

<table>
<tr><td rowspan="2">TE</td><td>Eccentric - NONE</td><td colspan="3">Eccentric – X or Y AXIS</td><td colspan="3">Eccentric – X and Y AXES</td></tr>
<tr><td></td><td>Log(x/y)<0</td><td colspan="2">0≤Log(x/y)</td><td>Log(x/y)<0</td><td colspan="2">0≤Log(x/y)</td></tr>
<tr><td>$n_x < n_y$</td><td rowspan="3">1.0</td><td>1.4</td><td colspan="2">1.0</td><td>1.5</td><td colspan="2">1.3</td></tr>
<tr><td>$n_x = n_y$</td><td colspan="3">1.2</td><td colspan="3">1.3</td></tr>
<tr><td>$n_x > n_y$</td><td colspan="2">1.3</td><td>1.0</td><td colspan="2">1.3</td><td>1.5</td></tr>
</table>

Figure 7. Arranged Coefficient (using ϕ_{TE} as an example)

Structural Health Monitoring of the Support Structure of a Wind Turbine Using a Wireless Sensing System

Kung-Chun Lu [1] and Juin-Fu Chai [2]

盧恭君 [1]、柴駿甫 [2]

Abstract

Wind turbines depend heavily on the success of their support structures to resist complicated environmental loading, especially offshore wind turbines. How to manage these wind turbines and monitor their structural safety has become an urgent and important issue today. To monitor the support structural safety of a wind turbine, a good understanding of the structural dynamic behaviors of wind turbines is a preliminary requirement. Due to the complicated dynamic behaviors of realistic wind turbines, which include the effects of the soil-structure interaction (SSI), the machine operation loading, the wind interaction, etc., both numerical model study and system identification are required to clarify these complicated structural behaviors.

In this study, a wireless sensing system, NTU-WSU, is installed in an onshore large wind turbine (GE 1.5MW) to collect the structural responses, and the system performance of the proposed NTU-WSU was also evaluated in this study. Three measurement layouts and two operational scenarios (operating and stop states of the wind turbine) are considered in this study to clarify the complicated structural dynamic behaviors. Two system identification approaches are adopted to extract and verify the dynamic structural features, namely the direct Fourier spectrum observation method (FFT) and frequency domain decomposition method (FDD).

Keywords: wind energy, structural health monitoring, wireless sensing, frequency domain decomposition.

Introduction

With the increasingly serious problem of energy shortage, the demand for renewable energy is increasing, and wind energy is gaining popularity as one of the most practical alternatives today. Currently, through the development of wind energy, the number of wind turbines is substantially increasing. In order to minimize the environmental impact and increase the power generating efficiency of wind turbines, the development of offshore wind farms is underway. A wind turbine depends heavily on the success of its support structure to resist complicated environmental loading, especially in the case of offshore wind turbines. How to manage these wind turbines and monitor their structural safety has become an urgent and important issue today. An integral Structural Health Monitoring System for offshore wind turbines was proposed by Rolfes et al. [1] and the concept of monitoring the structural safety of the support structure was also introduced. In a review of damage detection methods for wind turbine systems, Ciang et al. [2] provided the damage probability of each component of a wind turbine and reviewed several structural damage detection methods, especially for damage to the blade.

In order to monitor the structural safety of a wind turbine, scientists and engineers must have a good understanding of the dynamic structural behavior of wind turbines. The realistic dynamic behaviors of wind turbines are very complicated as they include the effects of soil-structure interaction (SSI), machine operation loading, wind interaction, etc. To clarify these complicated structural behaviors, both numerical model study and system identification on realistic

[1] Assistant Researcher, National Center for Research on Earthquake Engineering, kclu@narlabs.org.tw.

[2] Research Fellow, National Center for Research on Earthquake Engineering, chai@narlabs.org.tw

structural responses are necessary. An experimental and numerical investigation into the seismic response of wind turbines was presented by Prowell et al. [3], where a full scale shaking table test of a wind turbine was performed and both numerical study and system identification from the experiment were presented.

Traditionally, deploying a wired sensing system on a large-scale structure (bridge, dam, wind turbine, etc.) is expensive and constrained by the environment. To shorten the instrumentation time, reduce costs, and break through the environmental restraints, wireless sensing technology has been widely adopted in recent decades. A study on the structural monitoring of wind turbines using wireless sensor networks was presented by Swartz et al. [4], where a wireless sensing system was adapted to two wind turbines and dynamic features were roughly extracted in this experiment.

In this study, a wireless sensing system, NTU-WSU, which is proposed for civil structural vibration measurement, is installed on an onshore large wind turbine (GE 1.5MW) in Taiwan to collect the required structural response signals and demonstrate the system performance in this unique operational environment. The overview of NTU-WSU is presented in the literature. The dynamic features of the wind turbine, modal frequencies, and mode shapes are illustrated with two analysis techniques, Fourier spectrum observation and frequency domain decomposition [5].

Wireless Monitoring of Wind Turbine

To validate the proposed wireless sensing system (NTU-WSU) for applicability to wind turbines, this study implements the NTU-WSU system to measure the structural vibration responses of a large onshore wind turbine. Moreover, the behavior of the support structure of wind turbines could be realized by utilizing well-developed system identification techniques to extract the structural dynamic features. In this study, one of the onshore wind turbines (GE 1.5MW) in Taiwan is temporarily considered as the test bench for evaluating the applicability of the wireless sensing system in the structural monitoring of the support structure of wind turbines. The support structure of this onshore wind turbine is a 68-meter high tower with a gravity type foundation. The wireless sensing system, monitoring scenarios, sensor instrumentation, and signal analysis results are introduced in the following sections.

Wireless sensing system (NTU-WSU)

In this study, the wireless sensing system (NTU-WSU), developed by NCREE and NTU, and the high sensitivity velocity meter (VSE-15D1), designed by Tokyo Sokushin Co., Ltd., are adopted as the structural monitoring system for the wind turbine in order to prevent difficulties in sensor wiring and layout in the support structure of the wind turbine.

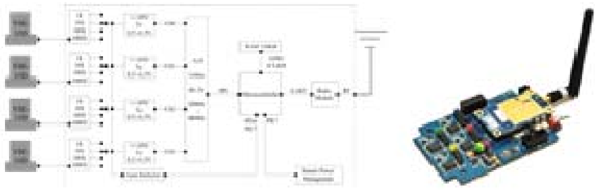

Figure 1 NTU-WSU architecture and photo

NTU-WSU inherited the main architectural design from the Wireless Modular Monitoring System (WiMMS): an 8-bit RISC microcontroller-based embedded system with 128kB external SRAM; 4-channel, 16-bit Analog-to-Digital Converter (ADC); and a wireless module. The 8-bit RISC microcontroller, ATmega128, controls the peripheral devices of the wireless sensing unit and handles the computation of data pre-processing. The external SRAM, CY62128, buffers the sampled row data and the variables that are generated by the analysis program, with a maximum buffered data length of 64k points (unsigned short). The 16-bit Analog-to-Digital Converter, ADS8341EB, converts the analog voltage signal to discrete digital row data. Two different proposed wireless modules, 9XTend and 24XStream, are compatible with NTU-WSU and create the data linkage between the wireless sensor network and the measurement system. The basic architecture of NTU-WSU is shown in Figure 1.

Based on this architecture, monitoring of the ambient structural responses is additionally considered in NTU-WSU. For sensor signal sampling, NTU-WSU provides two signal adjustment stages. The first stage is an amplifying signal with optimal pre-amplifying gain and the second stage is a scaling and shifting stage to convert the signal into the sampling range of ADC. There are four sensor input channels in the wireless sensing unit and all of them have a programmable gain amplifier (PGA204) to pre-amplify the sensor signal and are controlled by the microcontroller (ATmega128). Another improvement on the signal sampling of NTU-WSU is the oversampling process. This process achieves the ADC sampling with a rare high speed (limited by the performance of ADS8341EB and is about 100kHz) and downs the sample to the configured sampling rate (Fs). The oversampling process has three advantages for signal sampling: avoiding aliasing, improving resolution, and reducing noise [15]. NTU-WSU provides five different sampling rates, Fs, (50, 100, 200, 500, 10k Hz). When the oversampling function is achieved, the oversampling time is 128 for 50Hz, 64 for 100Hz, 32 for 200Hz, 16 for 500Hz, and 1 for 10kHz. The oversampling process is shown in Figure 2.

The NTU-WSU is compatible with two different wireless modules, Digi 9XTend and 24XStream. The 9XTend is operated in 900 MHz; 24XSream is operated in 2.4 GHz. By the selection of the wireless module, the NTU-WSU can prevent the busy frequency band of RF in the test environment.

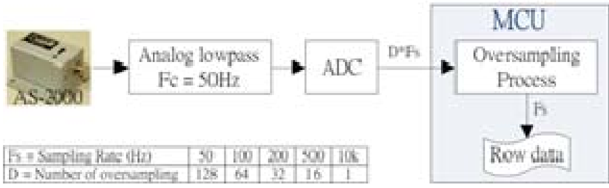

Figure 2 The oversampling process of Sensor Node.

Not only is the data rate and communication range of the 9XTend module is better than the 24XStream, but the power consumption of the 9XTend is also larger than 24XStream. NTU-WSU can adopt a suitable wireless module to match the application requirements of different structural monitoring scenarios.

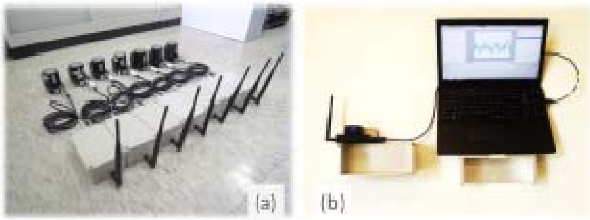

Figure3 (a) The calibration of wireless sensors. (b) The server and wireless receiver of wireless sensors

The entire wireless sensing system still requires a laptop as the server; the server provides data storage, signal analyzing, and sensor management. The entire wireless sensing system must make sure that the sensitivities of all sensors in this system are calibrated. To perform this calibration, all sensors are co-located and recorded at the same time segment and the sensitivities are evaluated through the comparison of the signals of different sensors. Figure 3(a) shows the calibration procedures for the wireless sensing system. Figure 3(b) shows the server of the wireless sensing system, which includes the laptop and wireless receiver.

Wind turbine instrumentations

In this study, the measurement target is the support structure of a GE 1.5MW onshore wind turbine, which consists of circular hollow sections and is 68 meters in height. Due to the geometric symmetry of the support structure and the eccentric loading of tower-induced torsional responses, the structural behaviors are complicated, which renders them difficult to present in two-dimensional space (XZ, YZ plane). Therefore, three-dimensional structural responses are required to perform the analysis of system identification. Each measurement point is installed with one set of three dimensional velocity meters, which consist of three uniaxial velocity meters (VSE-15D1).

To investigate the soil structure interactions between the tower foundation and soil, the responses of the free-field and tower foundation are required to collect the features of soil structure effect. The measurement point U3, Unit No.3 of the wireless sensing system, is used to measure the free-field ground motions and was located in the center of the grass 100 meters away from the tower. Moreover, to obtain the structural behaviors of the gravity type foundation of the wind turbine in this study, U4 and U5 were installed on symmetrical points of the circular foundation plate. Duplicated measurement points on a cross-section is necessary to obtain a good understanding of the vibration motion of the cross-section and to realize the minimum requirement on the sensor layout in a cross-section. The velocity meter (VSE-15D1) is expensive (about US$5000) and the number of VSE-15D1 is limited in the wireless sensing system. Therefore, to obtain the complete structural responses based on these constraints, the most effective measuring arrangement in this study includes three types of sensor layouts (Case1 - Case3). Figure 4 is the schematic layout of Case1 - Case3 and the details are as follows:

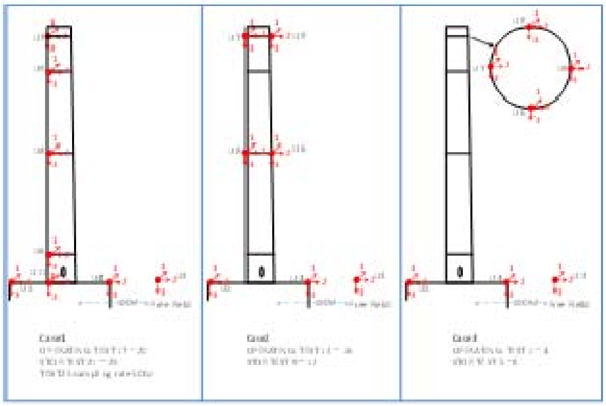
Figure 4 The arrangement of sensors on the wind turbine tower

- Case1: The vibration signal measurement from the elevation view. Five different elevations are picked to locate the sensors on the tower as equally spaced as possible. By observing the measured responses of these elevation sensors, the three primary mode shapes of the support structure could be illustrated in elevation view.
- Case2: The complex motions of the wind turbine must be well addressed. Therefore, torsion effects are considered as well as two horizontal directions and one vertical direction. As a result, the cross sections of the top and middle elevations of the tower are chosen as the observation targets. The sensors are arranged on each cross section symmetrically. The entire 3D motion of the tower is well illustrated by the six sensors.
- Case3: As the assembly mass of the wind power generator is almost the same as the tower, the wind turbine model can be roughly simplified to a single circular hollow column with an eccentric point mass on the top and six degrees of freedom (x, y, z, ϴx, ϴy, ϴz) are considered in the point

mass. To illustrate all motions of the point mass, there are four measurement points on the top of the tower.

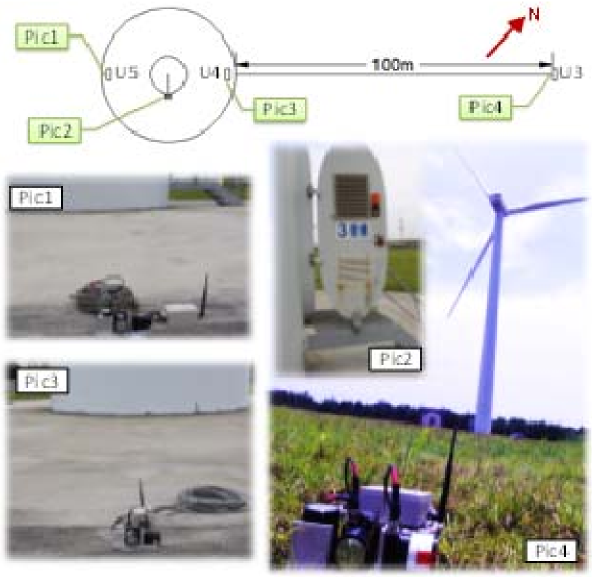

Figure 5 Photos of measuring equipment: outside the tower, near foundation, and in the free-field

Both the parked and operating conditions of the wind turbine are considered in this study. For the parked condition, the structural responses are mainly induced by light disturbances in the environment, which are not so complicated. Therefore, these structural ambient responses could be utilized to conceptualize the dynamic features of the support structure of the wind turbine. However, under operating conditions, the responses of the wind turbine contain a great number of other disturbances, such as the machinery vibration of the power generator, aerodynamics, and the soil-structure interaction under large deformation in the foundation. Therefore, the responses under the operating conditions contain a large amount of information that could be used to analyze many interactions between the foundation and other forcing effects. To obtain enough data for the follow-up analysis, there were 4 tests in each instrumentation case, and each test measured 1-minute response histories with a 200 Hz sampling rate.

The measurement equipment is shown in Figure 5 and Figure 6. Two symmetrical positions for measuring are chosen on the gravity type foundation. The 3-direction velocity meter is adhered to the foundation by gypsum. For the free-field sensor, the velocity meter is installed on the top of a short pile, which is embedded into the soil. A laptop functions as the server of the wireless sensing system and is installed at the bottom of the inner-side of the circular hollow tower. The door of the manhole is open to ensure the communication performance of the wireless sensing system. The instrumentation of Case3 for measurement at the top of the tower is shown in Figure 6(a). Figure 6(b) shows that the velocity meter in the tower is fixed to an aluminum box, which is magnetic adsorption for the inner surface of the tower.

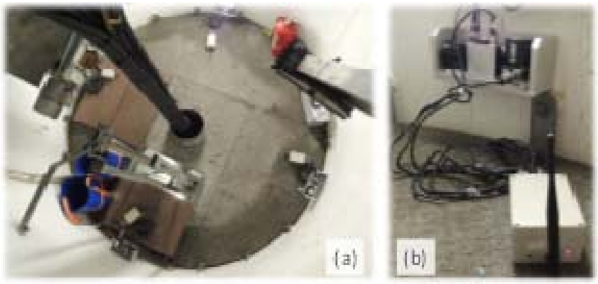

Figure 6 Photos of measuring equipment (a) inside the tower and (b) the fixing of the micro-vibro-meter

Results and Conclusions

The structural responses in the parked condition are analyzed by the Direct FFT and FDD methods, and the results are shown in Figure 7 and Figure 8. Two featured frequencies can be observed from these two methods. The first two mode shapes captured are in good agreement with the concept of structural dynamics.

The frequency characteristics and mode shapes of the results from these two methods were found to be highly congruent with each other, which means that the primary modal features have been captured successfully.

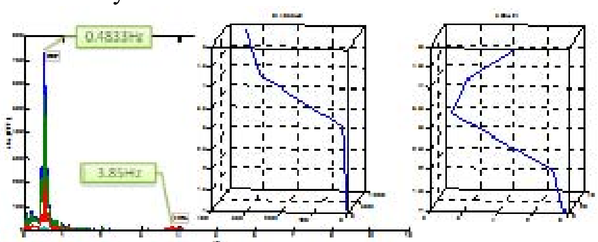

Figure 7 The analysis result of the wind turbine on the parked condition via Direct FFT

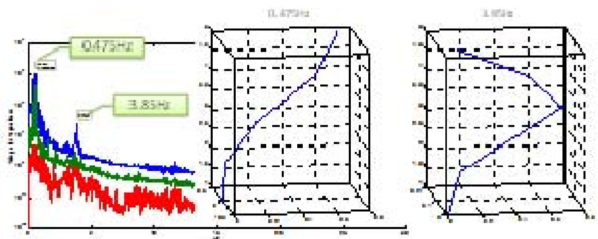

Figure 8 The analysis result of the wind turbine on the parked condition via FDD

References

K-C Lu*, H-C Peng, Y-Shu K, July 8-11, 2014, ”Structural Health Monitoring of the support structure of wind turbine using wireless sensing system”, the 7th European Workshop on Structural Health Monitoring, Nantes, France

Two Novel Approaches toward the Reduction of False Alarms Due to Unknown Events in On-Site Earthquake Early Warning Systems

Ting-Yu Hsu[1], Rih-Teng Wu[2], and Kuo-Chun Chang[3]

許丁友 [1]、吳日騰 [2]、張國鎮 [3]

Abstract

An on-site earthquake early warning system can provide more lead-time at regions that are close to the epicenter of an earthquake since only the seismic information of a target site is required. The on-site system extracts some P-wave features from the first few seconds of the vertical ground acceleration of a single station. It then predicts the intensity of the forthcoming earthquake at the same station according to these features. However, the system may be triggered by some vibration signals that are not caused by an earthquake or by interference from electronic signals, which may consequently result in a false alarm. Thus, this study proposes two approaches to distinguish the vibration signals caused by non-earthquake events from those caused by earthquake events, based on Support Vector Classification and Singular Spectrum Analysis. The results indicate that both of the proposed approaches effectively reduce the possibility of false alarms caused by an unknown vibration event.

Keywords: Earthquake Early Warning System; Support Vector Classification; Singular Spectrum Analysis; Signal Processing.

Introduction

Over the last two decades, Earthquake Early Warning (EEW) techniques have emerged as a result of advances in digital seismology, communications, automatic processing, and the algorithms employed for the rapid estimation of earthquake parameters (Satriano et al., 2011). Based on the information requirements of these algorithms, EEW techniques can be divided into two groups, namely regional warning and on-site warning techniques. Generally, since regional warning leverages information from several stations next to the epicenter of an earthquake, the accuracy of the estimation of earthquake parameters using regional warning techniques is usually higher than that of on-site warning techniques. However, regional earthquake early warning systems are not suitable for Taiwan due to the fact that most destructive seismic hazards come from inland earthquakes. For regions that are close to the epicenter, where seismic intensity is usually much higher than regions outside, the lead-time provided by regional warnings before a destructive wave arrives can be null. On the other hand, on-site warning can provide more lead-time at the regions that are close to an epicenter since only the seismic information of the target site is required, and the intensity of the forthcoming earthquake is predicted by the extraction of some P-wave features from the first few seconds of the vertical ground acceleration of a single station. Therefore, the increase in accuracy of on-site warnings is one of the key advantages of improving the effectiveness of EEW techniques in Taiwan.

According to the alarm records of the EEW stations of the National Center for Research on Earthquake Engineering (NCREE), the present on-site warning system may be triggered by vibration signals that are not caused by an earthquake event, and thus may result in many false alarms at the stations. Therefore,

[1] Associate Research Fellow, National Center for Research on Earthquake Engineering, dysheu@ncree.narl.org.tw
[2] Research Assistant, National Center for Research on Earthquake Engineering, r01521250@ntu.edu.tw
[3] Director, National Center for Research on Earthquake Engineering, kcchang@narlabs.org.tw

distinguishing between an earthquake and a non-earthquake event becomes an important issue. One approach to solve this particular problem is by using two sensors installed at different locations to conduct a double check procedure before an alarm is launched. For instance, one sensor may be triggered due to the vibration caused by moving cars, but the system would launch the alarm only if the second sensor is also triggered. The problem, however, is that this "hardware" approach increases the cost and difficulty of installation and maintenance. In this study, another "software" approach, which is based on Support Vector Classification (SVC) and Singular Spectrum Analysis (SSA), is proposed. The advantage of the proposed approach is that the vibration signals caused by non-earthquake events can be distinguished from those caused by earthquake events using only the measured vibration signals. Hence, no additional sensors are necessary.

Earthquake and Non-Earthquake Database

The vibration data utilized in this study were obtained from the Taiwan Strong Motion Instrumentation Program (TSMIP) and earthquake early warning system (EEWS) on-site stations including Gang-Ping Elementary School, Nan-An Junior High School, Guang-Fu Elementary School, and Yu-Dong Junior High School. The TSMIP network has been maintained by the Central Weather Bureau (CWB) in Taiwan to collect high-quality instrumental recordings of strong ground motions caused by earthquakes around Taiwan. In database I, approximately 15-years of TSMIP data between 29 July 1992 and 31 December 2006 were employed. Some data were excluded as their lengths were less than three seconds or appeared to be incorrect signals. There were 89,433 available data records from TSMIP.

To determine whether or not particular vibration data that are observed from an on-site station are a result of an earthquake, the time at which the data are recorded is compared with the time recorded by the Central Weather Bureau Seismic Network (CWBSN), and the acceleration signal is examined. Since the locations of the on-site station and the CWBSN station are different, the two times at which the data are recorded are compared by compensating for the time difference due to the different distances from the epicenter to the two stations. If both times correspond to each other and the signal is similar to an earthquake, the corresponding data is then regarded as being that from an earthquake event. Note that it is likely that there are some local earthquake events that are not recorded by the CWBSN but recorded by an on-site station, as there are 110 CWBSN stations in Taiwan and most distances between CWBSN stations are larger than 10 kilometers. Further, it is possible that there are some vibration signals that are similar to earthquake events but are not caused by an earthquake, such as vibrations caused by passing trucks or people running. This study does not view those signals as earthquake events as it is impossible to ensure whether or not data so similar to an earthquake is in fact the result of an earthquake, and it would be time-consuming and subjective if those data are distinguished by human selection. As a result, the remaining data from the on-site stations were considered as "unknown" data. In database I, the number of on-site station earthquakes and unknown events (collected from year 2011 to 2013) was 1,191 and 9,323, respectively.

To further verify the feasibility of the proposed approaches, database II was introduced. It contained a sample of earthquake data recorded by TSMIP from 2007 to 2012, and the vibration data of the four on-site stations mentioned previously recorded from year 2013 to 2014. There were 3,950 available data records from TSMIP, whereas the number of on-site station earthquakes and unknown events was 263 and 1,287, respectively.

Methodology

The on-site EEW technique takes advantage of the different propagation velocities of P-waves and S-waves. In other words, the expected ground shaking dominated by an S-wave is estimated based on the early information recorded of a P-wave from a single station. This is usually accomplished through empirical regressions between the P-wave features extracted from the measurements during the first few seconds and the final earthquake intensity at the same site. Satriano et al. (2011) reviewed the concepts, methods, and physical backgrounds of EEWS's. The P-wave features used to estimate the final earthquake size were also summarized in the same paper. In this study, we use several integral quantities of P-wave features (Böse et al., 2012), which are extracted from the first three second interval of a P-wave signal ($t_p = 3(s)$), including the peak absolute value of velocity (P_v), peak absolute value of displacement (P_d), predominant period (τ_c), integral of absolute acceleration (IAA), integral of absolute velocity (IAV), integral of absolute displacement (IAD), peak value of acceleration times velocity (P_{av}), peak value of acceleration times displacement (P_{ad}), and peak value of velocity times displacement (P_{vd}). These P-wave features are used as the training inputs of the regression model.

To establish a regression model that considers multiple P-wave features, an artificial intelligence method was utilized. SVC, which is a supervised learning method based on statistical learning theory, is outstanding for solving the multivariate problem. Moreover, it is especially desirable for use due to several other advantages such as having no problems with local minima and reliability at underfitting, overfitting, and in high noise conditions. Owing to these merits, this paper employed C-SVC (Boser et al., 1992; Cortes and Vapnik, 1995) to solve the following primal problem in the analysis. To reduce computational time, this study chose three features from the nine features mentioned, consequently resulting in 84 ($C_3^9 = 84$) combinations. However, only the result of the 39th (P_d, IAA, P_{vd}) combination is shown in this report due to it showing the best performance.

In addition, SSA (Golyandina et al., 2001) is introduced to investigate the energy distribution within the decomposed vibration signals. The original vibration signal can be decomposed into dominant energy series and residual energy series. It has been found that the FFT peak frequency of the residual energy series of a typical unknown event lies within the high frequency range, whereas the FFT peak frequency of the residual energy series of a typical earthquake event lies within the low frequency range. Thus, this study applies FFT to the residual series derived from SSA, and classifies the event based on the FFT peak location. If the FFT peak location is within the low frequency range, then the event is classified as an earthquake event; if the FFT peak location is within the high frequency range, then the event is classified as a non-earthquake event. The frequency threshold of this SSA criterion is 35 Hz.

To summarize, this study proposes two approaches to determine whether or not an unknown vibration event is caused by an earthquake event. Fig. 1 illustrates the procedure of the first proposed approach (Approach I). Since there are some vibration signals recorded from an on-site station containing only frequency content higher than 50 Hz, these events can be excluded if the FFT peak frequency location is higher than 50 Hz. For the events whose FFT peak frequency is lower than 50 Hz, they are classified again by the established SVC model. The system returns to its normal operational state if the event is classified as a non-earthquake event. Meanwhile, the system predicts the intensity of the forthcoming earthquake if the event is classified as an earthquake event. In addition, Fig. 2 illustrates the procedure of the second proposed approach (Approach II). Approach II is similar to Approach I, with the exception that the SSA criterion deals with those events that are classified as non-earthquake events by the SVC model. The motivation for adding an SSA criterion into Approach II is to further improve the classification accuracy of earthquake events. This SSA criterion provides an additional method to correctly classify those earthquake events misclassified by the SVC model. Therefore, it is expected that the accuracy of Approach II will be higher than the accuracy of Approach I.

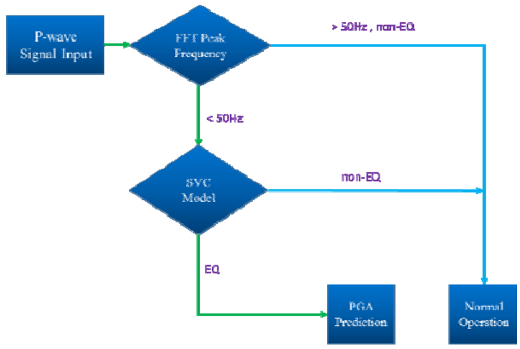

Fig. 1 Approach I

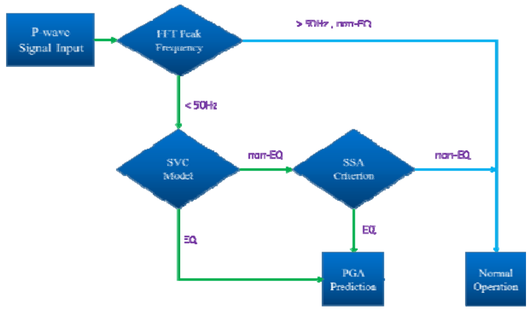

Fig. 2 Approach II

Results and Discussion

Fig. 3 and Fig. 4 respectively show the predicted PGA of on-site unknown events of database I for Approach I and Approach II by utilizing SVC model 39. Fig. 5 and Fig. 6 respectively show the predicted PGA of on-site unknown events of database II for Approach I and Approach II by utilizing SVC model 39. The vertical axis in the figures represents the predicted PGA of the event, and the horizontal axis denotes the actual PGA of the event. The numbers I, II…VII represent the earthquake intensity defined by the CWB. The blue cross marker represents each event, and a blue cross marker with a red circle marker indicates that the event is excluded before it enters the PGA prediction step. It is clear that almost all the unknown events with overestimated PGA values are excluded no matter whether we employed Approach I or Approach II, hence it greatly reduces the possibility of false alarms for on-site EEW systems. Moreover, it should be noted that both approaches obtained an accuracy higher than 99.64% for all the earthquake events with PGA values greater than 25 gal (not shown in this report).

Finally, although lead-time is a crucial aspect, the proposed approaches do not greatly reduce it. The conservative estimation of the additional computational time is 0.18(s), which arises mainly from the FFT and SSA algorithms, since it takes only 0.005(s) for the SVC model to classify the input vibration event. There is no extra time required for P-wave feature calculation as the present on-site warning system constantly calculates the features during its normal operational state.

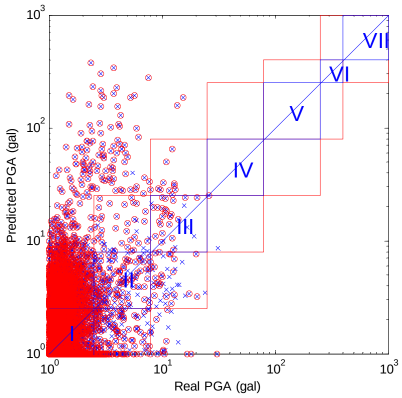

Fig. 3 PGA prediction for on-site unknown events (Approach I, SVC model 39, database I)

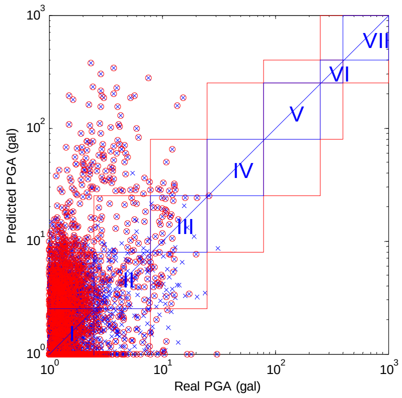

Fig. 4 PGA prediction for on-site unknown events (Approach II, SVC model 39, database I)

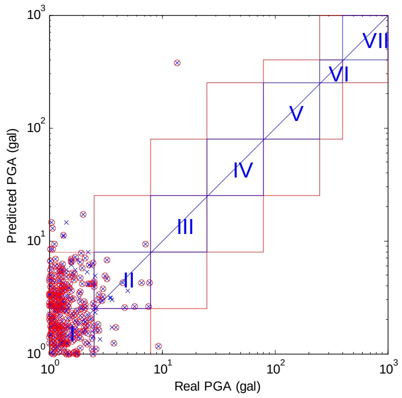

Fig. 5 PGA prediction for on-site unknown events (Approach I, SVC model 39, database II)

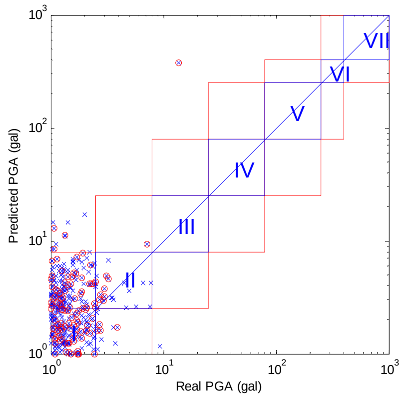

Fig. 6 PGA prediction for on-site unknown events (Approach II, SVC model 39, database II)

Conclusions

This study proposed two approaches to distinguish between the signals caused by earthquake and non-earthquake events. Both approaches effectively reduced the possibility of false alarms caused by unknown vibration events. In addition, an accuracy higher than 99.64% for all the earthquake events with PGA values greater than 25 gal was obtained by the use of the proposed two approaches. With regard to practical applications in the future, Approach II is recommended instead of Approach I because it has a higher accuracy for earthquake events, and the results from the two approaches regarding the reduction of false alarms are the same. Further, the proposed approach does not result in a great reduction of lead-time. Future studies are necessary to further verify the proposed method by using more data collected from an on-site station.

References

Boser, B. E., Guyon, I. and Vapnik, V. (1992), “A training algorithm for optimal margin classifiers”, Proceedings of the Fifth Annual Workshop on Computational Learning Theory, 144–152

Böse, M., Heaton, T. and Hauksson, E. (2012), ” Rapid Estimation of Earthquake Source and Ground-Motion Parameters for Earthquake Early Warning Using Data from a Single Three-Component Broadband or Strong-Motion Sensor”, Bulletin of the Seismological Society of America, v 102, n 2, 738-750

Golyandina N., Nekrutkin V. and Zhigljavsky A. (2001), Analysis of Time Series Structures, SSA and Related Techniques, Chapman and Hall/CRC

Satriano, C., Wu, Y.M., Zollo, A. and Kanamori, H. (2011), “Earthquake early warning: Concepts, methods and physical grounds,” Soil Dynamics and Earthquake Engineering, 31, 106–118

Vapnik, V.N. (1995), “The nature of statistical learning theory”, Springer-Verlag, Berlin

Seismic Assessment of Steel Liquid Storage Tanks

Gee-Yu Liu[1]

劉季宇[1]

Abstract

Steel tanks are widely employed in oil terminals, refineries, petrochemical installations, and many lifeline facilities. In areas of high seismicity, the safety of these tanks is crucial. In this study, a seismic assessment procedure for steel liquid storage tanks is presented. It is based upon "Appendix E: Seismic Design of Storage Tanks" in API 650 Welded Steel Tanks for Oil Storage (API, 2007). This study focuses on anchored, on-grade tanks, which are the most common type of tanks in Taiwan.

Keywords: steel tanks, seismic assessment, API 650

Introduction

Steel tanks are used extensively in oil terminals, refineries, and petrochemical factories all over the world for bulk storage of oil. They are also used for the storage of hazardous liquid materials, such as chemicals used for coagulation, sedimentation, and disinfection in water treatment plants. In areas of high seismicity, the safety of these steel liquid storage tanks is crucial. A rational approach to assess the seismic safety of such tanks is greatly needed.

Seismic Assessment Procedure

In this study, a seismic assessment procedure for steel liquid storage tanks is given, as depicted in Fig. 1. It is based upon "Appendix E: Seismic Design of Storage Tanks" in API 650 Welded Steel Tanks for Oil Storage (API, 2007), which provides on-grade welded steel tanks with minimum seismic requirements. Theoretically, it considers two response modes of a tank and its contents: impulsive and convective (Housner, 1963). This procedure applies to anchored steel tanks, which are the most commonly used variety, and is of high seismic concern in Taiwan. It is also incorporated with the ground motion specified in Taiwan Building Seismic Design Code (內政部營建署，2011).

API 650 classifies tanks into three Seismic User Groups (SUGs). SUG III tanks are those that provide service to facilities essential to the life and health of the public, or those that contain hazardous substances, to which it is greatly important to prevent public exposure. SUG II tanks are those that provide direct services to major facilities, or which store materials that may pose a public hazard and lack secondary controls. The rest belong to SUG I tanks.

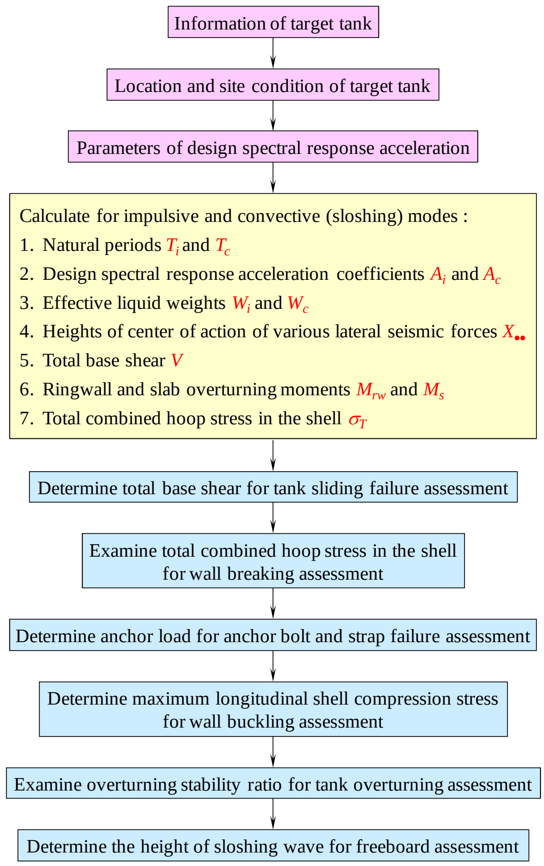

Fig. 1 Seismic assessment procedure for steel liquid storage tanks following API 650, App. E requirements.

[1] Associate Researcher, National Center for Research on Earthquake Engineering, karl@ncree.narl.org.tw

Table 1 Seismic analysis of steel tanks suggested by API 650 Appendix E

1. Determine T_i (s) and T_c (s), the natural periods of vibration for impulsive and convective (sloshing) modes of behavior of the liquid.

$$T_i = \frac{1}{\sqrt{2000}} \cdot \left(\frac{C_i H}{\sqrt{\frac{t_u}{D}}} \right) \cdot \sqrt{\frac{\rho}{E}} \qquad T_c = 2\pi \cdot \sqrt{\frac{D}{3.68g \cdot \tanh\left(\frac{3.68H}{D}\right)}}$$

where the coefficient C_i is a function of H/D depicted in the following chart.

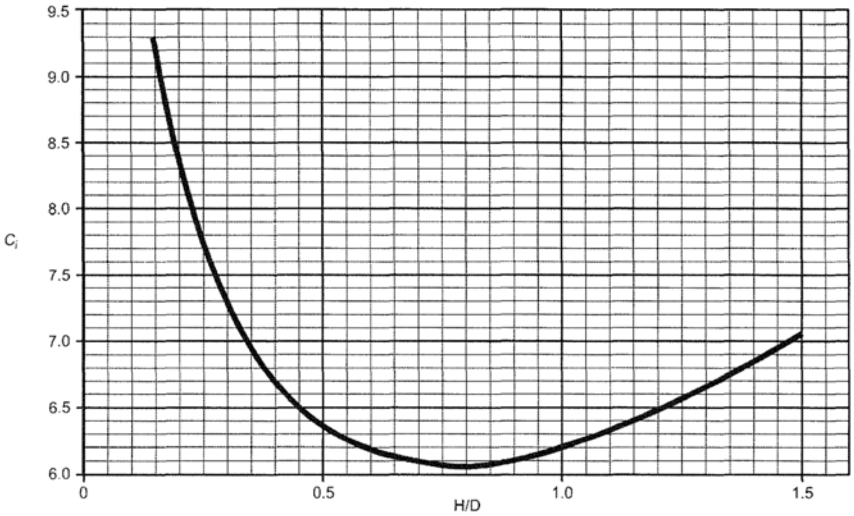

2. Determine A_i (g) and A_c (g), the impulsive and convective design spectral response acceleration coefficients (許琳青等，2010).

$$A_i = \left(\frac{I}{R_{wi}} \right) \cdot S_{aD}(T_i) \qquad A_c = K \cdot \left(\frac{I}{R_{wc}} \right) \cdot S_{aD}(T_c)$$

where I is set by Seismic User Group (SUG), and $K = 1.5$ unless otherwise specified. The values of force reduction coefficients R_{wi} and R_{wc} for the impulsive and convective modes using allowable stress design methods are 4 and 2, respectively, for mechanically-anchored tanks.

3. Determine V (N), the total base shear, from W_i (N) and W_c (N), the effective impulsive and convective portions of the liquid weight, respectively. Examine the possibility of tank sliding.

$$V = \sqrt{V_i^2 + V_c^2}$$

where

$$\begin{cases} V_i = A_i (W_s + W_r + W_f + W_i) \\ V_c = A_c W_c \end{cases} \quad W_i = \begin{cases} \dfrac{\tanh\left(0.866 \dfrac{D}{H}\right)}{0.866 \dfrac{D}{H}} \cdot W_p & D/H \geq 1.333 \\ \left(1.0 - 0.218 \dfrac{D}{H}\right) \cdot W_p & D/H < 1.333 \end{cases} \quad W_c = 0.230 \frac{D}{H} \cdot \tanh\left(\frac{3.67H}{D}\right) \cdot W_p$$

The calculated value of V should not exceed the sliding resistance V_s (N) calculated by:

$$V_s = \mu (W_s + W_r + W_f + W_p)(1.0 - 0.4A_v)$$

4. Determine the ringwall overturning moment M_{rw} (N-m) acting at the base of tank shell perimeter and the slab overturning moment M_s (N-m) used for slab and pile cap design.

$$M_{rw} = \sqrt{\left[A_i (W_i X_i + W_s X_s + W_r X_r)\right]^2 + \left[A_c (W_c X_c)\right]^2}$$

$$M_s = \sqrt{\left[A_i (W_i X_{is} + W_s X_s + W_r X_r)\right]^2 + \left[A_c (W_c X_{cs})\right]^2}$$

where $X_{\bullet}$ and $X_{\bullet\bullet}$ refer to the height from the bottom of the tank shell to the center of action of various lateral seismic forces from liquid, tank shell and roof.

$$X_i = \begin{cases} 0.375H & D/H \geq 1.333 \\ \left(0.5 - 0.094\dfrac{D}{H}\right)H & D/H < 1.333 \end{cases} \qquad X_c = \left[1.0 - \frac{\cosh\left(\dfrac{3.67H}{D}\right) - 1}{\dfrac{3.67H}{D} \cdot \sinh\left(\dfrac{3.67H}{D}\right)}\right]H$$

$$X_i = \begin{cases} 0.375\left[1.0 + 1.333\left(\dfrac{0.866\dfrac{D}{H}}{\tanh\left(0.866\dfrac{D}{H}\right)} - 1.0\right)\right]H & D/H \geq 1.333 \\ \left(0.5 + 0.060\dfrac{D}{H}\right)H & D/H < 1.333 \end{cases} \qquad X_{cs} = \left[1.0 - \frac{\cosh\left(\dfrac{3.67H}{D}\right) - 1.937}{\dfrac{3.67H}{D} \cdot \sinh\left(\dfrac{3.67H}{D}\right)}\right]H$$

5. Determine σ_T , the total combined hoop stress in the shell (MPa).

$$\sigma_T(\pm) = \frac{N_h \pm \sqrt{N_i^{\,2} + N_c^{\,2} + (A_v N_h)^2}}{t}$$

where the product hydrostatic membrane force N_h (N/mm), and the impulsive and convective hoop membrane forces N_i (N/mm) and N_c (N/mm) in tank shell, respectively, are calculated by:

$$N_h = \frac{9.81 \cdot GDY}{2}$$

$$N_i = \begin{cases} 8.48A_i GDH\left[\dfrac{Y}{H} - 0.5 \cdot \left(\dfrac{Y}{H}\right)^2\right] \cdot \tanh\left(0.866\dfrac{D}{H}\right) & D/H \geq 1.333 \\ 5.22A_i GD^2\left[\dfrac{Y}{0.75D} - 0.5 \cdot \left(\dfrac{Y}{0.75D}\right)^2\right] & D/H < 1.333 \quad \text{and} \quad Y < 0.75D \\ 2.6A_i GD^2 & D/H < 1.333 \quad \text{and} \quad Y \geq 0.75D \end{cases}$$

$$N_c = \frac{1.85A_c GD^2 \cdot \cosh\left[\dfrac{3.68(H - Y)}{D}\right]}{\cosh\left(\dfrac{3.68H}{D}\right)}$$

6. Examine P_{AB} , the anchor load (N).

$$P_{AB} = \left(\frac{1.273M_{rw}}{D^2} - w_t(1 - 0.4A_v)\right) \cdot \left(\frac{\pi D}{n_A}\right)$$

The calculated value of P_{AB} should not exceed 80% of the yield strength of anchor bolts.

7. Examine σ_c , the maximum longitudinal shell compression stress (MPa).

$$\sigma_c = \left(w_t(1 + 0.4A_v) + \frac{1.273M_{rw}}{D^2}\right) \cdot \frac{1}{1000t_s}$$

The calculated value of σ_c should not exceed the allowable longitudinal shell-membrane compression stress F_C (MPa) calculated by:

$$F_C = \begin{cases} 83 \cdot t_s / D & GHD^2/t^2 \geq 44 \\ 83 \cdot t_s /(2.5D) + 7.5\sqrt{GH} < F_{ty} & GHD^2/t^2 < 44 \end{cases}$$

8. Examine that the overturning stability ratio is 2.0 or greater.

$$\frac{0.5D \cdot (W_p + W_f + W_T + W_{fd} + W_g)}{M_s} \geq 2.0$$

9. Determine δ_s , the height (mm) of sloshing wave above the product design height. Examine the sufficiency of tank freeboard to accommodate the calculated value of δ_s .

$$\delta_s = 0.5DA_f$$ where $$A_f = \begin{cases} KS_{D1}I \cdot \left(\dfrac{1}{T_c}\right) & T_c \le 4 \\ KS_{D1}I \cdot \left(\dfrac{4}{T_c^{\ 2}}\right) & T_c > 4 \end{cases} \qquad A_f = \begin{cases} KS_{D1} \cdot \left(\dfrac{1}{T_c}\right) & T_c \le T_L \\ KS_{D1} \cdot \left(\dfrac{T_L}{T_c^{\ 2}}\right) & T_c > T_L \end{cases}$$

Nomenclatures	
A_v : vertical earthquake acceleration coefficient (g), taken as $0.14S_{DS}$ or greater for the ASCE 7 method D : nominal tank diameter (m) E : elastic modulus of tank material (MPa) F_{ty} : yield strength of shell (MPa) G : product specific gravity g : acceleration due to gravity (m/sec^2) H : maximum design product level (m) I : importance factor coefficient; I = 1.0, 1.25 and 1.5 for SUG I, II and III, respectively K : coefficient for adjusting spectral acceleration (from 5 to 0.5% damping) n_A : number of anchors around the tank circumference $S_{aD}(T)$: design earthquake spectral response acceleration coefficient for structural period T S_{D1} : design (5% damped) spectral response acceleration parameter at one second S_{DS} : design (5% damped) spectral response acceleration parameter at short periods (0.2s)	T_L : regional-dependent transition period for longer period ground motion (s) t : thickness of shell ring under consideration (mm) t_s : thickness of bottom shell (mm) t_u : equivalent uniform thickness of tank shell (mm) W_f : weight of the tank bottom (N) W_{fd} : total weight of tank foundation (N) W_g : weight of soil over tank foundation footing (N) W_p : total weight of the tank contents (N) W_r : total weight of fixed tank roof (N) W_s : total weight of tank shell and appurtenances (N) W_T : total weight of tank shell, roof, framing, knuckles, product, bottom, attachments and appurtenances (N) w_t : tank and roof weight acting at base of shell (N/m) Y : distance from liquid surface to any point (positive down (m) μ : friction coefficient for tank sliding (max. 0.4) ρ : density of fluid (kg/m^3)

Examples of Tank Assessment

As water is crucial to sustaining life, the seismic safety of water supply facilities is a pivotal issue in urban earthquake hazard mitigation. Recently, the seismic assessments of two 300-ton steel chemical storage tanks of the Taipei Water Department (one in Zhitan and the other in Changxing water purification plants) have been completed by using the procedures mentioned above. Details of the assessment criteria, calculation and major findings may be found in the technical report. Accordingly, measures to enhance the tanks' seismic integrity and secure their seismic safety have been advised (臺北自來水事業處，2014).

Concluding Remarks

In this study, a seismic assessment procedure for steel liquid storage tanks has been presented. It is based upon API 650, Appendix E (API, 2007). It is focused on anchored on-grade tanks, which are the most commonly-used tanks in Taiwan. The current API 650 code revises the combination of impulsive and convective forces to use the SRSS (square root of the sum of the squares) method and includes minimum requirements for overturning stability, hydrodynamic hoop stresses, and freeboard. By using this procedure, two steel chemical storage tanks in water treatment plants have recently been assessed.

Acknowledgement

The research funding from the Taipei Water Department under Grant 10331102S15 is gratefully acknowledged.

References

API (American Petroleum Institute), 2007, "API 650 Welded Steel Tanks for Oil Storage," 11-th Ed.

Housner, G.W. 1963, "Dynamic Analysis of Fluids in Containers Subjected to Acceleration," Nuclear Reactors and Earthquakes, Appendix F, Report No. TID 7024, U.S. Atomic Energy Commission, Washington D.C.

內政部營建署，2011，「建築物耐震設計規範及解說」，台北。

許琳青、姚忠達、蔡吉仁、吳嘉偉、曹詩婷，2010，「工廠危險物品室內外儲槽場所之耐震設計可行性評估研究」，內政部消防署委託研究報告。

臺北自來水事業處，2014，「自來水水管橋、藥槽及配水池之耐震評估研究案」，研究報告，計畫編號 10331102S15，台北。

A New PGD Model for Bridge Damage Assessment

Chin-Hsun Yeh[1], Chi-Hao Lin[2], Cheng-Tao Yang[3], Lee-Hui, Huang[4]

葉錦勳 [1]、林祺皓 [2]、楊承道 [3]、黃李暉 [4]

Abstract

This report briefly describes a new Permanent Ground Displacements (PGD) model for seismic damage assessment of bridges. Based on the experience of the 921 earthquake disaster, it was found that PGD from fault rupture seriously impacts bridges. Therefore, the method of estimating PGD near fault rupture is an important component in seismic assessment of bridge damage. The model consists of three formulas as follows: (1) Permanent Ground Displacements, (2) Encounter Probability, and (3) Relation Position. The new model has been implemented as a new kernel assessment module for the sub-system of Taiwan Earthquake Loss Estimation System (T-Highway) in 2014. For the verification of the PGD model, the T-Highway has been adopted to assess bridge damage in the Chi-Chi earthquake scenario. The new T-Highway has also been applied to the seismic risk and retrofit order of the highway bridges. Administration is progressing retrofit projects in order to upgrade the seismic capacity of highway bridges. The retrofit projects include 1169 bridges in 2014. This report will first describe the model and the validation of it. Finally, applications of the model will be described.

Keywords: Seismic Damage Assessment, Fault Rupture Phenomenon, Permanent Ground Displacements

Introduction

In order to fully utilize the local inventory data, analysis models, and parameters, the National Center for Research on Earthquake Engineering (NCREE) has developed an earthquake loss estimation system in Taiwan, named "Taiwan Earthquake Loss Estimation System (TELES)", since 2003. The system simulates the violence of ground shaking, the severity of structural and non-structural damage, the number of casualties, the lifeline service disruption, and economic and social losses caused by earthquakes. It can provide a variety of seismic damage assessments. The assessment results enable users to develop plans and strategies for earthquake hazard mitigation. In recent years, in order to stratify various objects, TELES has been customized for multiple independent subsystems, such as T-Highway and T-Water (for the water system).

T-Highway was built for seismic damage assessment of highway bridges. Fig. 1 shows the flow chart of the seismic damage assessment for bridges. The seismic hazard of bridges comes from ground motion and ground deformations. The vibration intensity is usually calculated based on the magnitude of the earthquake event, the shortest distance from the site to the fault rupture surface (or line), and soil properties, namely the vibration attenuation law and the correction mode of the site effect. The vibration intensity can be assessed by the peak ground acceleration (PGA) or structural response spectrum of acceleration (Sa). The permanent ground displacements (PGD) include soil liquefaction, landslides, and fault ruptures.

Based on the experience of the 921 earthquake disaster, the most serious damage to bridges was located on the zone of fault rupture or on the hanging wall. The PGD from fault rupture seriously impacts bridges. Therefore, the method of estimating PGD near fault rupture is an important component of seismic assessment of bridge damage. The model consists of three formulas as follows: (1) Permanent

[1] Research Fellow and Division Manager, National Center for Research on Earthquake Engineering, chyeh@ncree.narl.org.tw
[2] Assistant Research Fellow, National Center for Research on Earthquake Engineering, chihao@ncree.narl.org.tw
[3] Associate Research Fellow, National Center for Research on Earthquake Engineering, ctyang@ncree.narl.org.tw
[4] Assistant Research Fellow, National Center for Research on Earthquake Engineering,lhhuang@ncree.narl.org.tw

Ground Displacements, (2) Encounter Probability, and (3) Relation Position. In order to conduct more realistic descriptions of the fault rupture phenomenon and its impact on structures, this study has modified the estimation formula of permanent ground displacement based on research by Wells and Coppersmith (1994) and Yeh et al. (2005). To account for the uncertainty of fault rupture, the encounter probability between fault rupture and bridge structures was also adopted. Finally, the relation position between bridges and the fault has been modified to represent the impact of fault rupture to long span bridges. The new PGD model will be detailed in the next section.

The new model has been implemented as a new kernel assessment module for TELES in 2014. T-Highway has been selected for bridge damage assessment in the Chi-Chi earthquake scenario for the verification of the PGD model. T-Highway was verified against the disaster record of the Chi-Chi earthquake and consequently found to be an accurate assessment of bridge damage. The comparison between the disaster record and T-Highway simulation is expounded in the model verification section.

The T-Highway coupled with the new PGD model feature has also been applied in developing retrofit plans of highway bridges in 2014. In order to upgrade the seismic capacity of highway bridges, the Taiwan Area National Freeway Bureau (NFB) has been progressing highway bridges retrofit projects. The progress of the retrofit projects consist of three phases, the first two of which have been completed and the third has been entrusted to T.Y.Lin International Group (T.Y. Lin) in 2014. There were 1169 highway bridges in the phase. T-Highway was applied to the seismic risk and retrofit order of the bridges. The application will also be illustrated.

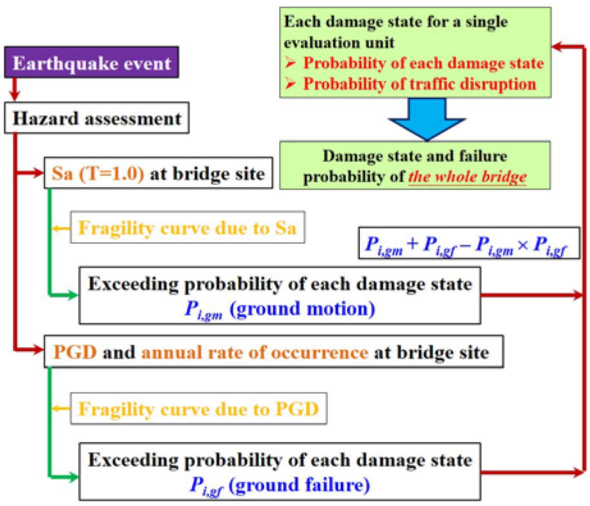

Fig.1 Flow chart of the earthquake damage assessment for a highway bridge

PGD Model

Permanent Ground Displacements

According to the research by Wells and Coppersmith (1994) and Yeh et al. (2005), PGD was estimated by Eq. (1).

$$PGD=\begin{cases} p\cdot f_H\cdot D\cdot\exp\left[-\dfrac{d}{d_{sr}\cdot f_H}\right] & \text{on hanging wall} \\ p\cdot f_F\cdot D\cdot\exp\left[-\dfrac{d}{d_{sr}\cdot f_F}\right] & \text{on footwall} \end{cases} \tag{1}$$

To make a more realistic description of the fault rupture phenomenon and its impact on the bridge structure, Eq. (1) was modified into Eq. (2).

$$PGD=\begin{cases} \dfrac{1000}{d_{sr}}\cdot p\cdot f_H\cdot D\cdot\exp\left[-\dfrac{d}{d_{sr}\cdot f_H}\right] & \text{on hanging wall} \\ \dfrac{1000}{d_{sr}}\cdot p\cdot f_F\cdot D\cdot\exp\left[-\dfrac{d}{d_{sr}\cdot f_F}\right] & \text{on footwall} \end{cases} \tag{2}$$

where f_H and f_F are the adjustment factors located on the hanging wall and footwall, respectively, and can be expressed as $f_F=|\alpha|/180$ and $f_H=1-f_F$; α is the angle of the fault rupture surface; d_{sr} is the depth from the top of the seismogenic zone to the ground surface; D is the maximum slip on both sides of the fault; and d is the shortest distance between the rupture surface to the bridge site. The unit of D, d_{sr}, and d is meters. d_{sr} is usually 2-5 kilometers, so that the PGD has a dramatic change on the fault rupture surface and both its sides.

Encounter Probability

To consider the non-uniform or continuous ruptured phenomenon of the ground surface, the probability p of structures being located on the rupture line is assumed to be related to the shortest distance d. The probability p can be expressed as follows:

$$p=0.7\cdot\exp[\frac{-d}{2000}] \tag{3}$$

where d is measured in meters. The constant 0.7 in Eq. (3) reflects the uncertainty of the fault line (plane) position. The exceedance probability of the different damage states of structures due to a fault rupture should be multiplied by p.

The Relation Position between Bridges and the Fault

In literature, the center point of the bridge was used to estimate the shortest distance d_c between the rupture surface and the bridge site. However, when the highway bridge is long, this value cannot accurately reflect the damage situation of the other parts since only the center point of the bridge is used to estimate the PGD. To overcome this limitation in this study, the main azimuth angle φ of the bridge is defined by using both ends of the bridge. Using the fault strike θ, the included angle |φ-θ| can be calculated. Referring to Fig. 2, if d_c has been calculated, according to the bridge length l, the included angle |φ-θ|, and the inclination angle α of the fault plane, the shortest distance d_e from an endpoint of the bridge to the rupture surface can be estimated by the following equation:

$$d_e = \begin{cases} \max\left(0, d_c - 0.5 \cdot l \cdot \sin\left|\varphi - \theta\right| \cdot \sin\alpha\right) & \textit{on hanging wall} \\ \max\left(0, d_c - 0.5 \cdot l \cdot \sin\left|\varphi - \theta\right|\right) & \textit{on footwall} \end{cases} \tag{4}$$

As d_e is less than 10 meters, the bridge may span the fault and its permanent ground displacement D. When d_e is substituted into Eq. (2), a more accurate estimation of the damage probability of PGD caused by the fault rupture can be achieved.

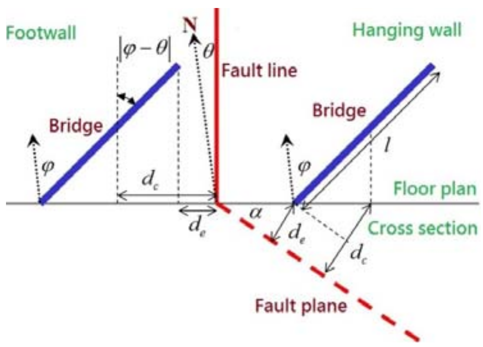

Fig.2 Schematic diagram of the relative position of the bridge and the fault line (and rupture surface)

Model Verification

For verification of the PGD model, the disaster record of the Chi-Chi earthquake was compared to the simulation result of T-Highway subsystem. The earthquake (7.3 M_s or 7.6 - 7.7 M_w) is Taiwan's worst disaster in recent years. Many bridges near the epicenter were damaged. Damage states are divided into five damage degrees as follow: no damage (D1), slight damage (D2), moderate damage (D3), extensive damage (D4), and complete damage (D5). The 26 damaged bridges, which are shown in Fig. 3, are representative of the damage caused by the earthquake. Fig. 4 also shows the simulation result of T-Highway.

As listed in Table 1, the assessment of T-Highway with the PGD model is compared with site survey results. The damage states of the assessment and the site survey are much close. There are 24 bridges that the difference between the assessment and the site survey is in one damage degree. The other 2 bridges have the difference of two damage degrees. It is worth noting that one of the 2-damage-degrees bridges was actually under construction when the earthquake occurred. According to the verification, coupling T-Highway with the new PGD model should be able to deliver a more reasonable damage assessment of bridges.

Table1. The damage status of 26 typical bridges

Damage state	D5	D4	D3	D2	D1	Total
Site survey	10	7	3	6	0	26
T-Highway	8	5	5	5	3	26

Application

In order to improve the seismic capacity of highway bridges, the Taiwan Area National Freeway Bureau (NFB) is progressing retrofit projects of highway bridges. The process of the retrofit projects consists of three phases. In 2014, the last phase involved 1169 bridges and used T-Highway in the assessment of the seismic risk and retrofit order of the bridges. The seismic loss of bridges considers direct and indirect losses. The direct losses arise from the expected cost to repair damaged bridges in the event of an earthquake. Indirect losses arise from the cost of extra detour time and distance due to damaged bridges.

The seismic risk of highway bridges could be estimated based on the annual average loss. Additionally, six factors have also been considered for ranking the retrofit order among the highway sections. They are: 1. Structural Risk, 2. Benefit, 3. Preliminary Evaluation, 4. Detour cost, 5. Economy lost, and 6. Overpass. The first three factors consider structural vulnerability and the others consider social and economic impacts. The comparison between the annual average losses of highway bridges after retrofit with those without retrofit could be an influential factor in the decision-making process behind the retrofit order of the bridges. The result of the seismic risk assessment is shown in Table 2. It indicates that the seismic loss decreased after retrofit.

Table 2. Highway Bridges Annual Average Loss

	Direct	**Indirect**	**Total**
Before retrofit	430,662	345,971	776,632
After retrofit	51,985	77,644	129,630

Concluding Remarks

In this study, a model describing the fault rupture impact on bridges is proposed. The model is a very important module of T-Highway for estimating seismic damage of bridges near or across fault rupture. An application based on the last retrofit phase in 2014 shows that the development of the subsystem is suitable for practical applications.

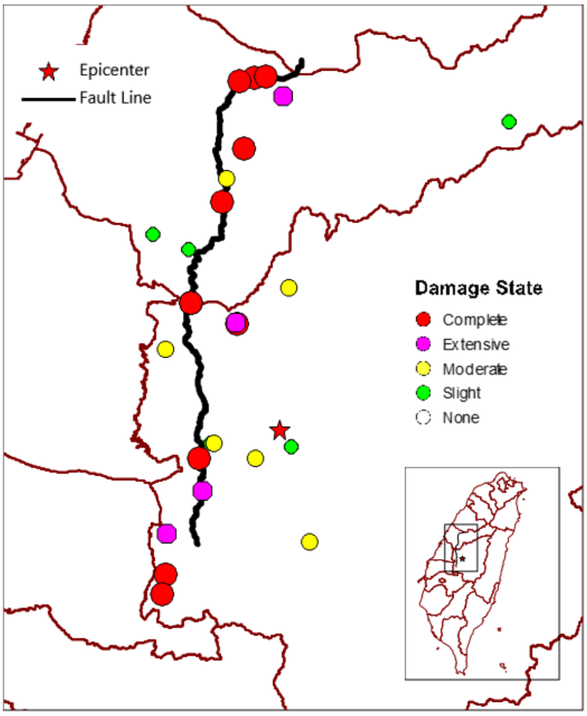

Fig3. The site survey result on Chi-Chi earthquake

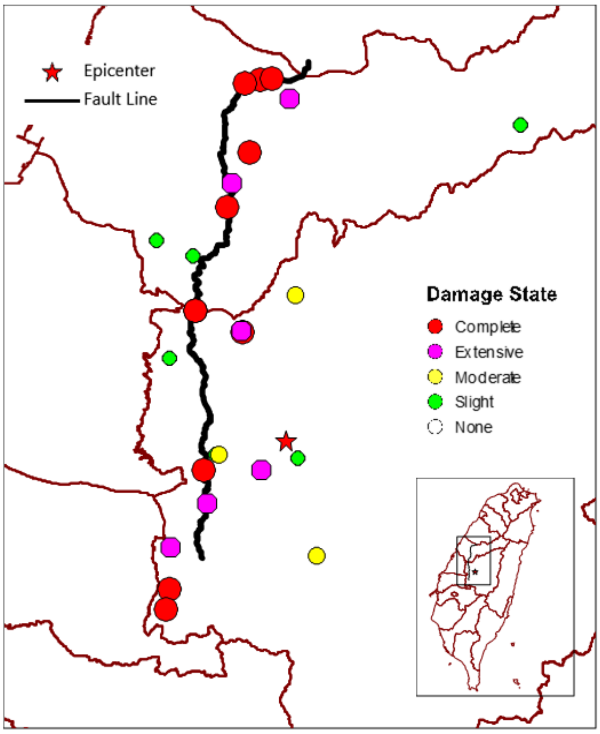

Fig4. The simulation result of T-Highway

References

Cornell, C. A. (1968), "Engineering Seismic Analysis", Bull. Seism. Soc. Am., 58, pp. 1583-1606.

Wells, D. L. and Coppersmith, K. J. (1994), "New Empirical Relationships Among Magnitude, Rupture Length, Rupture Width, and Surface Displacement", Bulletin of the Seismological Society of America, Vol. 84, pp. 974-1002.

ATC-10 (1996), "An Investigation of the correlation between earthquake ground motion and building performance", Applied Technology Council.

Atkinson, G. M. and Boore, D. M. (1997), "Some comparisons between recent ground motion relations", Seism. Res. Lett., 68, 1, pp. 24-40.

Yeh, C.-H. (2003), "Taiwan Earthquake Loss Estimation System – TELES", Technical Report NCREE 03-002, National Center for Research on Earthquake Engineering, Taipei (in Chinese).

Yeh, C.-H. , Hung, L.-L., Wen, Q.-L. (2005), "Seismic Damage Assessment of Gas System and Its Applications", Technical Report NCREE-05-021, National Center for Research on Earthquake Engineering, Taipei. (in Chinese)

Jean, W.-Y., Chang, Y.-W., Wen, K.-L., Loh, C.-H. (2006), "Early Estimation of Seismic Hazard for Strong Earthquakes in Taiwan", Natural Hazards, 37(1–2):39-53

Chang, Y.-W., Jean, W.-Y., Wen, K.-L., Loh, C.-H. (2007), "The Application of Time-Predictable Characteristic Earthquake Model for Evaluation of Design Earthquake in Taiwan", The Proceedings of 10th International Conference on Applications of Statistics and Probability in Civil Engineering(ICASP10), Paper No.CH072 (CD-ROM), Japan.

Yeh, C.-H., Lin, C.-H., Huang, L.-H., Liu, G.-Y., Yang, C.-T. (2014), "The Earthquake Loss Assessment for Freeway Bridges and its Applications", Workshop on Seismic Assessment and Retrofit Techniques for Freeway Bridges.

Preliminary Seismic Evaluation of School Building with RC Jacketing

Sheng-Hsueh Lin[1], Yao-Sheng Yang[2] and Lap-Loi Chung[3]

林聖學[1]、楊耀昇[2]、鍾立來[3]

Abstract

After the 921 Earthquake, the required seismic capacity in the design codes was heightened significantly, especially for primary and secondary school buildings. School buildings protect the lives of children and serve as emergency shelters after earthquakes, and so we must consider the issue of the seismic performance of school buildings. An overall evaluation of primary and secondary school buildings needs to be performed as soon as possible. Retrofitting school buildings with RC column jacketing is commonly performed. After retrofitting, engineers can use methods like preliminary seismic evaluation to quickly calculate the seismic capacity. In this paper, we use a typical school building to develop a preliminary seismic evaluation method for RC jacketing and compare the results with those obtained experimentally. The estimates using the proposed method are conservative.

Keywords: RC jacketing, preliminary seismic evaluation, school buildings, retrofitting

Introduction

In this paper, we want to use the spirits of the method of the preliminary seismic evaluation of a school building to establish the preliminary seismic evaluation of a school building with RC jacketing. After retrofitting, engineers can use this method like preliminary seismic evaluation to quickly calculate the seismic capacity. Then we use a typical school building to develop a preliminary seismic evaluation method for RC jacketing and compare the results with those obtained experimentally.

Lateral Strength of RC Jacket per Unit Cross-Sectional Area

We will establish the lateral strength of a reinforced concrete (RC) jacket per unit of the cross-sectional area based on a column line of a typical school building before and after retrofitting with RC jacketing.

(1) Column line before retrofit

Figure 1 shows the column line of typical school building. It is a two-floor column line. The floor height is 3.40 m. The reinforcement of the 30×50-cm column consists of four No.7 and eight No.6 longitudinal bars and No.3 stirrup spacing at 25 cm. The reinforcement of the 24×60-cm beam consists of four No.6 longitudinal bars on the top, two No.6 longitudinal bars on the bottom, and No.3 stirrup spacing at 25 cm (Fig. 2). The compressive strength of concrete is $f_c' = 160\ kgf/cm^2$. The yielding strengths of both the longitudinal bars and stirrup are $f_y = 2800\ kgf/cm^2$.

The structural systems of existing typical school buildings are usually weak-column strong-beam type. The lateral strength of a column is:

$$V_C = \frac{2M_{nC}}{H_C} \tag{1}$$

where M_{nC} is the nominal strength of the column ends and H_C is the clear height of the column. According to the above equation, the lateral strength of a typical column line is calculated to be $V_C = 10.062\ tf$.

[1] Graduate Student, Department of Civil Engineering, NTU
[2] Assistant Research Fellow, NCREE
[3] Research Fellow, NCREE and Professor, NTU

(2) Column line after retrofit

The reinforcement of the 60×80-cm retrofitted column consists of twelve No.6 longitudinal bars and No.3 stirrup spacing at 10 cm (Fig 2), in addition to the reinforcement already existing before the retrofit. The compressive strength of concrete is $f_c' = 280\,kgf/cm^2$. The yielding strengths of longitudinal bars and stirrup are $f_y = 4200\,kgf/cm^2$ and $f_y = 2800\,kgfcm^2$, respectively. Using moment equilibrium and taking moment about the column bottom (Fig 3) we have:

$$\frac{1}{3}V_{CJ}h_{1F} + \frac{2}{3}V_{CJ}h_{2F} = M_{nRCJ} + 2\left(M_{nbR} + M_{nbL}\right) \quad (2)$$

Thus, we can calculate the lateral strength of the retrofitted column V_{CJ}:

$$V_{CJ} = \frac{3M_{nRCJ} + 6\left(M_{nbR} + M_{nbL}\right)}{h_{1F} + 2h_{2F}} \quad (3)$$

Then we can get the lateral strength of the RC jacket per unit of cross-sectional area τ_{RCJ}:

$$\tau_{RCJ} = \frac{V_{CJ} - V_C}{A_{RCJ}} \quad (4)$$

where A_{RCJ} is the area of jacket, in this case 3300 cm^2. The axial force on the column is $50\,tf$. Using sectional analysis, the column nominal moment is $M_{nRCJ} = 91.2386\,tf-m$, and the beam nominal moments are $M_{nbR} = 12.131\,tf-m$ and $M_{nbL} = 22.487\,tf-m$. The lateral strength of the RC jacket per unit of cross-sectional area is $\tau_{RCJ} = 5.53\,kgf/cm^2$.

Preliminary Seismic evaluation method of school building with RC jacketing

The base shear strength of a school building retrofitted with RC jacketing, called $V_{bs,R}$, is based on the preliminary seismic evaluation before retrofit and the installation of the RC jacket, and is expressed by:

$$V_{bs,R} = V_{bs} + \beta\left(\tau_{RCJ}A_{CJ}\right) \quad (5)$$

where V_{bs} is the base shear strength before retrofitting and A_{CJ} is the total cross-sectional area of the RC jacket.

Then we can calculate the ductility capacity R of a school building with RC jacketing as:

$$R = \frac{R_E V_{bs} + R_R\left(\tau_{RCJ}A_{CJ}\right)}{V_{bs,R}} \quad (6)$$

where V_{bs} is the base shear strength of the original school building; $R_E = 2.8$ is the ductility capacity of the original building; and $R_R = 4$ is the ductility capacity of the retrofitted column.

Comparison with Experimental Results

(1) Hou-jia Junior High School

We use the experimental results of a specimen replicating a building in Hou-jia Junior High School in a comparison with the preliminary evaluation results. The specimen was retrofitted with RC jacketing and subjected to a cyclic loading test. From the results of the experiment, we determined the base shear strength of the school building to be $V_{bs,EX} = 882.26\,kN = 89.93\,tf$ and the ductility capacity of the retrofitted building to be $R_{EX} = 6.14$ by the following equation:

$$\frac{1}{R_{EX}} = 1 - \sqrt{1 - \frac{2U_{V\Delta}\Delta_{RF,0.7V_{max}}}{0.7V_{bs,EX}\Delta_{RF,u}^2}} \quad (7)$$

where $U_{V\Delta}$ is the area under the capacity curve from zero roof displacement to the roof displacement corresponding to the base shear having decreased to 80% of the maximum; $\Delta_{RF,0.7V_{max}}$ is the roof displacement corresponding to the base shear having increased to 70% of the maximum; $V_{bs,EX}$ is the experimental base shear strength; and $\Delta_{RF,u}$ is the roof displacement corresponding to the base shear having decreased to 80% of the maximum.

From the preliminary evaluation, the base shear strength of the school building with RC jacketing was calculated to be $V_{bs,R} = 73.89\,tf$ (Equation 5). This is 87% of the experimental result. We also calculated the ductility capacity of the school building with RC jacketing to be $R = 3.704$ (Equation 6), which is 60.3% of the experimental result.

(2) Guan-miao Elementary School

A building in Guan-miao Elementary School was retrofitted with RC jacketing and subjected to the monotonic pushover test. From the experimental results, we can get the base shear strength of the school building to be $V_{bs,EX} = 279.766\,tf$ and the ductility capacity $R_{EX} = 9.748$. We also calculated the allowable ductility capacity of the school building to be $R_{a,EX} = 6.832$ by the following equation:

$$R_{a,EX} = 1 + \frac{R_{EX} - 1}{1.5} \quad (8)$$

Preliminary Seismic evaluation of Guan-miao Elementary School building with RC jacketing

(1) Base shear

On the first floor, the total cross-sectional areas of the classroom columns, partition columns and RC jackets were 12,000 cm^2, 2,880 cm^2 and 12,000 cm^2, respectively. Through the preliminary evaluation, we calculated the base shear strength of the retrofitted building to be $V_{bs,R} = 159.6\ tf$. This is 61.25% of the experimental result.

(2) Weight per unit of floor area

We used 800 kgf/m^2 as the weight per unit area of the roof, and 950 kgf/m^2 as the unit weight of the other floors in the preliminary evaluation of school building retrofitted with RC jacketing.

We calculated the weight of the roof floor of the Guan-miao school building to be 125.734 tf and the weight per unit floor area to be 727.632 kgf/m^2. The preliminary evaluation result is 109.9% of the actual. The weight of the second floor was 159.164 tf and the unit weight was 921.088 kgf/m^2. The preliminary evaluation result is 103.1% of the actual.

(3) Fundamental vibration period

From the test results, we calculated the period of the Guan-miao school building to be $T_{EX} = 0.230\ s$ by the following equation:

$$T_{EX} = 2\pi\sqrt{\frac{1.5\left(W_{RF} + 0.25W_{2F}\right)\Delta_{RF}}{1.25gV_{bs}}} \tag{9}$$

where W_{RF} is the weight of the roof floor and W_{2F} is the weight of the second floor.

Through preliminary evaluation, we estimated the period as $T = 0.3012\ s$ from the building seismic design code as follows:

$$T = 0.070h_n^{3/4} \tag{10}$$

where h_n is the height of the school building.

The preliminary evaluation result is 131% of the actual period.

(4) Allowable ductility capacity

The allowable ductility capacity obtained through preliminary evaluation of the Guan-miao school building was $R_a = 2.43$. This is 35.57% of the actual value $R_{a,EX} = 6.832$.

(5) Basic seismic performance

According to the seismic design code, the minimum level of the design seismic force V is:

$$V = \frac{S_{aD}I}{1.4\alpha_y F_u}W \tag{11}$$

We rearranged this equation to get the seismic capacity and demand ratio (CDR) as:

$$R_{CD} = \frac{C_s}{D_s} = \frac{1.4\alpha_y V}{S_{aD}IW / F_u} = \frac{V_{bs}}{S_{aD}IW / F_u} \geq 1 \tag{12}$$

where the seismic capacity is $C_s = 1.4\alpha_y V = V_{bs}$; and the seismic demand is $D_s = S_{aD}IW / F_u$.

The importance factor of an ordinary school building is $I = 1.25$. The building site is classified as the second site. The design horizontal acceleration response spectrum factor is $S_{aD} = 0.7$ as per the building seismic design code.

The earthquake reduction factor of a structural system is a function of the allowable ductility capacity and the fundamental vibration period.

$$F_u = \begin{cases} \sqrt{2R_a - 1} + \left(\sqrt{2R_a - 1} - 1\right)\dfrac{T - 0.2T_0^D}{0.2T_0^D}, & T \leq 0.2T_0^D \\ \sqrt{2R_a - 1}, & 0.2T_0^D \leq T \leq 0.6T_0^D \\ \sqrt{2R_a - 1} + \left(R_a - \sqrt{2R_a - 1}\right)\dfrac{T - 0.6T_0^D}{0.4T_0^D}, & 0.6T_0^D \leq T \leq T_0^D \\ R_a, & T_0^D \leq T \end{cases} \tag{14}$$

where T_0^D is the corner period between the short and mid-to-long periods. When T is longer, F_u is bigger and the force V decreases further. After substituting the relevant parameters into the above equation, we get $F_u = 3.559$.

In order to illustrate the results more clearly, we enlarged the capacity demand ratio 100 times. This results in a basic seismic performance of $E = 372$, where E is expressed by:

$$E = 100R_{CD} = 100\frac{V_{bs}F_u}{S_{aD}IW} \tag{15}$$

The result from the preliminary evaluation is 31.86% of the actual value.

Conclusions

We established a method to estimate the seismic performance school buildings retrofitted with RC jacketing and our main findings are as follows:

1. Most estimates are conservative.

2. Preliminarily estimation before retrofitting is possible.

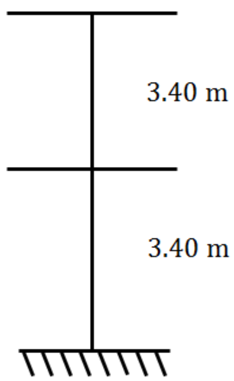

Fig.1 Column line of typical school building

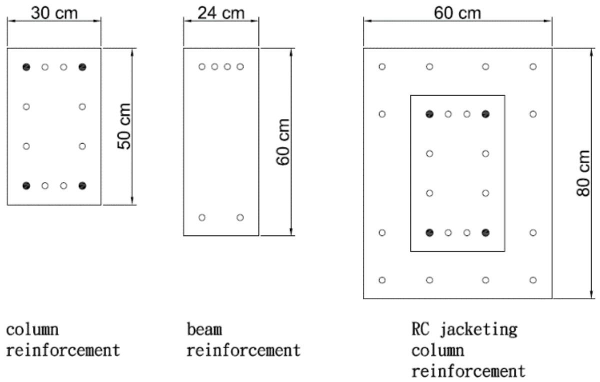

Fig.2 Size and reinforcement of column, beam and RC jacketing

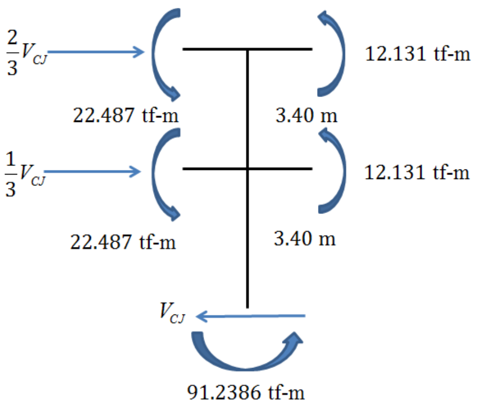

Fig.3 Free body diagram of retrofitted column line

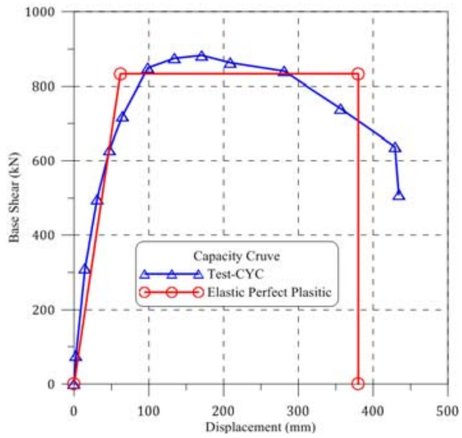

Fig.4 Capacity curve of Hou-Jia Junior High School building with RC jacketing

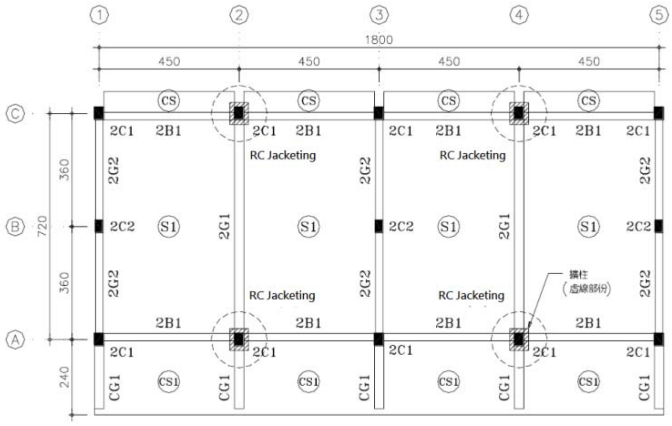

Fig.5 Plan view of second floor

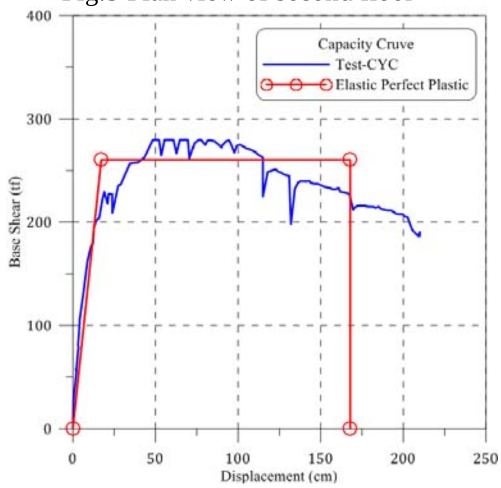

Fig.6 Capacity curve of Guan-Miao elementary school with RC jacketing

Reference

Ministry of the Interior, Building Seismic Design Code and Commentary, Taipei 2011.